Université de Liège

Faculté des Sciences Appliquées

Statistical analysis of pressure measurements on a high-rise building model in an atmospheric boundary layer in a wind tunnel

---

Romain Marcelle

Travail de fin d'études réalisé en vue de l'obtention du grade de Master Ingénieur Civil des Constructions

Année académique 2014-2015

Composition du jury: Vincent Denoël, Thomas Andrianne, Vincent E. Terrapon, Vincent de Ville de Goyet

Statistical analysis of pressure measurements on a high-rise building model in an atmospheric boundary layer in a wind tunnel

Romain Marcelle

$2^{ème}$ Master Ingénieur Civil des Constructions

Dans le domaine de l'ingénierie du vent, il est généralement admis que le vent peut être considéré comme un processus gaussien. Cependant, une étude récente réalisée à l'Université de Liège a montré que cette hypothèse n'est pas toujours vérifiée lors de la simulation d'une couche limite atmosphérique en soufflerie.

Les coefficients de pressions mesurés sur un modèle de structure sont influencés par la nature stochastique du vent incident. En cas de vent non gaussien, cela mène à des incohérences entre les mesures expérimentales et les hypothèses considérées par l'ingénieur en charge du dimensionnement de la structure. De plus, une évaluation précise des paramètres statistiques du champ de pression s'avère importante pour le dimensionnement des éléments de façade d'un bâtiment, plus particulièrement concernant leur resistance à la fatigue.

À première vue, on pourrait simplement conclure que les modèles ne peuvent être testés que dans la zone de la soufflerie où le vent est correctement modélisé comme un processus gaussien. Cependant, cela limiterais fortement la game de structures modélisables. La prédiction des paramètres statistiques du champ de pression ainsi que de la force résultante uniquement sur base des mesures de vitesses de vent n'est pas évidente. De plus, l'effet d'échelle influence la nature stochastique de la force résultante du vent sur une surface. Une étude plus approfondie du champ de pression sur un batiment couvrant la zone non gaussienne de la soufflerie est donc nécessaire.

Dans cette optique, le présent travail a pour but de montrer comment un vent de nature non gaussienne influence les mesures de pression sur un modèle de bâtiment de grande hauteur testé en soufflerie ansi que l'influence des dimensions de la surface considérée sur la distribution statistique de la force résultante du vent.

Statistical analysis of pressure measurements on a high-rise building model in an atmospheric boundary layer in a wind tunnel

Romain Marcelle

$2^{ème}$ Master Ingénieur Civil des Constructions

It is common practice in wind engineering to consider the wind flow as a Gaussian stochastic process. However, a recent study carried out at the university of Liège showed that this assumption is not verified in simulated atmospheric boundary layer.

In this context, the pressure coefficients recorded on a building model would be influenced by the stochastic nature of the wind flow. This leads to inconsistencies with designers assumptions. At the same time, an accurate description of the probabilistic nature of the pressure field is a major interest for the design of cladding on buildings; especially considering the fatigue damages.

At first glance, we could conclude that building models can only be tested in the region of the wind tunnel where the wind flow is Gaussian. Nonetheless, this would limits the range of models that can be tested. The prediction of the statistical parameters of the pressure field and the resultant wind force on the basis of those of the incident wind flow is not straightforward. Moreover, the size effect of the considered area also influences the statistical distribution of the wind load on a building facade. Therefore it appears necessary to analyze the pressure field around a model that covers the zone of non-Gaussian wind flow.

With this in mind, this thesis aims to show the influence of a non-Gaussian wind flow on the pressure measurements recorded on a high-rise building model in an atmospheric boundary layer in wind tunnel. At the same time, it will present the influence of the considered facade area on the stochastic nature of the resultant force on cladding.

Je tiens à remercier tout particulièrement Monsieur Vincent Denoël, professeur à l'Université de Liège et promoteur de ce travail, pour ses conseils avisés, son soutien et sa disponibilité.

Je tiens également à remercier Monsieur Thomas Andrianne, responsable de la soufflerie de l'Université de Liège, pour ses nombreux conseils et le grand intérêt qu'il a manifesté tout au long de cette étude.

Je remercie les membres de mon jury pour l'intérêt et l'attention portée à mon travail.

Merci à Monsieur Freddy Wertz pour son aide et sa collaboration.

Finalement, je remercie mes proches qui m'ont soutenu durant toute la durée de mes études.

Contents

Chapter 1

Introduction

In wind engineering, the basic methodology followed to design structures is first to characterize the wind flow, then compute the pressure field, and finally integrate the pressures to obtain resultant forces. The wind flow $V(x, y, z, t)$ can be represented by its mean component $U(x, y, z)$ constant in time, and its turbulent part $u(x, y, z, t)$ that vary in time and space. Using the quasi-static theory, the pressure field is computed by multiplying aerodynamic coefficients by the square of the wind velocity. It is common practice in wind engineering to consider the wind flow as a Gaussian stochastic process and to neglect the turbulence quadratic component. In this case, both the pressure field and the resultant forces are also Gaussian processes. However, numerous researches in wind tunnel and on real scale models, have shown that the pressure field cannot be considered as a Gaussian process in some locations of a building [1]. This approximation leads to consider peak factors that underestimate extreme pressure values. An accurate description of the probabilistic nature of the pressure field is a major interest for the design of cladding on buildings. Especially considering the fatigue damages.

A recent study on wind speed measurements in wind tunnel, carried out at the University of Liège by T. Andrianne and V. Denoël [Andrianne and Denoël, 2014], showed that the assumption of a wind flow characterized by a Gaussian probability density function is not verified in simulated atmospheric boundary layer. In this context, the pressure coefficients recorded on a building model in the wind tunnel would be influenced by the stochastic nature of the wind flow. These coefficients would then be used by designers that would make the assumption of a Gaussian wind flow and pressure field. This situation is obviously inconsistent.

The purpose of this master thesis is to answer two questions. The first one is: "How does a non-Gaussian wind flow influence the pressure measurements recorded in an atmospheric boundary layer in wind tunnel"? The second question is: "How does the considered facade area influences the stochastic nature of the resultant force on cladding"?

To achieve my goals and answer those two questions, I measured pressure coefficients on a high rise building model in the wind tunnel of the University of Liège. The pressure has

[1] An exhaustive list of these researches is proposed in [Gioffrè et al., 2001]

been collected along the height of the model and on three zones characterized by a high density mesh of measurement taps.

This thesis is structured in seven chapters. After this short introduction, I will define some terms and concepts that are important and widely used in the dissertation. Then, I will analyze the wind speed measurements collected by T. Andrianne and V. Denoël in order to characterize the atmospheric boundary layer created in the wind tunnel. This will set the basis of the comparison with the pressure measurements recorded during my experiment. The fourth chapter will present the experimental set-up and methodology used to record the pressure measurements. Chapter five will describe the experimental pressure results collected on the model. In chapter six, I will compare the wind velocity and the pressure measurements in order to answer the first question asked in this thesis. I will also analyze the influence of the cladding area on the stochastic nature of the resultant force and consequently answer the second question. Finally, the conclusions and perspectives that can be followed to extend the topic of this thesis will be proposed in chapter seven.

Chapter 2

Background information

2.1 Natural wind

The natural wind is created by the atmospheric motion around the earth. This movement is complex and consists of different motion patterns that take place at various space and time scales. It ranges from turbulence (vortices of few meters with a lifetime of some minutes) to local weather system and large planetary waves, which circumvent the entire globe and have a lifetime of several days [Dyrbye and Hansen, 1996]. Figure 2.1 represents the different motion patterns and their respective scales.

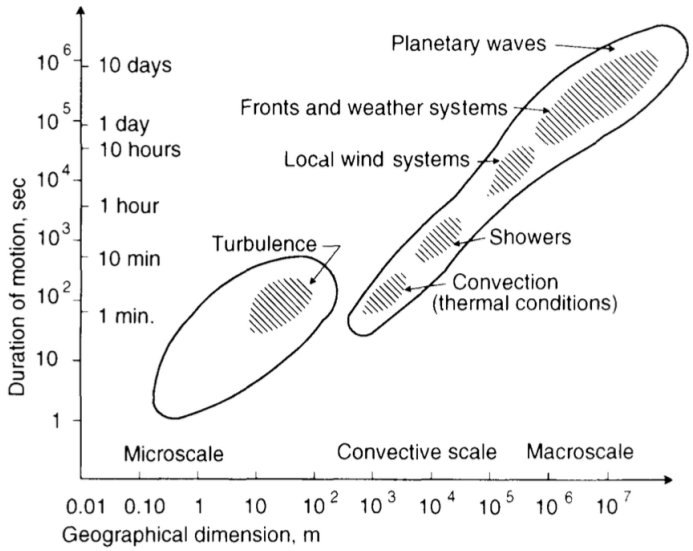

Figure 2.1 – Order of magnitude of time and space scales of different atmospheric motions, source: [Dyrbye and Hansen, 1996]

The separation between microscale and macroscle phenomena can be represented in the frequency domain. Van der Hoven computed the autospectrum of wind measurements collected at 100 m height in Brookheaven, NY, USA. A representation of this spectrum is showed on figure 2.2.

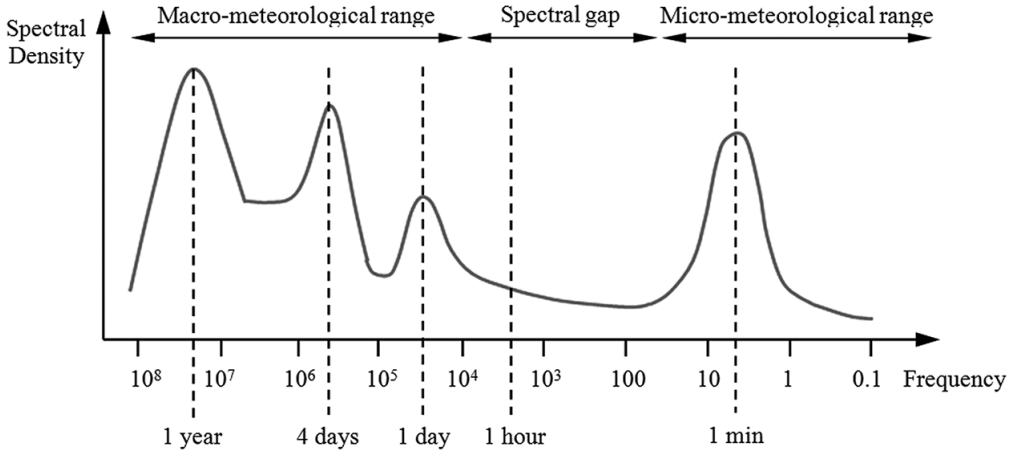

Figure 2.2 – Van der Hoven spectrum, source: [Wang et al., 2013]

The spectral gap between approximately 60 and 10 minutes indicates that the large scale climate is independent from the turbulence in the atmospheric boundary layer and both phenomena can be superimposed. For this reason, the characteristic duration chosen to study the wind effect on structures is equal to 10 minutes in Eurocode 1-4 [EN1991-1-4, 2005]. This also explains why the wind flow $V(x, y, z, t)$ can be decomposed in a mean climatic component $U(x, y, z)$ constant in time compared to the characteristic duration, and a turbulent part $u(x, y, z, t)$ that vary in time and space.

2.2 Atmospheric boundary layer

The atmospheric boundary layer is the first 200-300 m of the atmosphere where the wind flow is influenced by the topography and everything that stands on the ground. This is the region of interest for the design of building and other structures. As stated in the previous section, the wind can be decomposed in a mean and a turbulent components. The friction between the wind flow and the ground induces a mean wind velocity profile that increases with the altitude and a turbulent part that varies randomly around the mean value.

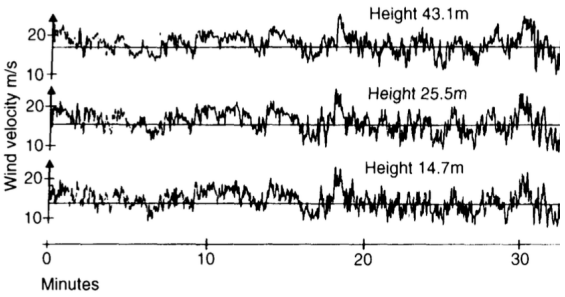

Figure 2.3 – Example of wind velocity measurements, source: [Dyrbye and Hansen, 1996]

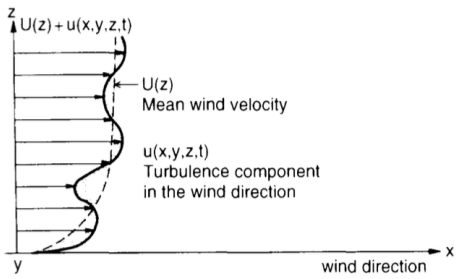

Figure 2.4 – Representation of the wind profile, source: [Dyrbye and Hansen, 1996]

As represented on figure 2.4, the mean velocity varies heavily in the first few meters and then tends toward a constant free flow velocity. The magnitude of the turbulent part is larger close to the ground and decreases with the altitude, as the wind becomes less and less disturbed by the ground.

From now on, I will consider a wind flow that is unidirectional and homogeneous in a horizontal plane. This means that the mean velocity only depends on the attitude and the turbulent component only depends on the altitude and the time.

Multiple models are available to describe the mean velocity profile. The Eurocode 1-4 proposes the following equations:

$$\begin{cases} U(z) = v_b k_r ln\left(\dfrac{z}{z_0}\right) \ for \ z_{min} < z < 200m \\ U(z) = U(z_{min}) \ for \ z < z_{min} \end{cases} \tag{2.1}$$

$$k_r = 0.19 \left(\frac{z_0}{z_{0,II}}\right)^{0.07} \tag{2.2}$$

v_b is the basic wind velocity and depends on the project location. This model considers different terrain characteristics as shown in figure 2.1. k_r is the terrain factor depending on the roughness length z_0.

Category	Description	z_0 (m)	z_{min} (m)	α
0	Sea or coastal area exposed to the open sea	0.003	1	-
I	Lakes or flat and horizontal area with negligible vegetation and no obstacles	0.01	1	0.12
II	Area with low vegetation and isolated obstacles	0.05	2	0.16
III	Area with regular cover of vegetation or buildings or with isolated obstacles	0.3	5	0.22
IV	Urban area covered with buildings of average height higher than 15 m	1	10	0.30

Table 2.1 – Terrain categories with their parameters adapted from [EN1991-1-4, 2005]

Another widely used model is the power law profile defined as:

$$U(z) = U(z_{ref}) \left(\frac{z}{z_{ref}} \right)^{\alpha} \tag{2.3}$$

Considering z_{ref} the reference height. Note that no power law profile is defined for the terrain category 0.

The turbulence component of the wind flow varies in time and space and is characterized by four parameters:

- **The standard deviation**:

$$\sigma_u(z) = \sqrt{E[u(z,t) - U(z)]^2} \tag{2.4}$$

The Eurocode 1-4 gives the following estimation of the standard deviation of the turbulence:

$$\sigma_u = k_r v_b \tag{2.5}$$

- **The intensity of turbulence**:

$$I_u(z) = \frac{\sigma_u}{U(z)} \tag{2.6}$$

- **The integral scale**:

  The longitudinal integral scale of turbulence L_u^x represents a measure of the nominal size of vortices present in the wind flow. It is often computed using Taylor's hypothesis of "frozen turbulence". According to [Dyrbye and Hansen, 1996] this approximation is normally considered to be accurate in natural wind. Using this assumption, temporal variation are obtained by a translation of "frozen turbulence" with the mean wind velocity. The longitudinal integral scale of turbulence is equal to:

$$L_u^x(z) = U(z)T(z) \tag{2.7}$$

  With $U(z)$ the longitudinal mean wind speed and $T(z)$ is the time scale defined as :

$$T(z) = \int_0^\infty \rho_u^T(z,\tau)d\tau \tag{2.8}$$

  If a measurement is taken at time t, it will give a lot of information about the measurement taken at time $t+\tau$ if $\tau \ll T(z)$, but only a little information if $\tau \gg T(z)$.

  The autocorrelation function $\rho_u^T(z,\tau)$ of the turbulence is defined as the mathematical expectation of the product of the turbulent wind speed taken at time t and $t + d\tau$:

$$\rho_u^T(z,\tau) = \frac{E[u(z,t).u(z,t+d\tau)]}{\sigma_u^2(z)} \tag{2.9}$$

  It represent how a measurement at time t will give information about a measurement at time $t + d\tau$.

The Eurocode 1-4 gives the following estimation of the integral scale of turbulence:

$$L_u^x(z) = \begin{cases} L_t \left(\frac{z}{z_t}\right) \ pour \ z_{min} < z < 200m \\ L_u^x(z_{min}) \ pour \ z < z_{min} \end{cases} \tag{2.10}$$

$L_t = 300m$, $z_t = 200m$, $a = 0.67 + 0.05ln(z_0)$

- **Power spectral density function**:

  This function describes the frequency distribution of the turbulence and is defined as the Fourier transform of the autocorrelation function:

$$S_u(n, z) = \frac{1}{2\pi} \int_{-\infty}^{+\infty} \rho_u(z, \tau) e^{-j\omega\tau} d\tau \tag{2.11}$$

  Different models have been proposed by scientists to estimate this function. The most famous ones are the expressions developed by Von-Karman and by Kaimal (used in the Eurocode 1-4).

$$Von\ Karman : S_u(n, z) = \frac{4\frac{L_u^x}{U(z)}}{[1 + 70.7(\frac{nL_u^x}{U(z)})^2]^{5/6}} \sigma_u^2 \tag{2.12}$$

$$Kaimal(Eurocode\ 1) : S_u(n, z) = \frac{6.8\frac{L_u^x}{U(z)}}{[1 + 10.2(\frac{nL_u^x}{U(z)})]^{5/3}} \sigma_u^2 \tag{2.13}$$

2.3 Wind effect on structures

Now that we have characterized the wind in a atmospheric boundary layer, the next step is to compute the pressure and the resultant forces induced by the wind on structures.

the local wind pressure can be obtained with:

$$P = \frac{1}{2}\rho C_d \tilde{V}^2 \tag{2.14}$$

$\tilde{V}^2 = U + u - \dot{x}$ is the relative wind velocity with respect to the structure. $\dot{x}$ is the structure velocity. C_d is a coefficient that depends on the structure's aerodynamics properties. ρ is the density of the air.

If we consider the quadratic terms in u and $\dot{x}$ negligible, equation 2.14 can be written:

$$P = \frac{1}{2}\rho C_d (U^2 + 2Uu - 2U\dot{x}) \tag{2.15}$$

This expression highlights the three effects of the wind: the mean, the turbulent, and the dynamic effects.

The Eurocode 1-4 uses the concept of "equivalent static load" and consider the turbulent and dynamic effects of equation 2.15 through the computation of a peak velocity pressure $q_p(z)$ and a dynamic coefficient c_d.

$$q_p(z) = [1 + 2k_p I_v(z)]\frac{1}{2}\rho U^2(z) \tag{2.16}$$

k_p is the peak factor considered equal to 3.5 by the Eurocode. Additional information about this expression can be found in appendix A.

Resultant forces are then computed with:

$$F_w = c_s c_d \sum C q_p(z_e) A_{ref} \tag{2.17}$$

$c_s c_d$ is composed of the size factor c_s that takes into account the reduction effect on the wind action due to the non-simultaneity of occurrence of the peak wind pressures on the surface. This factor is presented in appendix B. It also contains the dynamic factor c_d that accounts for the resonance effect of the structure introduced by the vibrations due to the turbulence. A_{ref} is the reference surface exposed to the wind action. C can be an external pressure, internal pressure or force coefficient depending on the method chosen in Eurocode 1-4.

2.4 Stochastic process

This section is based on the stochastic process theory developed in [Denoël, 2013].

A stochastic or random process can be defined as an organized set of random variables i.e. a function of random variables. A random variable is completely characterized by its probability density function $p_X(x)$, with $p_X(x)dx$ the probability that the variable X takes a value in the interval $[x; x + dx]$. This concept can be extended for stochastic process with the first order probability density function $p_x(x, t)$, considering $p_x(x, t)dx$ the probability that $x(t)$, value of the function at time t, take a value in the interval $[x; x+dx]$.

Unlike for random variable, this function does not fully characterize a random process. Thus, we need to define higher order functions. the second order probability density function is defined by $p_x(x_1, t_1; x_2, t_2)$, considering $p_x(x_1, t_1; x_2, t_2)dx_1dx_2$ the probability that $X_1 = x(t_1)$ takes a value in the interval $[x_1; x_1 + dx_1]$ and $X_2 = x(t_2)$ takes a value in the interval $[x_2; x_2 + dx_2]$. The characterization of a stochastic process with a second order probability density function (PDF) is more complete, and provides information about the correlation between values at different time steps.

However, a random process is only fully characterized by knowing their probability density functions of order 1 to n, defined as $p_x(x_1, t_1; ...; x_n, t_n)$ with $n \to \infty$. Despite being exhaustive this representation of a stochastic process is impossible to achieve from an experimental point of view.

Another, more practical, representation of random process is based on the concept of mathematical expectation. The mathematical expectation of order 1, 2 and n are respectively defined as:

$$E[f(x_1)] = \int_{\mathbb{R}^n} f(x_1)p_x(x, t)dx \tag{2.18}$$

$$E[f(x_1, x_2)] = \iint_{\mathbb{R}^n} f(x_1, x_2)p_x(x_1, t_1; x_2, t_2)dx_1dx_2 \tag{2.19}$$

$$E[f(x_1, ..., x_n)] = \int_{\mathbb{R}^n} ... \int f(x_1, ..., x_n)p_x(x_1, t_1; ...; x_n, t_n)dx_1...dx_n \tag{2.20}$$

Let's focus only on the mathematical expectation of order 1. If we replace $f(x_1)$ by x_1^k in equation 2.18, we can determine the k^{th} statistical moment of a random process.

$$m_{k,x}(t) = E[x_1^k] = \int_{-\infty}^{+\infty} x_1^k p_x(x_1, t) dx_1 \qquad k \in \mathbb{N}, \tag{2.21}$$

The first statistical moment is called mean and is defined as:

$$\mu_x(t) = E[x_1] = \int_{-\infty}^{+\infty} x_1 p_x(x_1, t) dx_1 \tag{2.22}$$

Now, if we replace $f(x_1)$ by $(x_1 - \mu_x)^k$ in equation 2.18, we can determine the k^{th} centered statistical moment of a random process.

$$\tilde{m}_{k,x}(t) = E[(x_1 - \mu_x)^k] = \int_{-\infty}^{+\infty} (x_1 - \mu_x)^k p_x(x_1, t) dx_1 \qquad k \geq 2 \in \mathbb{N} \tag{2.23}$$

Once again, by choosing specific values of k, we can define parameters that describe statistical properties of a random process with respect to its mean. If $k = 2$ we find the variance of the process, that is also the square of the standard deviation σ. This parameter represents how far the data are scattered around the mean value.

$$\sigma_x^2(t) = \tilde{m}_{2,x}(t) = E[(x_1 - \mu_x)^2] = \int_{-\infty}^{+\infty} (x_1 - \mu_x)^2 p_x(x_1, t) dx_1 \tag{2.24}$$

If $k = 3$ we come up with the third centered statistical moment. This expression can be normalized with the second moment to give the skewness γ_3 of the process. This parameter is very important to characterize the non-gaussianity of a random process. It represents a measure of the symmetry of the distribution around its mean value.

$$\tilde{m}_{3,x}(t) = E[(x_1 - \mu_x)^3] = \int_{-\infty}^{+\infty} (x_1 - \mu_x)^3 p_x(x_1, t) dx_1 \tag{2.25}$$

$$\gamma_3 = \frac{\tilde{m}_{3,x}(t)}{\tilde{m}_{2,x}(t)^{\frac{3}{2}}} \tag{2.26}$$

In the same way, the fourth centered statistical moment can also be normalized to give the kurtosis γ_4 that characterizes the peakedness (peak width) of the distribution.

$$\tilde{m}_{4,x}(t) = E[(x_1 - \mu_x)^4] = \int_{-\infty}^{+\infty} (x_1 - \mu_x)^4 p_x(x_1, t) dx_1 \tag{2.27}$$

$$\gamma_4 = \frac{\tilde{m}_{4,x}(t)}{\tilde{m}_{2,x}(t)^2} \tag{2.28}$$

Figure 2.5 and 2.6 show the influence of positive and negative skewness and kurtosis on a probability density function. A Gaussian distribution presents a skewness of 0 and a kurtosis of 3. These two parameters are used in this thesis to asses the non-gaussianity of a process. According to [Kumar and Stathopoulos, 1998] a process can be considered non-Gaussian when its skewness and kurtosis are respectively higher than 0.5 and 3.5 in absolute value. These values are indicative and should not be taken as fixed limits.

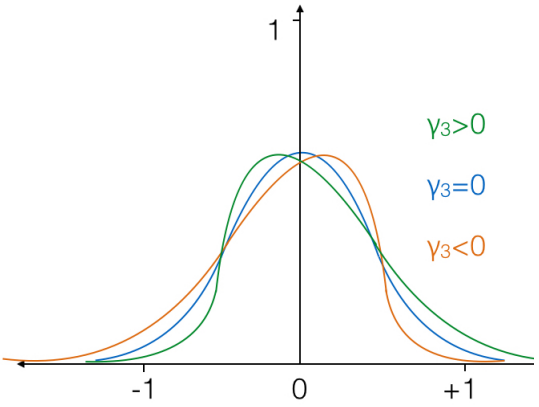

Figure 2.5 – Positive and negative skewness

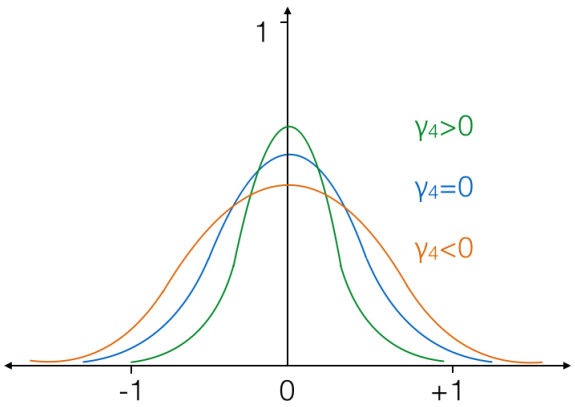

Figure 2.6 – Positive and negative kurtosis

These parameters characterize the distribution of a random process with respect to its mean value. Sometimes, more information are required and we need to consider the mathematical expectation of order 2. Like it has been done for the first order, replacing $f(x_1, x_2)$ by $(x_1 - \mu_x(t1))(x_2 - \mu_x(t_2))$ in equation 2.19, defines the autocovariance function.

$$Cov(x_1, x_2) = E[(x_1 - \mu_x)(x_2 - \mu_x)] = \iint_{\mathbb{R}^n} (x_1 - \mu_x)(x_2 - \mu_x) p_x(x_1, t_1; x_2, t_2) dx_1 dx_2 \tag{2.29}$$

This function represents the degree of correlation that exists between two random variables. Another useful expression is the correlation function, that expresses the same thing but takes its values between -1 and 1. This function has already been introduced in section2.2 and is defined as:

$$\rho(x_1, x_2) = \frac{Cov(x_1, x_2)}{\sigma_{x_1}\sigma_{x_2}} = \frac{E[(x_1 - \mu_x)(x_2 - \mu_x)]}{\sigma_{x_1}\sigma_{x_2}} \tag{2.30}$$

In this definition, x_1 and x_2 represent the values of a single stochastic process at time t_1 and t_2. We can also compute the correlation between two different random processes by replacing x_1 and x_2 by two values of these two stochastic processes at the same instant. In this case, the prefix "auto" is replaced by "cross" to mark the difference.

The same information can also be retrieved in the frequency domain with the coherence function between two stochastic processes:

$$\Gamma_{xy} = \frac{S_{xy}(\omega)}{\sqrt{S_x(\omega)S_y(\omega)}} \tag{2.31}$$

S_{xy} is the cross-spectrum function of the two stochastic processes and can be computed with:

$$S_{xy} = FFT(x).conj[FFT(y)] \tag{2.32}$$

Where $conj[FFT(y)]$ denotes the conjugate of Fourier transform of the process y. This function is faster and easier to compute than its counterpart in the time domain.

The integral in the preceding definitions are realized over a range of samples. From an experimental point of view, it is impossible to record a sufficient number of realizations to be able to compute accurately the statistical moments. The theorem of ergodicity states that, for stationary random process, the integration can be realized over time instead that over a set of samples. The definition of the mathematical expectation can be rewritten:

$$E[f(x_1)] = \int_{\mathbb{R}^n} f(x_1)p_x(x,t)dx = \lim_{T\to\infty} \frac{1}{T}\int_0^T f(x_i(t))dt \tag{2.33}$$

And the definitions of the non centered and centered statistical moments of order k become:

$$m_{k,x}(t) = E[x_1^k] = \lim_{T\to\infty} \frac{1}{T} \int_0^T x_i(t)^k dt, \tag{2.34}$$

$$\tilde{m}_{k,x}(t) = E[(x_1 - \mu_x)^k] = \lim_{T\to\infty} \frac{1}{T} \int_0^T (x_i - \mu_x)^k dt \qquad k \geq 2 \in \mathbb{N} \tag{2.35}$$

A necessary condition for a random process to be stationary is that its probability density function of order 1 does not vary in time.

$$Stationary\ process \rightarrow \frac{\partial p_x(x,t)}{\partial t} = 0 \tag{2.36}$$

The link between the previous section and the notions developed in this one can be the concept of peak factor and extreme or characteristic wind load.

The characteristic wind load F_{max} represents the largest force that a structure is likely to undergo during a storm period of say 10 minutes. It is defined as:

$$F_{max} = \bar{F} + g_F \sigma_F \tag{2.37}$$

With $\bar{P}$ a 10 minutes mean pressure, g_F the peak factor and σ_F a 10 minutes pressure standard deviation.

This is what is basically computed by following the procedure described in Eurocode 1-4. The peak factor relates the extreme values of a process to its mean value. Therefore, it seems obvious that it is influenced by the statistical distribution of the stochastic process. Making the assumption of a Gaussian peak factor when the distribution is actually heavily skewed can leads to nonconservative characteristic loads.

Chapter 3

Analysis of velocity measurements

This chapter is dedicated to the characterization of the atmospheric boundary layer created in the wind tunnel of the University of Liège. I will first present the experimental set-up used by [Andrianne and Denoël, 2014] and then analyze the collected data in order to determine the wind flow characteristics and statistical parameters. This will set the basis of the comparison with the pressure measurements that will be presented in section 6.1.

3.1 Velocity measurements experimental set-up

According to [Andrianne and Denoël, 2014], the measurements were collected in the wind tunnel of the University of Liège in the wind engineering configuration (Goettingen type). The section dimensions are : length = 13.5 m, width = 2.5 m, height = 1.8 m.

Figure 3.1 – Wind tunnel of the University of Liège, source:
$http://www.facsa.ulg.ac.be/cms/c_285333/fr/equipements-remarquables$

The atmospheric boundary layer (called here ABL1) was created using 5 spires (1.15 m high), a castellated fence (0.15 m high) and wooden blocks (0.05 m x 0.05 m x 0.1 m), covering the floor of the wind tunnel up to 1 m upstream the measurement location. The wind speed measurements were taken using two single component Hot-Wire Probes (HWP's). The HWP's, separated by 0.3 m in the transversal direction to the wind (y-axis), were translated vertically at the center of the test section. The measurement method parameters are summarized in table 3.1.

Hot-Wire type	1D (Dantec Dynamic)
Acquisition frequency	1kHz
Measurement duration (per position)	4 min
18 vertical positions	0.04m - 1.4m

Table 3.1 – Measurement parameters adapted from [Andrianne and Denoël, 2014]

3.2 Mean velocity and turbulence intensity profiles

Figure 3.2 and 3.3 represent the mean wind velocity and turbulence intensity profiles. The dots represent the actual measurements

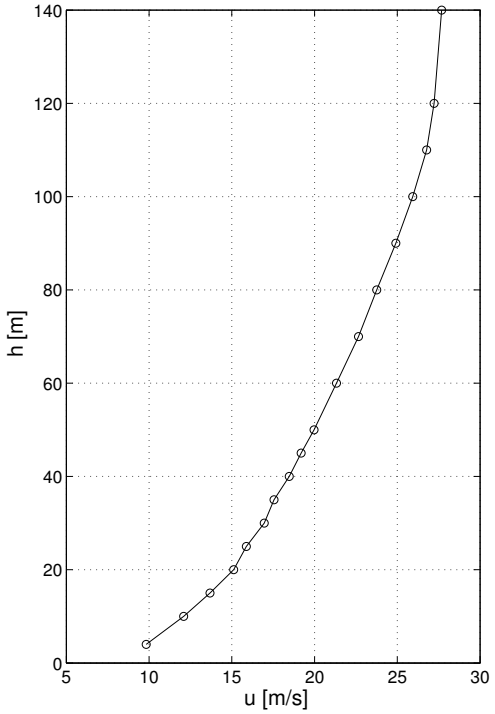

Figure 3.2 – Mean wind speed profile (ABL1)

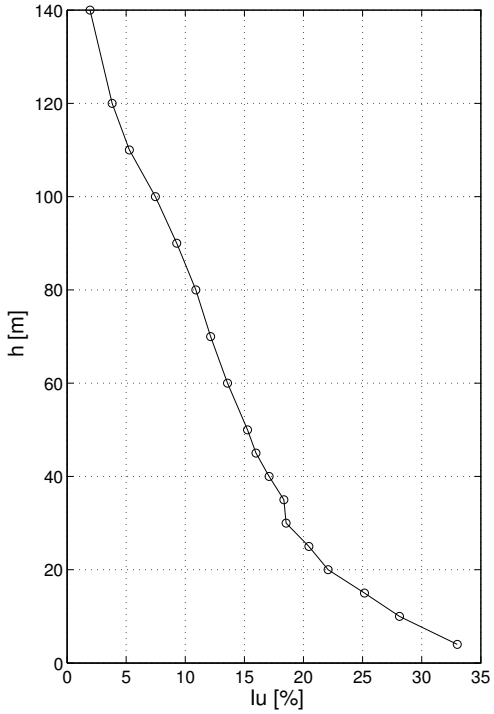

Figure 3.3 – Turbulence intensity profile (ABL1)

Figure 3.4 presents the standard deviation of the velocity measurements. We can see that the fluctuations decrease slowly in the first 80 m of the boundary layer and then decline faster. The shape of the turbulence intensity profile can also be explained by looking at figure 3.2 and 3.4.

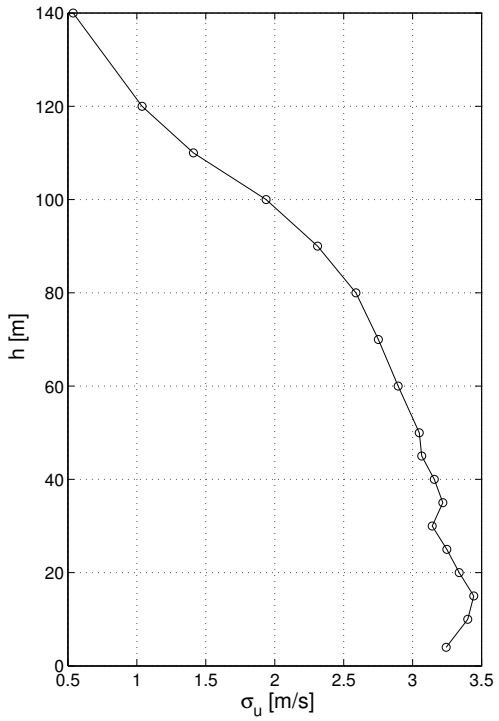

Figure 3.4 – Standard deviation profile (ABL1)

At this point, it is interesting to compare the atmospheric boundary layer created in the wind tunnel with the theoretical profiles defined in the Eurocode 1.4 (see section 2.2).

To run this comparison, scale factors need to be defined. the values are presented in table 4.1.

Scale factor	Definition	Value
Length scale	$\epsilon_l = L_{model}/L_{prototype}$	1/100
Velocity scale	$\epsilon_u = U_{model}/U_{prototype}$	1/1.71
Frequency scale	$\epsilon_f = f_{model}/f_{prototype}$	58
Time scale	$\epsilon_t = t_{model}/t_{prototype}$	1/58

Table 3.2 – Scale factors for the velocity measurements

The reference height is chosen equal to 100 m at full scale (height of building prototype, see section 4.1). The wind speed scale factor is defined as the ratio between the speed recorded in the wind tunnel at the reference height and the speed of a fourth category

wind profile of the Eurocodes at the same height ($v_b = 24$m/s). The frequency and time scale factor have been computed by conservation of the strouhal number $St = fD/U$, with f the frequency, D the characteristic length and U the velocity. With these factors, a record of 10 seconds corresponds to approximately 10 minutes in full scale.

Figure 3.5 show that the experimental mean velocity profile is close to a fourth terrain category of the Eurocode 1-4. The turbulence intensity is harder to fit to a terrain category as depicted on figure 3.6.

We can also compare the experimental mean velocity profile with the power law model. As it can be seen on figure 3.7, this model confirms the fourth terrain category.

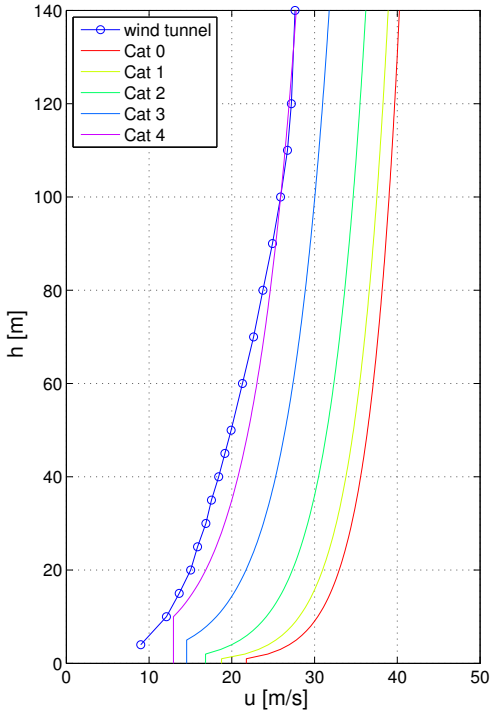

Figure 3.5 – Mean wind velocity profile comparison with Eurocode 1-4 (ABL1)

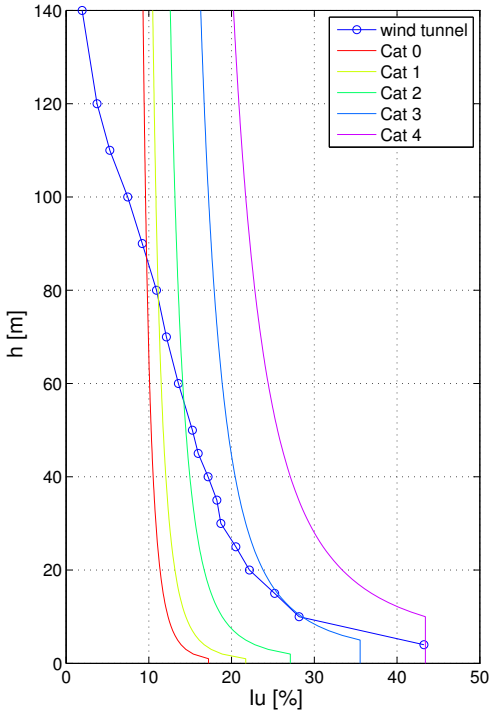

Figure 3.6 – Turbulence intensity profile comparison with Eurocode 1-4 (ABL1)

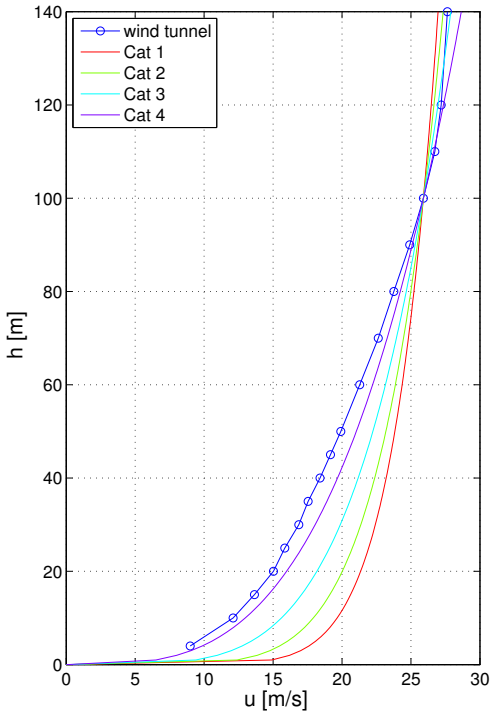

Figure 3.7 – Mean wind speed profile comparison with the power law (ABL1)

3.3 Turbulence integral scale

Recalling the theory presented in section 2.2, The integral scale of turbulence is defined by the integral of the autocorrelation function multiplied by the mean wind velocity. A discussion on how this integration have been realized can be found in appendix C.

Figure 3.8 suggests that the nominal size of vortices present in the wind flow is around 40 m (0.4 m at the model scale). If we compute the integral length of turbulence with equation 2.10 from the Eurocode 1-4 we obtain 188 m. According to [ASCE, 1999] this situation corresponds to a "partial simulation of wind turbulence" where, despite large vortices, the small scale turbulence is correctly represented. Considering this atmospheric boundary layer configuration, if the large scale turbulence needs to be modeled accurately, the length scale should be chosen in the range: [1/400 - 1/500]. Indeed, it is impossible to create vortices of 188 m inside the wind tunnel with a scale of 1/100. This would result in vortices larger than the size of the tunnel itself.

Figure 3.9 shows that the time scale of the turbulence stays around 2 seconds.

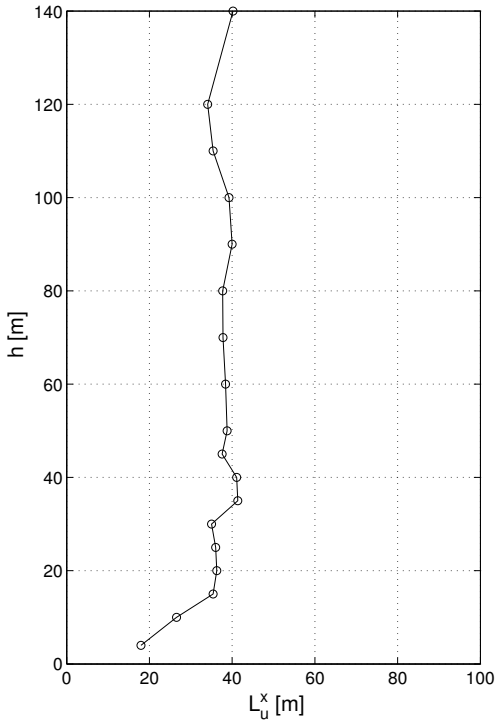

Figure 3.8 – Integral scale of turbulence profile (ABL1)

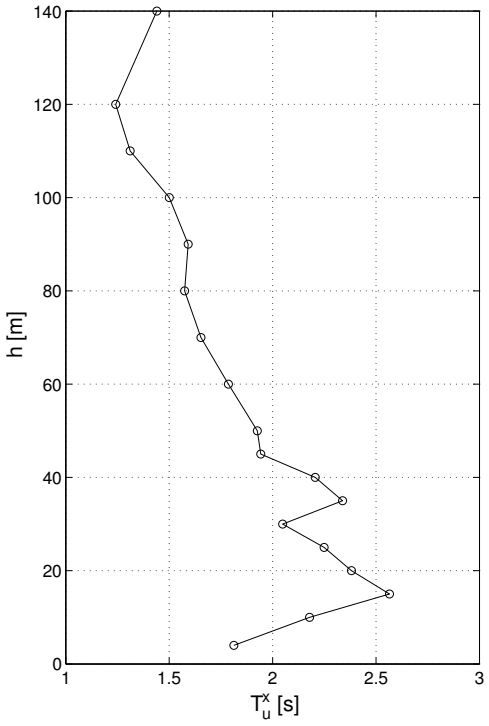

Figure 3.9 – Time scale of turbulence profile (ABL1)

3.4 Power spectral density function

According to [Dyrbye and Hansen, 1996] turbulent energy is generated in large eddies (low frequencies) and dissipated in small vortices (high frequencies). In the intermediate region, called the internal subrange, the energy production is balanced by the energy dissipation and the turbulent energy spectrum is independent of the specific mechanisms of generation and dissipation. Assuming Taylor hypothesis of "frozen turbulence", and considering frequencies in the internal subrange, the non dimensional power spectrum $R_N(h,n)$ is given by:

$$R_N(h,n) = Af_l^{-2/3} \tag{3.1}$$

A is a constant that depends slightly on the height and f_l is the non dimensional frequency: $f_l = nL_u^x(h)/U(h)$. The Von Karman and Kaimal theoretical expressions (see equation 2.12 and 2.13), consider respectively a constant A equal to 0.14 and 0.115.

Figure 3.10 represents the normalized power spectral density function of the longitudinal turbulence compared to Von Karman and Kaimal (EC1) theoretical functions. We can see on this figure that the slope, represented by the exponent $-2/3$ in equation 3.1, is not exactly represented by the experimental data. In the internal subrange, these measurements are better estimated by the black line defined as:

$$R_N(h,n) = 0.10f_l^{-0.8} \tag{3.2}$$

This indicates that the energy is distributed differently compared what is predicted by the theoretical expressions.

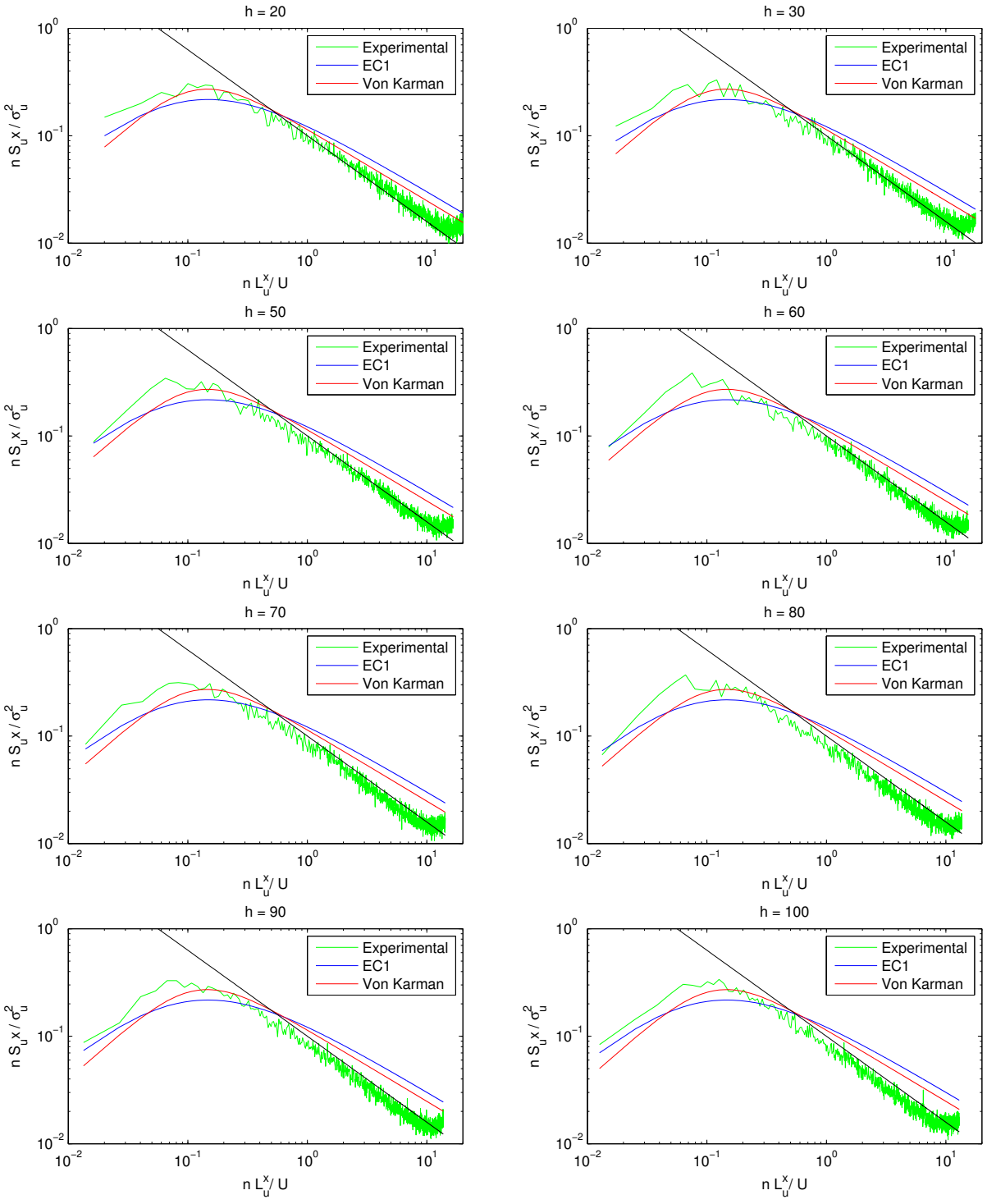

Figure 3.10 – Power spectral density function of the longitudinal turbulence (ABL1)

3.5 Statistical analysis

As it has been said previously, the wind flow is supposed to be Gaussian by codes and general practice. To be consistent with this assumption, the objective is therefore to simulate, in the wind tunnel, an atmospheric boundary layer in which the wind flow is a gaussian process.

A practical way to asses the gaussianity of a stochastic process is to compute its skewness and its kurtosis (defined by equation 2.26 and 2.28). Figure 3.11 shows that the skewness of the wind flow stays close to 0 in the first 50 m and then decreases progressively. From 0 to 80 m, the kurtosis presented on figure 3.12 oscillates around 3 and then deviates in higher values.

If we consider the indicative lower bounds of 0.5 and 3.5 in absolute values to assume that a process is non-Gaussian, we can conclude that above 70 m the wind flow cannot be considered as a Gaussian process any more.

Both the skewness and the kurtosis tend to come back to 0 and 3 respectively at the height of 140 m (1.4 m at model scale), but data recorded at that height are influenced by the roof of the wind tunnel and cannot be taken into consideration for the conclusions. We can also notice that under 20 m, the skewness changes its sign. This height corresponds to the end of the roughness sub-layer created by the wooden blocks.

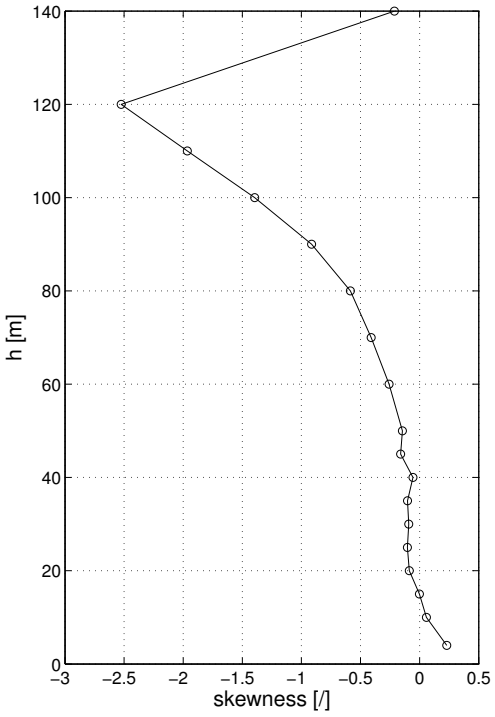

Figure 3.11 – Skewness of the wind speed data (ABL1)

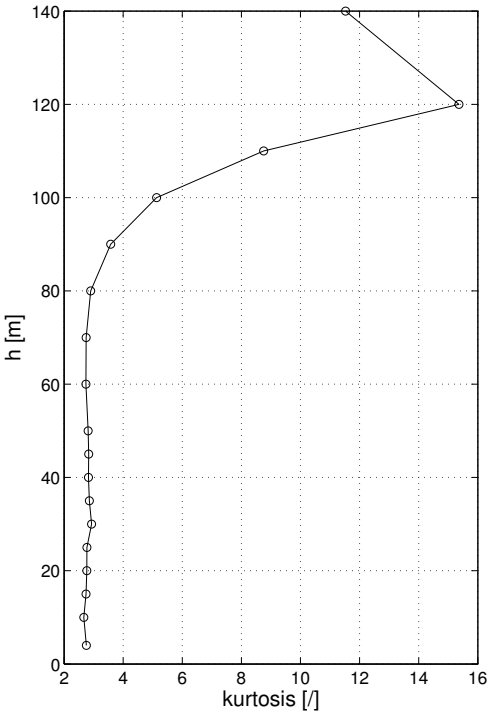

Figure 3.12 – Kurtosis of the wind speed data (ABL1)

Figure 3.13 shows the probability density functions of the wind speed data and a Gaussian PDF having the same mean and standard deviation. These graphs confirm that the wind flow follows a Gaussian distribution between the heights of 0 and 50 m, while above 70 m they clearly appear non-Gaussian.

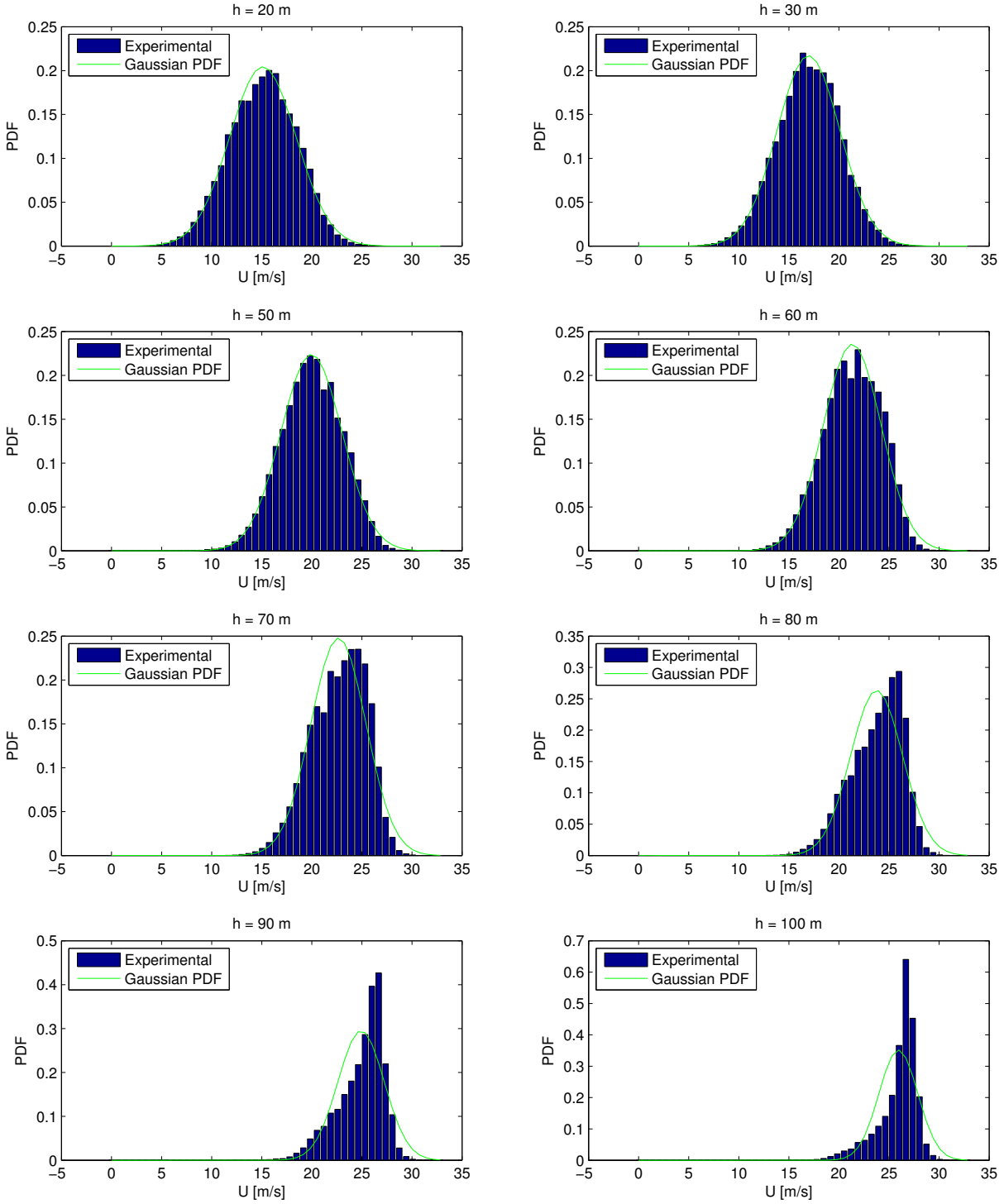

Figure 3.13 – Probability density function of the wind speed data and Gaussian PDF (ABL1)

3.6 Personal atmospheric boundary layer measurements

The pressure measurements that will be presented in this thesis where recorded in two different atmospheric boundary layers:

- ABL2: created by 5 spires (1.15 m high), a castellated fence (0.15 m high) and wooden blocks (0.05 m x 0.05 m x 0.1 m), covering the floor of the wind tunnel up to 3.5 m upstream the model location.
- ABL3: created by 5 spires (1.15 m high), a castellated fence (0.15 m high) and wooden blocks (0.05 m x 0.05 m x 0.1 m), covering the floor of the wind tunnel up to 0.3 m upstream the model location.

Figure 3.14 and 3.15 present respectively the ABL2 and the ABL3. The blueish part contains the added wooden blocks compared to the ABL2.

Figure 3.14 – Picture of the experimental set-up used to create the atmospheric boundary layer ABL2

Figure 3.15 – Picture of the experimental set-up used to create the atmospheric boundary layer ABL3

I measured the mean wind speed profile in both new configurations using an ultrasonic anemometer 2D Thies Clima. Note that this device was not able to record the variance of the wind flow accurately. Thus the intensity of turbulence cannot be presented here. Figure 3.16 shows the mean wind speed profiles of ABL1, ABL2 and ABL3. This figure suggests that the three ABL's are very similar. In fact, the addition of wooden blocks closer to the model only changes the profile in the first 20 m.

Figure 3.17 compares the new atmospheric boundary layers with the profiles defined in the Eurocode 1.4.

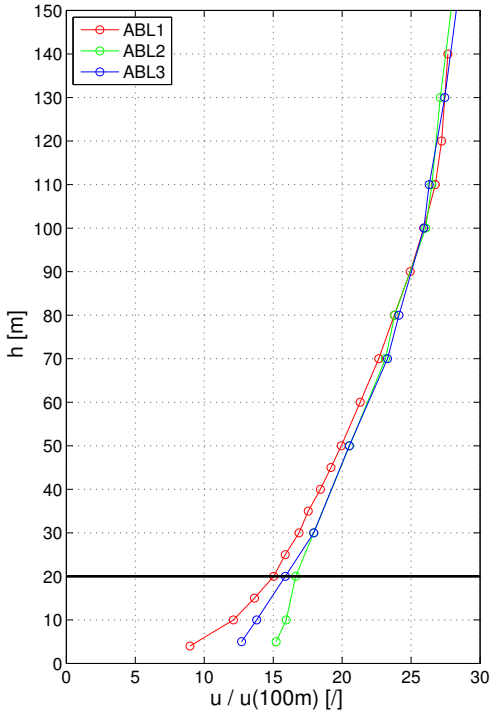

Figure 3.16 – Mean wind speed profiles of ABL1, ABL2 and ABL3

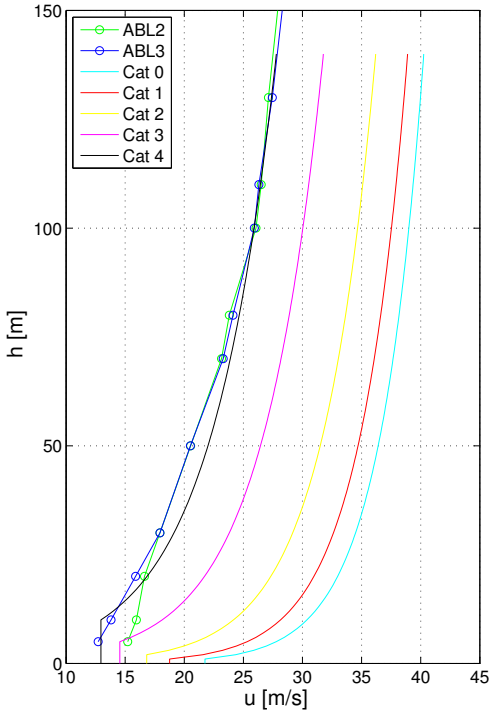

Figure 3.17 – Mean wind speed profiles of ABL2 and ABL3 compared to the velocity profiles of the Eurocode 1-4

3.7 Conclusion

This section has characterized the atmospheric boundary layer that is created in the wind tunnel of the University of Liège. We have seen that the velocity profile is similar to the fourth terrain category of the Eurocode 1-4. We have also noticed that the turbulence intensity is quite different compared to the theoretical profiles. Then, the longitudinal integral scale was found to be around 40 m, which hardly represents the large scale turbulence with a length scale of 1/100. However, the most interesting result of this section is the statistical characterization of the wind flow. This section has demonstrated that the wind flow can be considered Gaussian in the first 50 cm of the wind tunnel. Between 50 and 70 cm the transition to non-Gaussian flow occurs and above 70 cm the wind is clearly non-Gaussian.

Chapter 4

Pressure measurements experimental set-up

4.1 Experimental model

The pressure measurements were collected in the wind tunnel of the University of Liège in the wind engineering configuration as presented in section 3.6.

I considered two types of measurement layouts aiming to two specific goals:

1. **The vertical layout** consists of 98 measurement taps aligned along a vertical line at the center of a facade of the model (see figure 4.1). The purpose of this configuration is to describe the pressure distribution along the height of the model. This will also enable the comparison between the pressure and the velocity signals discussed in section 3.

2. **The patches layout** is composed of three patches of 50 measurement taps each. A patch consists of 10 lines of 5 taps (see Figure 4.2). Between lines, the measurement taps are spaced by 0.5 cm whereas between rows, they are spaced by 2 cm. Each line starts and finishes at 1 cm from the edges of the model. The three patches are located on the opposite facade that contains the vertical layout. The purpose of this configuration is to gather pressure information on a refined mesh. The positions of the three patches are chosen in the following way:

    - The first patch is positioned between the height of 28 and 32.5 cm from the bottom of the model. This position has been chosen because at that height the wind flow presents a Gaussian distribution and is no more influenced by the floor of the wind tunnel.
    - The second patch is placed between the height of 59 and 63.5 cm from the bottom of the model. This position corresponds to the transition zone between Gaussian and non-Gaussian wind flows.
    - The third patch is placed between the height of 80 and 84.5 cm from the bottom of the model. Therefore, the pressure recorded on this patch will be influenced

by a non-Gaussian wind flow. This position also prevents the measurements from interactions with the free flow that can occur near the top of the building.

Figure 4.1 and 4.2 represent the building model and the two measurement layout.

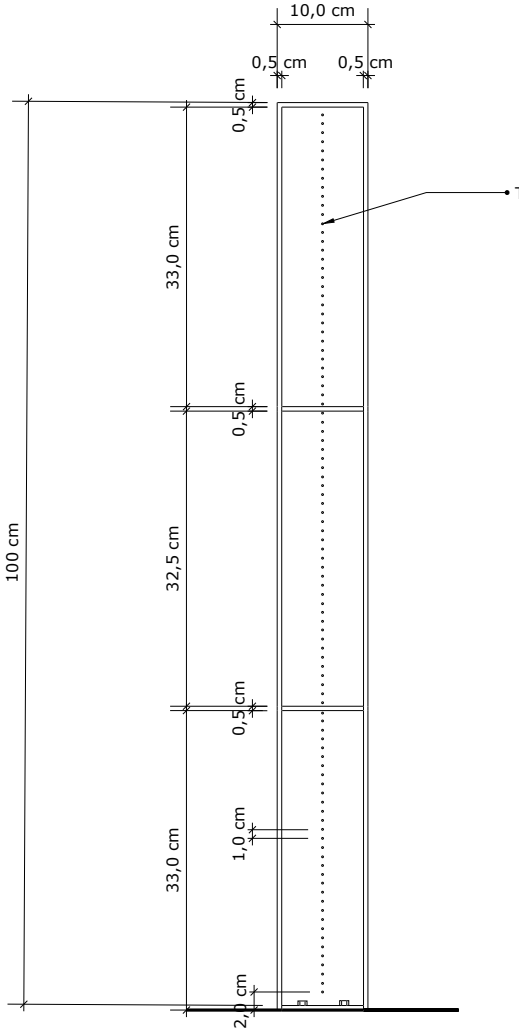

Figure 4.1 – Model profile view with the vertical measurement taps layout

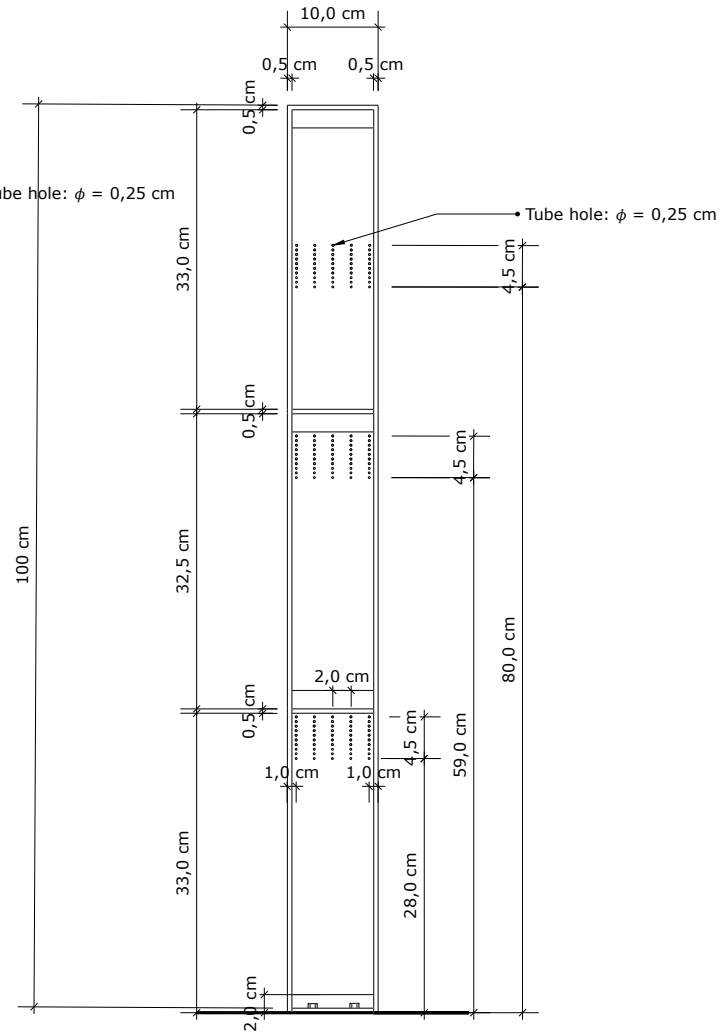

Figure 4.2 – Model profile view with the patches measurement taps layout

The model was built with 5 mm thick Plexiglas slabs. It has been designed to be rigid and to not experience vibrations during tests. Its dimensions are: height = $1m$, width = $0.1m$, depth = $0.1m$. The pressure measurements were collected using two miniature electronic pressure scanners. The first one is an ESP-64HD, with 64 channels and able to record 64 signals at a time. The second one is an ESP-32HD, with 32 channels and able to record 32 signals at a time. Inside each tap hole was glued a plastic tube 25 cm long. These tubes were connected to the channels of the pressure scanners as it is pictured on the figure 4.4.

Figure 4.3 – Picture of the model

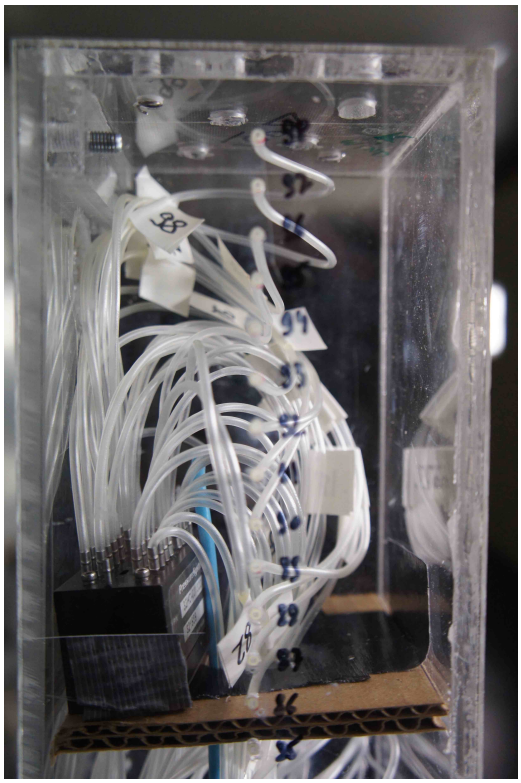

Figure 4.4 – Picture of the ESP-32HD pressure scanners connected to the plastic tubes

4.2 Pressure scanners analysis and correction

Before starting the pressure measurement campaign in the simulated atmospheric boundary layer, I checked the experimental equipment in the aerodynamic configuration (uniform wind velocity profile configuration) and without wind (wind-off configuration).

After some tests, I noticed that the ESP-64HD pressure scanners presented multiple defective channels. The signals recorded by some channels showed non-physical oscillations both in the wind-off and in the uniform velocity configurations. An example of these oscillations, observed during a wind-off test, is presented on figure 4.5. This figure represents each signal recorded by each channel of the ESP-64HD scanner in a different color.

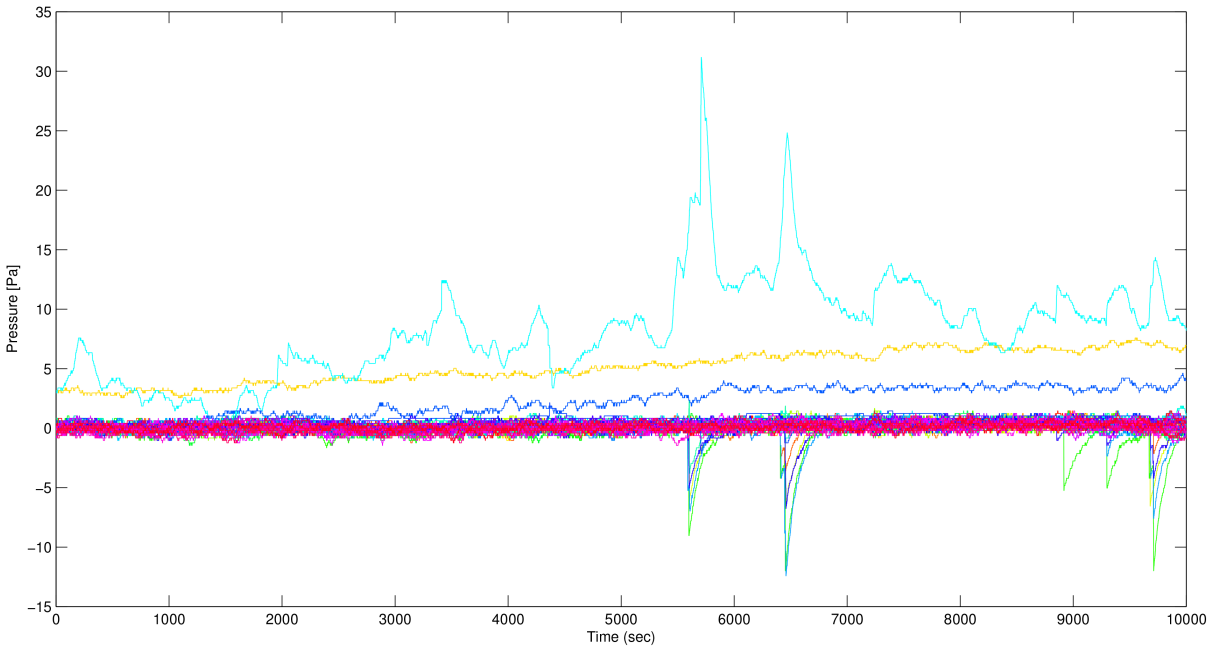

Figure 4.5 – ESP-64HD pressure signals recorded during a wind-off experiment

This phenomenon occurred for different channels as different tests were performed with no apparent logic. In order to detect the defective channels, I performed more than 30 experiments in the wind-off configuration and with different wind speeds. Then, I spotted every channels that experienced that phenomenon, and only the channels that never showed any non-physical oscillations were selected to record the pressure measurements. Finally, from the 64 available channels of the ESP-64HD pressure scanners, I kept the last 18 ones (channel 47 to 64). Therefore, I had 50 channels available with the two pressure scanners: 32 in the ESP-32HD, and 18 in the ESP-64HD. Both sensors were used to record pressure signals in each measurement layout.

Each patch contains 50 measurement taps numbered from 1 to 50 from the top left to the bottom right (see figure 4.6). The first 32 measurement taps were connected to the ESP-32HD pressure scanner and the last 18 to the ESP-64HD pressure scanner.

Regarding the vertical measurement layout, I divided the 98 measurement taps into two sub-layouts:

- Vertical 1: for the lower 50 taps. In this sub-layout, I connected the lower 18 taps to the ESP-64HD pressure scanner and the upper 32 taps to the ESP-32HD.
- Vertical 2: for the upper 48 taps with the first 16 taps connected to the ESP-64HD and the next 32 to the ESP-32HD pressure scanner.

Figure 4.7 represents the vertical measurement layout with the dashed yellow line delimiting the "vertical 1" and "vertical 2" sub-layouts. The blue line corresponds to measurement taps connected to the ESP-64HD scanner and the red one to the measurement taps connected to the ESP-32HD scanner.

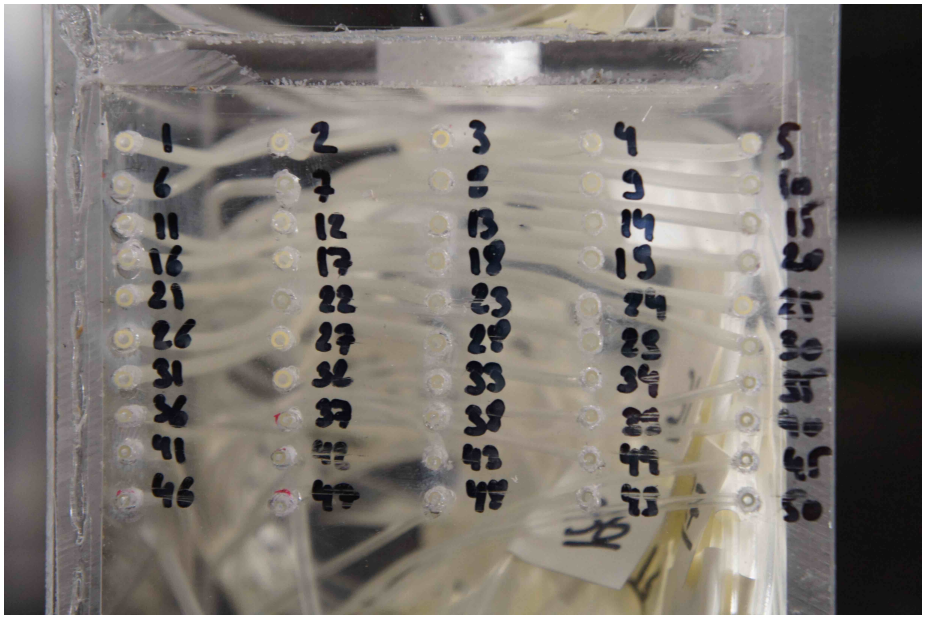

Figure 4.6 – Picture of the patches layout

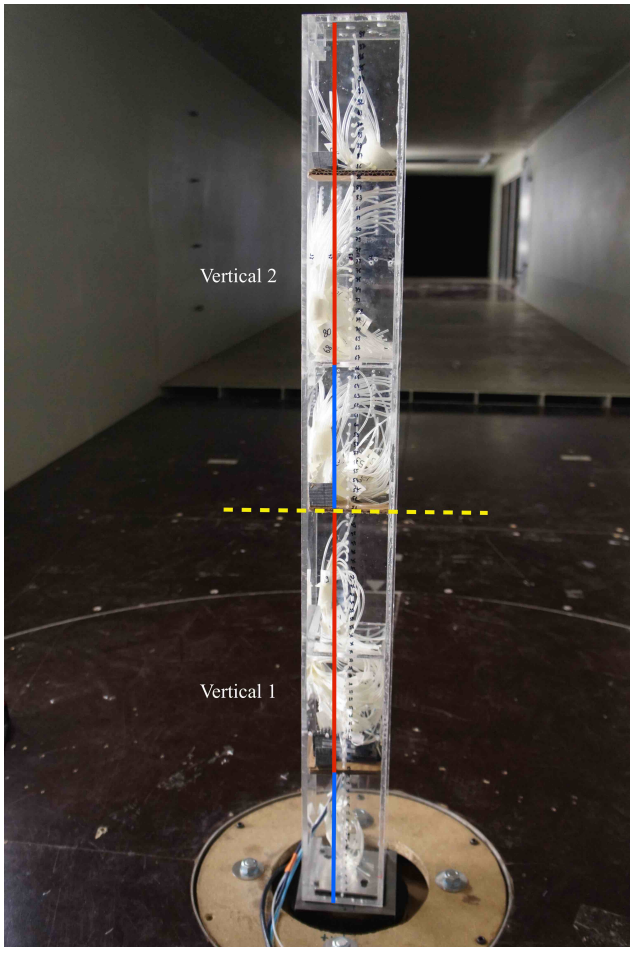

Figure 4.7 – Picture of the vertical measurement layout

Another phenomenon happened to influence the pressure signals given by the ESP-64HD scanner. Compared to the ESP-32HD, the 64 channels scanner presented a different transfer function.

In the patch measurement layout, the measurement tap couples: [31; 36], [32; 37], [28; 33], [29; 34], and [30; 35], formed 5 couples of signals recorded by the two scanners at a distance of only 0.5 cm far from each others. In that configuration, the pressure signals should be equal even if they were collected by two different scanners. However, this was clearly not the case. Figure 4.8 represent the pressure signals of the measurement taps 28 and 33 in the frequency domain (FFT of the two signals, from 0 to 250 Hz).

On this figure, we can see that both signals start at the same level. Then, the red one decreases more rapidly than the blue one and stays at a lower level in the high frequency range. This has been identified to be caused by the transfer function of the ESP-64HD. Consequently results from both scanners were not comparable. The transfer function of the ESP-64HD needed to be estimated and its response corrected. I computed the raw transfer function of the ESP-64HD by dividing, for each couple, the signal of the 64 channels scanner by the signal of the 32 channels scanner in the frequency domain. Then, I fitted this raw transfer function by a theoretical expression defined as:

$$FRF_{fitted} = a.e^{b.n} + c \tag{4.1}$$

With the coefficients: $a = 0.83$; $b = -0.97$; $c = 0.35$.

These coefficient have been computed using the method of least squares to match the raw transfer function of each couple individually in every configurations: 5 couples in 3 patches on 4 facades. Then I took the average of each coefficient. Figure 4.9 represents the raw and fitted transfer function of the ESP-64HD scanner for the measurement taps number 28 and 33 in the frequency domain.

This fitted FRF was then used to correct the pressure signals recorded by the 64 channels scanner. I simply divided the pressure signals in the frequency domain by this function.

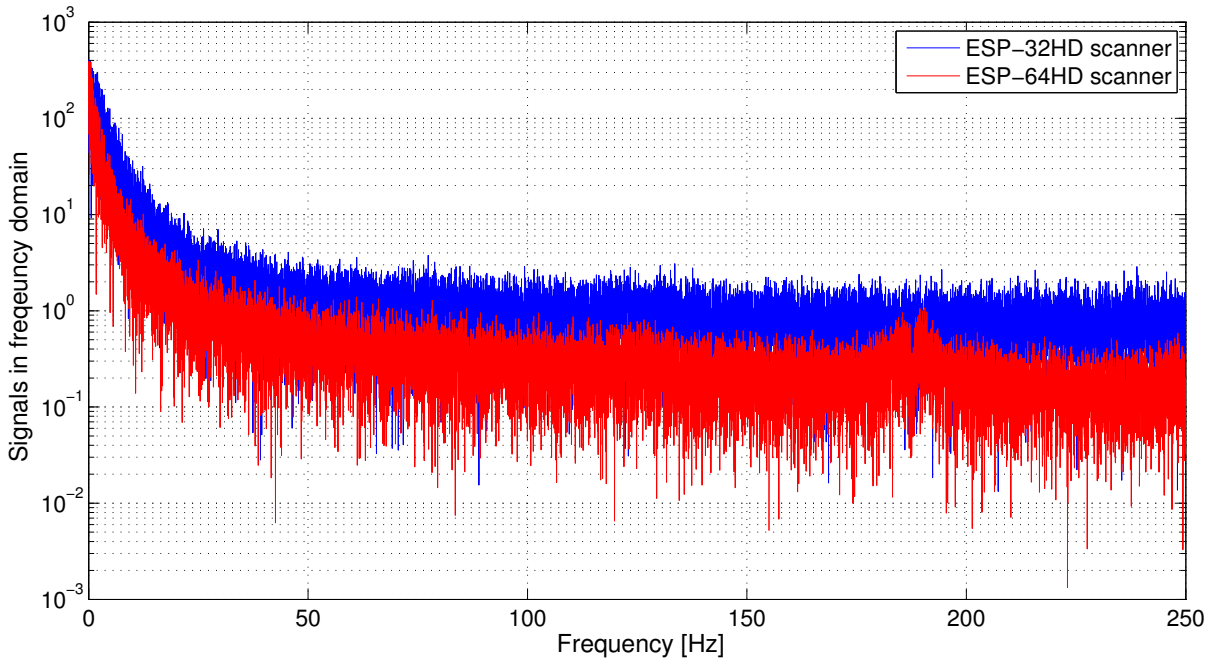

Figure 4.8 – Difference between the ESP-64HD and ESP-32HD scanners response in the frequency domain (measurement taps 28 and 33 with vertical logarithmic axis)

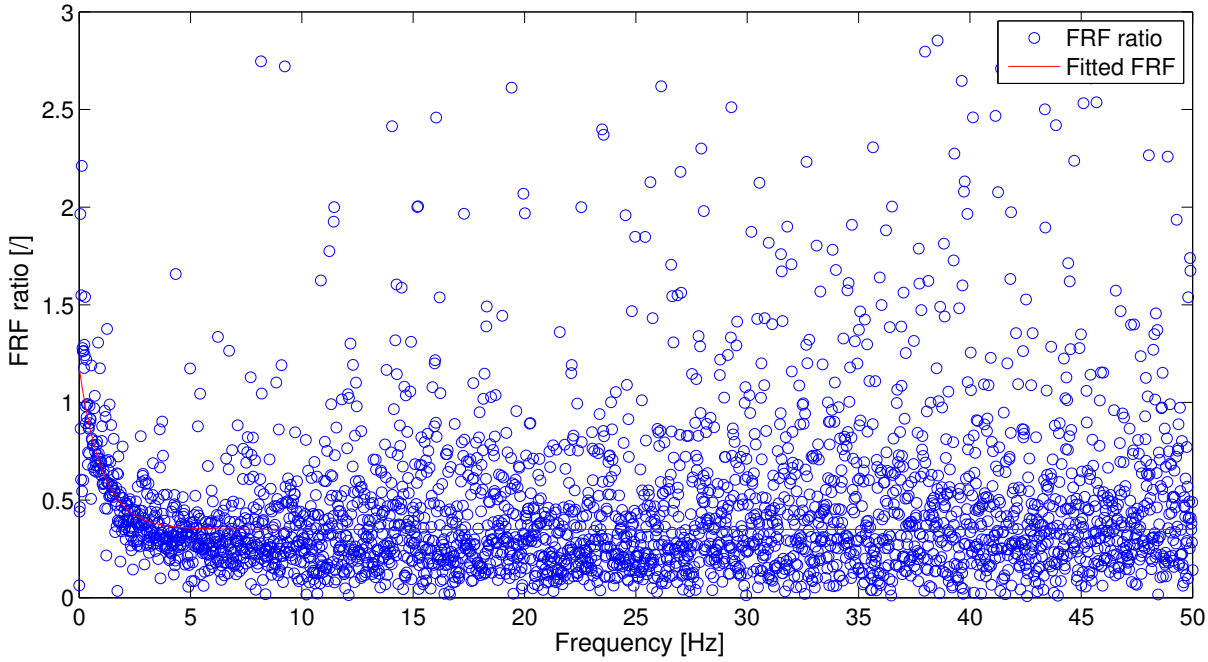

Figure 4.9 – Raw and fitted transfer function of the ESP-64HD scanner in the frequency domain (measurement taps 28 and 33)

4.3 Experimental methodology

Both the vertical and the patches measurement layouts are only present on one single side of the model. Therefore, in order to collect pressure signals on the four facades, the model was fixed on a turning table and turned accordingly. This method has been validated by [Gioffrè et al., 2001] and [Simiu and Scanlan, 1977] who indicate that the pressure measurements on a prismatic building facade are almost uncorrelated with those recorded on other faces, presenting typical correlation coefficients of the order of 0.1 to 0.2. The only drawback of this measurement technique is that I had to disconnect each channel of the pressure scanners and reconnect them to 50 other channels each time I needed to switch from one measurement layout to another. Thus, between patch 1, patch 2, patch 3, vertical 1 and vertical 2. I chose this method to keep a high density of measurement taps even if I only had 50 channels available.

During the preliminary tests, I also noted that the pressure scanners were sensitive to low wind velocity. In fact, the ESP-64HD is able to record pressure in the range of [-1 PSI to 1 PSI] = [-6895 Pa to 6895 Pa] and the ESP-32HD has a full scale pressure range of [-5 PSI to 5 PSI] = [-34474 Pa to 34474 Pa]. These scanners are calibrated to guaranty that the errors will stay lower than a 0.1 ‰. Therefore, the ESP-64HD has a precision of ± 0.7 Pa. In the same way, the ESP-32HD scanner has a precision of ± 3.4 Pa. This explains why I chose to record the pressure data at two relatively high reference wind speeds: 7.5 m/s and 9.8 m/s. Higher speeds could not be reached because above 13 m/s, the model began to experience vibrations.

Three wind angles of incidence: 0°, 15°, and 45° were also considered in order to study the influence of the wind direction on the pressure field.

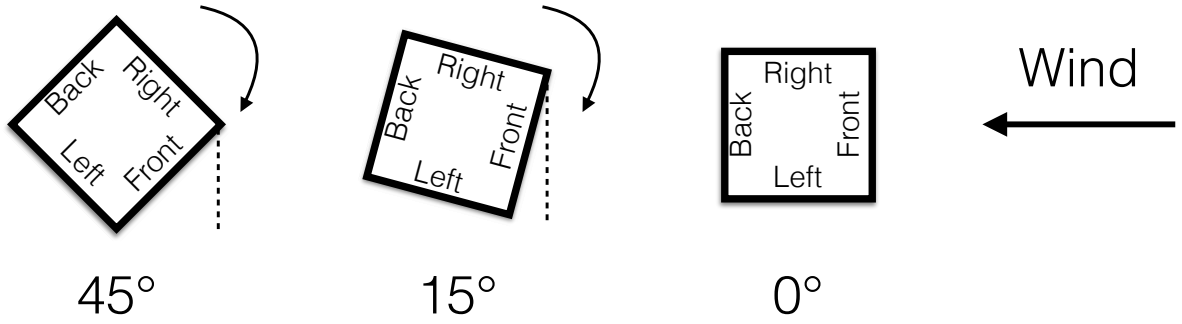

Figure 4.10 – Positions of the building model with respect to the wind flow in each configuration

The pressure measurements were recorded with an acquisition frequency of 500 Hz and during 60 seconds. With the scale factors summarized in table 4.1, a full scale duration of 10 minutes is equivalent to approximately 16 seconds at model scale with a wind speed of 9.8 m/s and to 21 seconds with a wind speed of 7.5 m/s.

Scale factor	Definition	Value
Length scale	$\epsilon_l = L_{model}/L_{prototype}$	1/100
Velocity scale at 7.5 m/s	$\epsilon_u = U_{model}/U_{prototype} = 7.5/25.9$	1/3.45
Velocity scale at 9.8 m/s	$\epsilon_u = U_{model}/U_{prototype} = 9.8/25.9$	1/2.64
Frequency scale at 7.5 m/s	$\epsilon_f = f_{model}/f_{prototype}$	29
Frequency scale at 9.8 m/s	$\epsilon_f = f_{model}/f_{prototype}$	38
Time scale at 7.5 m/s	$\epsilon_t = t_{model}/t_{prototype}$	1/29
Time scale at 9.8 m/s	$\epsilon_t = t_{model}/t_{prototype}$	1/38

Table 4.1 – Scale factors for the pressure measurements

Chapter 5

Analysis of pressure measurements

This chapter aims to summarize the results issued from the analysis of the pressure measurements recorded on the model. It is structured in two sections. The first one presents the measurements collected on the vertical layout in order to give some insights about the variation of the pressure field along the height of the model. The second section goes deeper into the details by analyzing the pressure recorded on the patches layout.

In both sections, I will first focus on the measurements collected with a wind flow perpendicular to the windward facade. Then I will analyze the influence of the wind angle of incidence on the pressure field.

The pressure data are presented in this thesis as non-dimensional coefficients of pressure (C_P's) defined as:

$$C_P(h) = \frac{P(h) - P(\infty)}{1/2\rho V_{ref}^2} \tag{5.1}$$

$P(\infty)$ is the free stream static pressure recorded by a pitot tube placed in the wind tunnel at a height of 1.45 m, 1.5 m upstream of the model. V_{ref} is the wind velocity at the reference height (model height).

In this chapter, I will use different terms to denote the four facades of the model. In order to avoid any confusion, I need to introduce them once and for all. The terminology "front side" denotes the windward facade. The words "back side" means leeward facade. Finally, the words left and right side denote respectively the facades on the left and the right of the windward facade. This terminology stays the same when considering different wind directions.

As expected from the analysis of the three atmospheric boundary layers in section 3.6, the pressure data differ dimly from one ABL to another. Exactly the same conclusions can be drawn from the different ABL's. Therefore, I will only present the results from ABL2 in this thesis. In the same way, I will present the measurements recorded with a wind speed of 7.5 m/s at the reference height. Note that each conclusion is confirmed by the measurement recorded at 9.8 m/s.

5.1 Pressure measurements recorded on the vertical layout

5.1.1 Wind flow perpendicular to the windward facade

Figure 5.1 shows the mean pressure profiles recorded on the four facades of the vertical layout with a wind incidence of 0°. First we can see that a positive pressure only acts upon the front side. According to [Simiu and Scanlan, 1977], for a reasonably high Reynolds number, a square profile is seen to produce flow separation at the edges of the windward facade, followed by a wide turbulent wake (see figure 5.5 and 5.6). We can also notice that on each side, the pressure grows in absolute value with the height. This is simply due to the wind velocity profile that increase with the altitude in the ABL. Concerning the left and right sides, we observe a steep variation in the first 8 m of the profile. In this region, wind flow interactions with the floor of the wind tunnel occur and prevent a clear flow separation at the edges of the windward face. The left and right sides show lower negative values than on the back side. In fact, wind velocity reaches higher values in the vicinity of the lateral facades than near the back side, the pressure recorded on theses faces are therefore lower. The mean pressure coefficient of this section are consistent with those obtained by [Gioffrè et al., 2001] in wind tunnel and those of [Huanga et al., 2007] computed with numerical simulation.

Figure 5.2 indicates that the standard deviation values of the front and back sides are nearly equivalent. They increase in the first 30 m and then stay relatively constant from 30 m to the top of the model. The reason of this shape is explained in section 6.1 and is due to the ratio between the mean and standard deviation values of the incident wind. We also notice that the fluctuations around the mean pressure values are larger on the left and right sides than on the other facades. This can be explained by the formation of vortices inside the shear layers initiated at the edges of the windward frontage. If we focus on the lateral sides profiles, we see that the standard deviation stays constant between 8 and 50 m and then decreases slightly in the upper half of the model, probably due to the reduction of the turbulence. We also observe the same rapid variation than observed on the mean profile in the first 8 m. Vortices have difficulties developing in the vicinity of the ground.

The skewness profiles of the four facades are shown on figure 5.3. The front side pressure measurements present a skewness that decreases from 0.5 at the bottom to -1 at the top of the model. On the lateral and back facades, we can see that the skewness oscillates around -0.5 on the entire height. The wind flow obviously influences the pressure on the front side whereas the other faces seem unaffected. This subject is discussed in section 6.1. Once again, the interactions with the floor of the wind tunnel cause variations in the first meters of the lateral facades.

As a general observation, it comes out from figure 5.4 that the kurtosis of the pressure measurements of each facade stays relatively close to the Gaussian value of 3. However, small deviations can be observed on the lateral facades. The kurtosis recorded on the front side also deviates near the top of the model. This is due to the non-gaussianity in the incident wind flow. As noticed for the other statistical moments and for the same reason, the kurtosis of the lateral facades change rapidly at the bottom of the model.

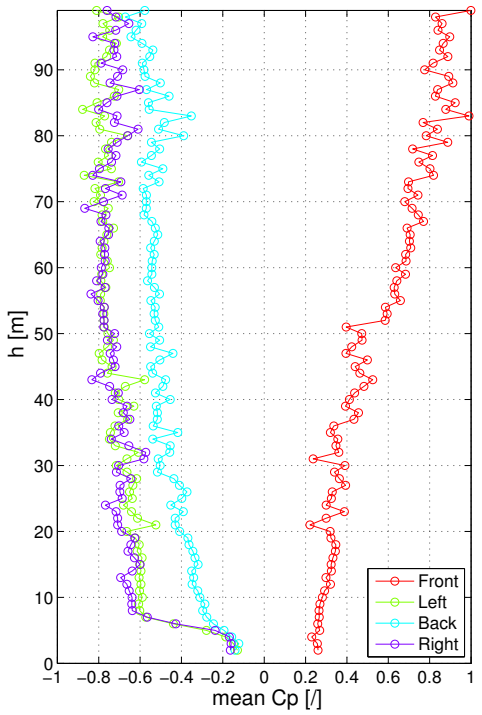

Figure 5.1 – Mean C_P profile on each facade with 0° incident wind

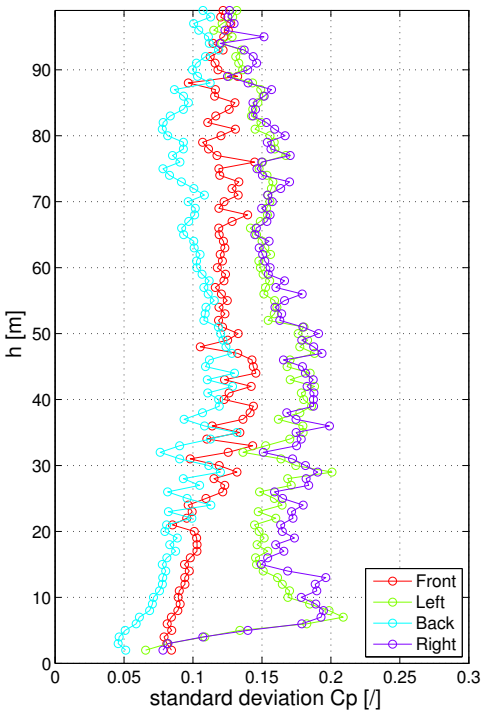

Figure 5.2 – Standard deviation C_P profile on each facade with 0° incident wind

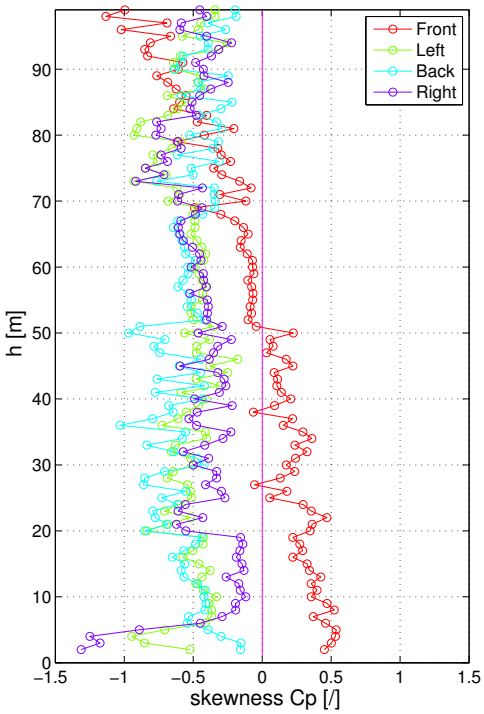

Figure 5.3 – Skewness C_P profile on each facade with 0° incident wind

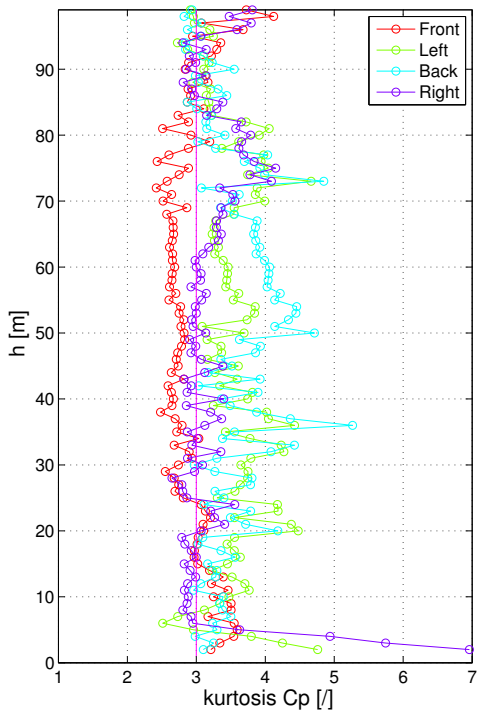

Figure 5.4 – Kurtosis C_P profile on each facade with 0° incident wind

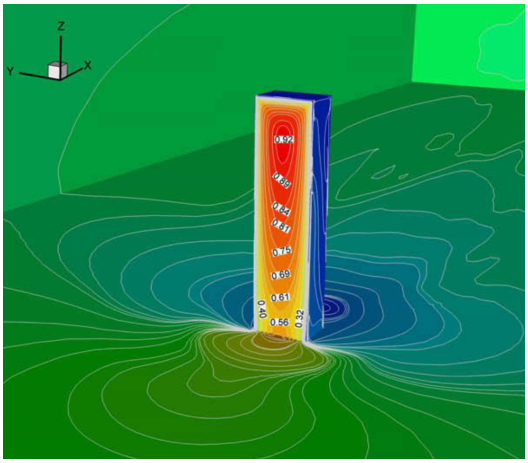

Figure 5.5 – Distribution of mean pressure coefficient over the building walls taken from [Braun and Awruch, 2009]

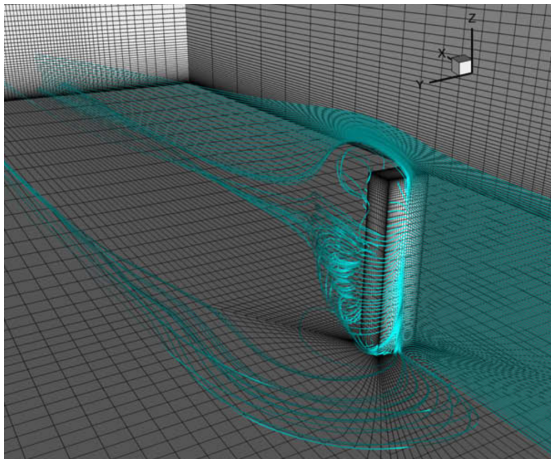

Figure 5.6 – wind streamlines around a prismatic building taken from [Braun and Awruch, 2009]

Figure 5.7 represents a pressure record on the left facade as a function of time. In the separated and vortex flow regions, vortices associated with the wind flow around the model induce a suction that is reflected in the large fluctuations as well as in the sharp spikes observed on this figure [Gioffrè et al., 2001]. The same authors also explain that the deviation from the Gaussian model in those regions can find its physical explanation in the combination of the wind process (wide band) and the vortex-shedding process (narrow band).

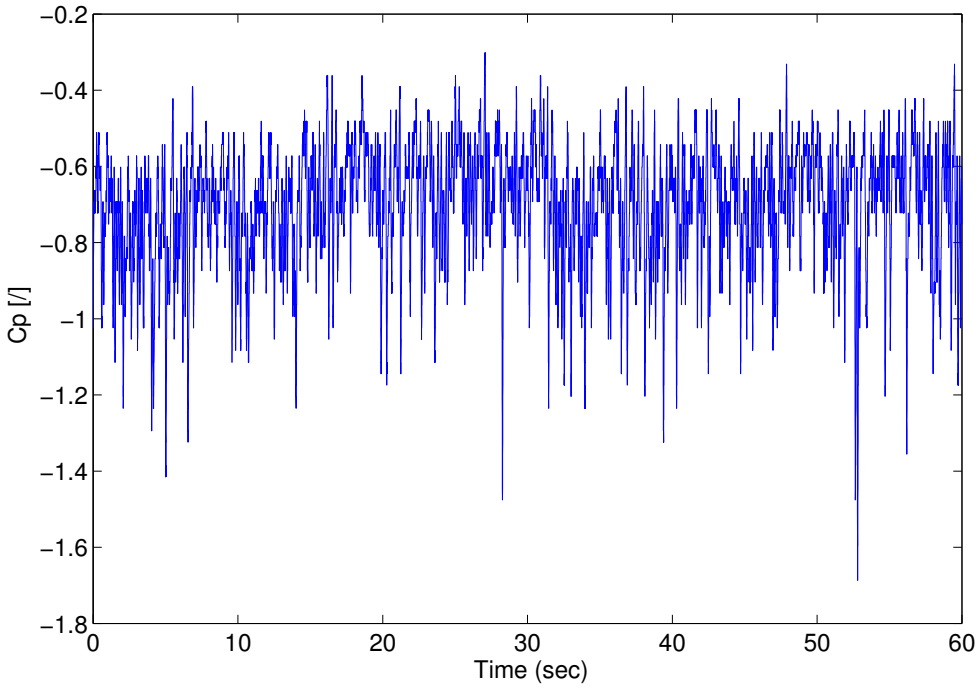

Figure 5.7 – Coefficient of pressure recorded on the left facade at 30 m

The skewness and kurtosis influence the statistical distribution of the pressure measurements, represented by their probability density functions. Regarding the lateral and back facades, the distributions are clearly non-gaussian and left-tailed on the entire height of the model. Thus, the probability to find larger negative pressures on these facades is larger than predicted by a Gaussian model. The kurtosis also influences the peakedness of their distributions. On the front side, the kurtosis only diverts from the Gaussian value at the top of the model. Therefore, the parameter that mainly influences the non-gausiannity is the skewness. In the first half of the model height, the skewness is positive and the probability density functions of the pressure signals are right-tailed. Around 50 m, the skewness is close to the Gaussian value of 0 and the distribution can be considered Gaussian. In the upper half, the skewness decreases in the negative values and the distributions are therefore left-tailed. This means that the probability to find large positive pressures on the front side is underestimated by a Gaussian model at low altitudes and overestimated at higher altitudes.

Note that on a facade where the pressure is positive, a right-tailed PDF implies that high positive values of pressure have a higher probability of occurrence. This situation is unfavorable to the design of structure and structural elements because it leads to consider a higher peak factor than the Gaussian would predict (prescribed equal to 3.5 in the Eurocode 1.4). The same argument can be made about a left-tailed PDF on facades where the pressure is negative.

As it has been done for the velocity measurements in section 3.4, I will now characterize the frequency content of the pressure data using their power spectral density functions. The results on figure 5.8 have been normalized with the variance of the considered signals and plotted on a vertical logarithmic axis. We can see that almost the entire energy is contained in the low frequency (0 - 50 Hz). More interestingly, the vortex shedding effect can be observed through peaks around 10 Hz on the lateral facades. Under 30 m, the turbulence seems to disrupt the phenomenon and the spikes are attenuated on the first two graphs. At the top of the model, vortex shedding also seems to be influenced by interactions with the free stream around the sharp edges of the model rooftop.

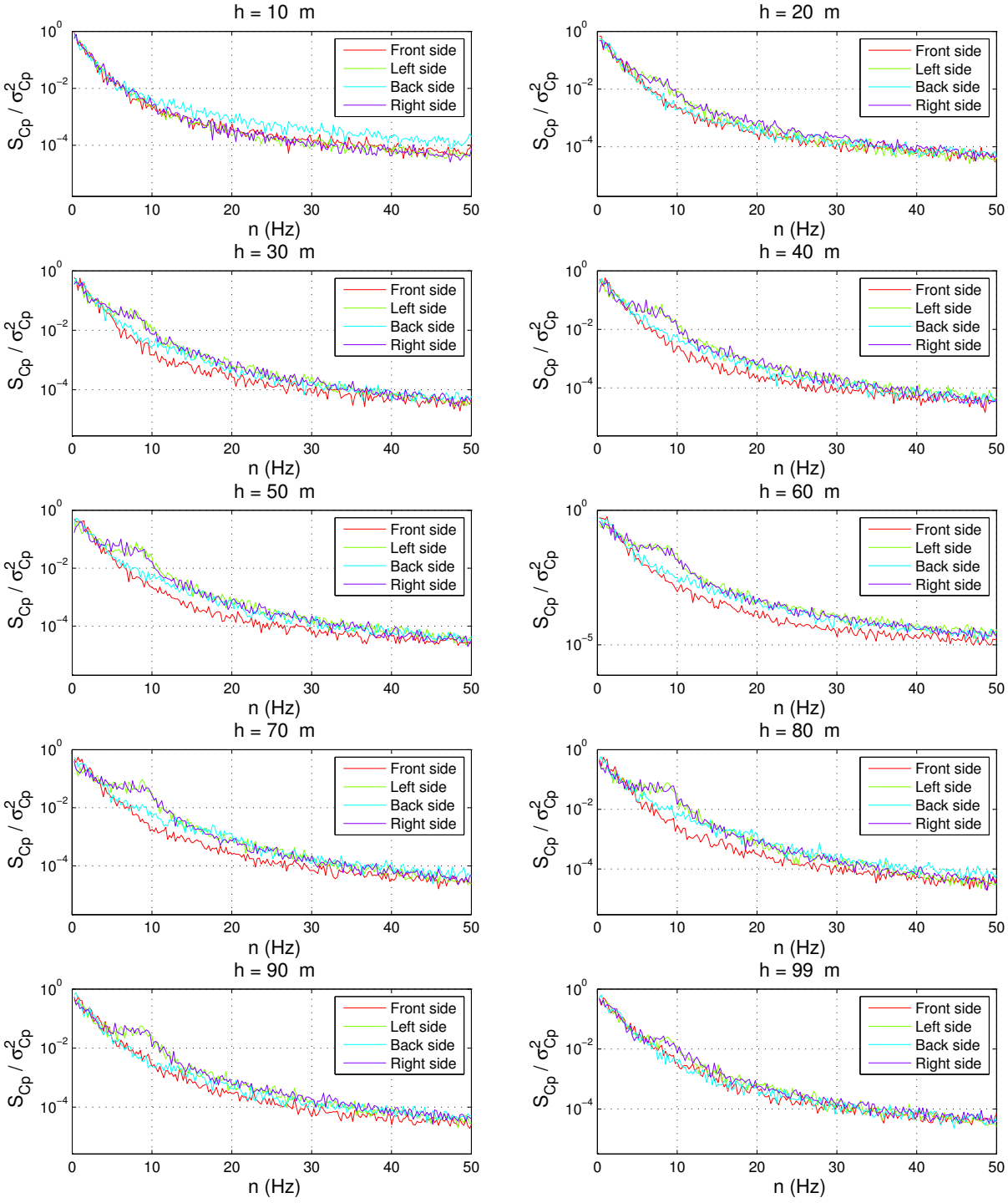

Figure 5.8 – Normalized spectral density function of C_P signals on each facade with 0° incident wind (vertical logarithmic axis)

The frequency where the vortex shedding peak appears increases with the height (around 8 to 10 Hz on the graphs of figure 5.8). This frequency can be computed analytically with the following equation:

$$f_{VK}(h) = \frac{St.U(h)}{D} \tag{5.2}$$

Considering D the characteristic length of the model (the width = 0.1 m). St is the Strouhal number equal to 0.12 for a square shaped model. U is the mean wind velocity.

Results are presented on figure 5.9 and appear to slightly overestimate the frequency observed with the pressure measurements. This small difference is probably due to the Strouhal number of the experimental set-up that is shortly under 0.12.

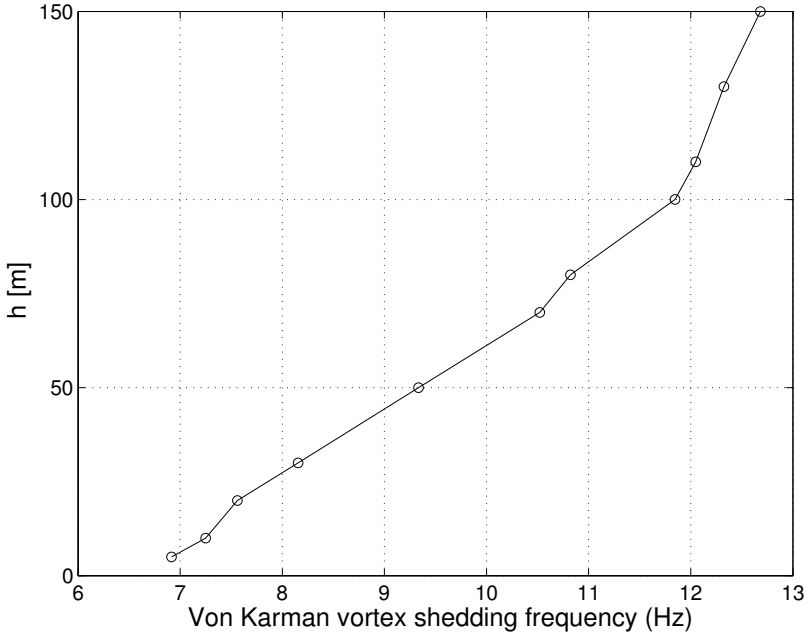

Figure 5.9 – Von Karman vortex shedding frequency

5.1.2 Influence of the wind angle of incidence

This section describes the influence of the wind direction on the first four statistical moments of the pressure measurements. Only the data recorded on the front and right sides are presented. Indeed, the back facade stays in the wake for each wind direction, results are therefore very similar. Then, angles of incidence of 15° and 45° place also the left face of the model in the wake and the results become analogous to those recorded on the back side. One last comment about this section is that the profiles of the front and right side are the same at 45°. They are depicted on both sets of graphs to enable an easier comparison between each wind incidence configuration.

On figure 5.10, we can see that changing the wind direction to 15° does not influence the mean pressure profile on the front side. With a wind angle of incidence of 45° the values decrease because the facade supports less wind pressure due to its relative orientation to the wind direction. Indeed, the wind flow is separated more smoothly and does not stop on the front facade. At 15° the phenomenon in the first 8 m appears less marked on the right side and the mean values decrease gradually on the entire height of the model as depicted on figure 5.11. With a wind direction of 45° with respect to the model, the right side undergoes positive pressure.

Nearly the same comments can be made about the standard deviation presented on figure 5.12. Actually, changing the wind angle of incidence to 15° does not affect the pressure on the front side. It is only at 45° that the standard deviation values decrease following the same trends as the mean profile. On figure 5.13 we see that at 15 degrees, the pressure fluctuations on the right side are larger than at 0°. The pressure field on this face is more influenced by the incident wind flow due to its orientation and the profile can once more be explained by the theory developed in section 6.1.

By looking at figure 5.14 and 5.16, we can affirm that the skewness and kurtosis of the front side measurements are not affected by variations of the wind direction. If we now focus on the other two figures, 5.15 and 5.17, we see that unlike the kurtosis that stay unchanged, the third statistical moment of the right side measurements is heavily affected by the different wind incidences.

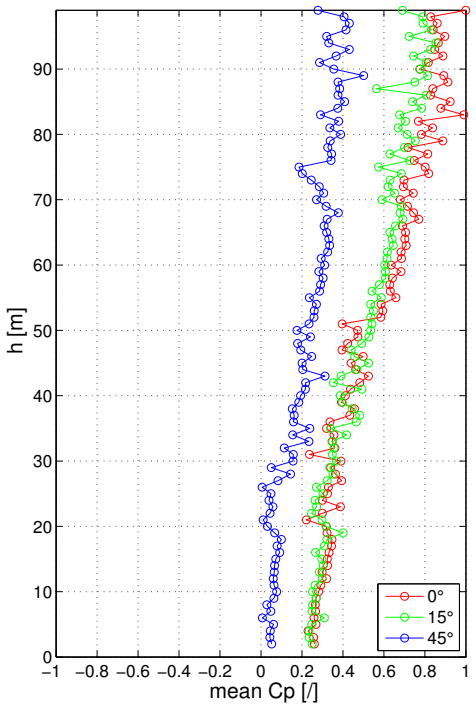

Figure 5.10 – Influence of the wind direction on the mean C_P profile of the front side

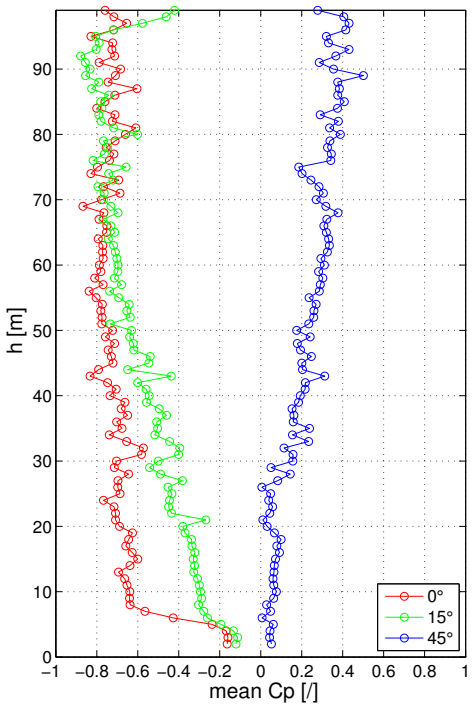

Figure 5.11 – Influence of the wind direction on the mean C_P profile of the right side

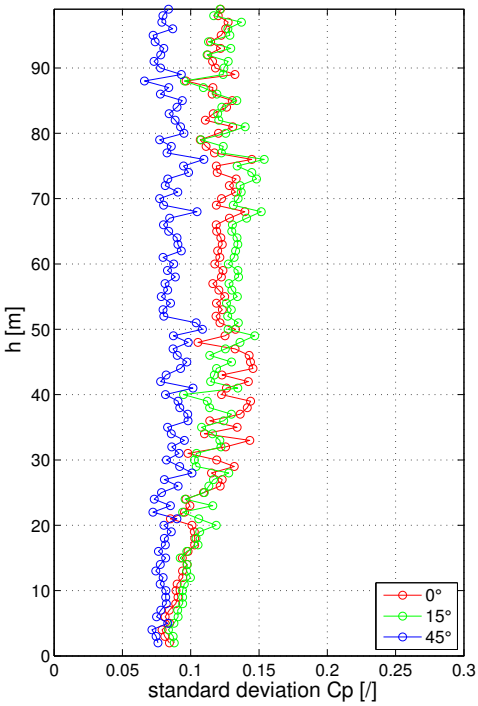

Figure 5.12 – Influence of the wind direction on the std C_P profile of the front side

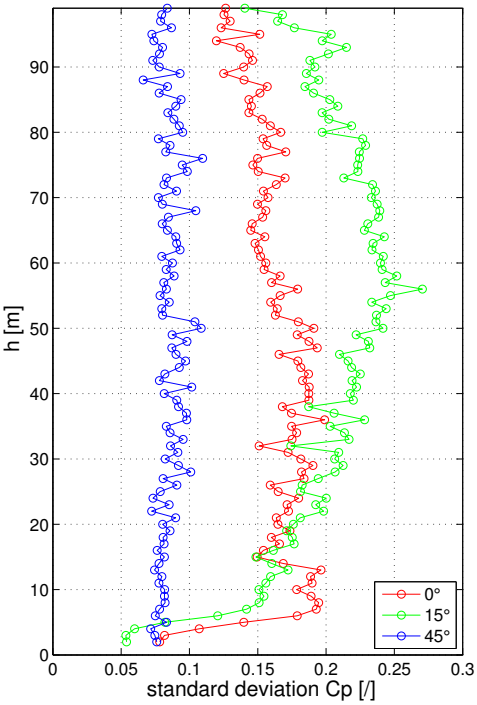

Figure 5.13 – Influence of the wind direction on the std C_P profile of the right side

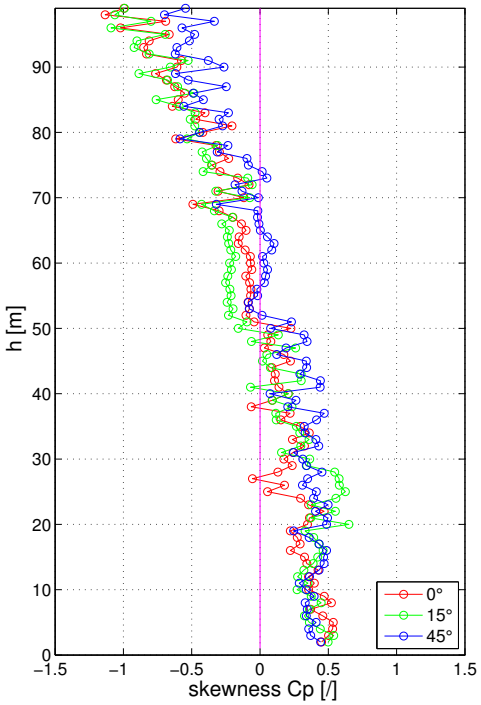

Figure 5.14 – Influence of the wind direction on the skewness C_P profile of the front side

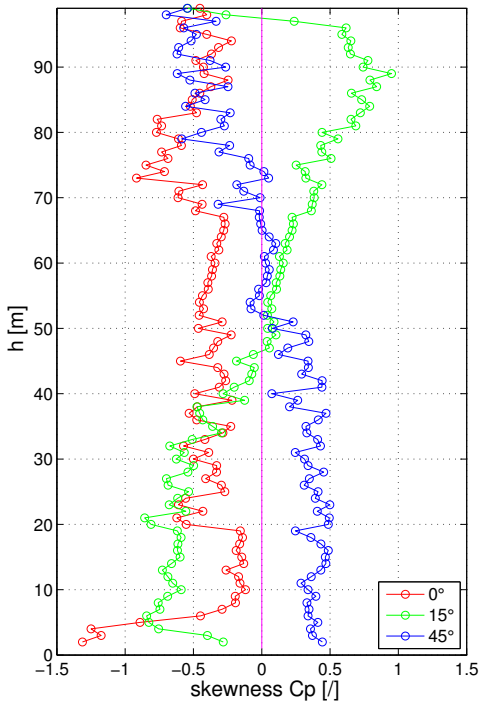

Figure 5.15 – Influence of the wind direction on the skewness C_P profile of the right side

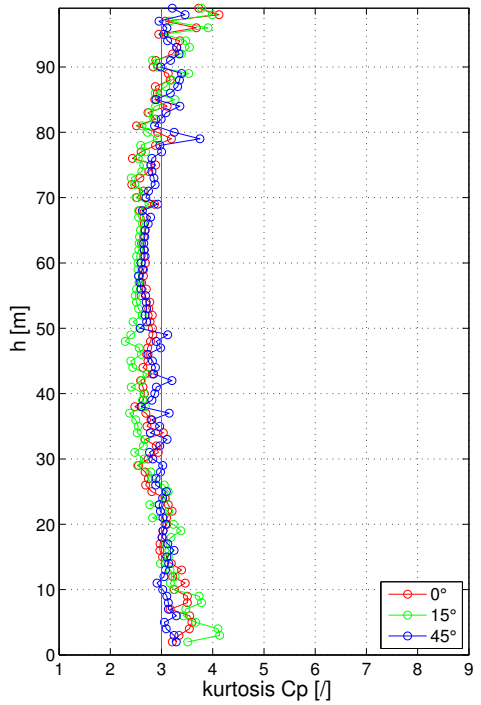

Figure 5.16 – Influence of the wind direction on the kurtosis C_P profile of the front side

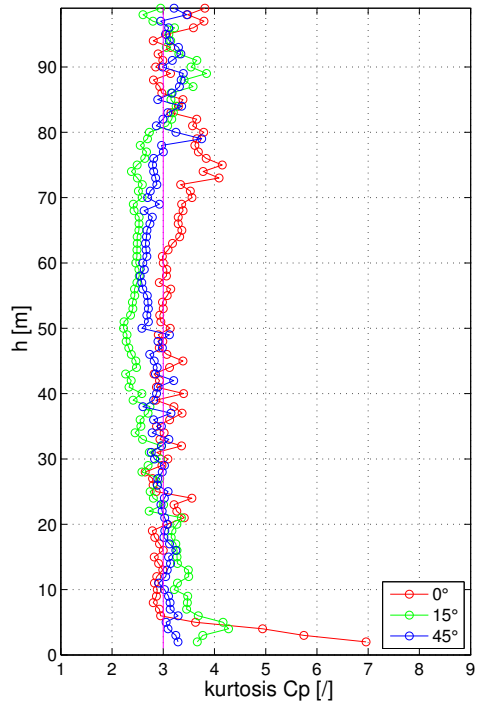

Figure 5.17 – Influence of the wind direction on the kurtosis C_P profile of the right side

The wind direction also influences the frequency distribution of the pressure measurements. By comparing figures 5.18 and 5.19, we can see that the vortex shedding effect disappears on the right facade when the models is turned at 15 and 45 degrees whereas it remains visible on the left side.

At 45°, the right side undergoes positive pressure. Vortices are therefore created behind the right face and cannot be seen in the frequency content. However, the orientation of the left side enable to record the pressure fluctuations induced by the vortex shedding effect.

At 15 degrees, vortex shedding vanishes on the right side while it clearly appears on the left one. The negative pressure that acts on both facades indicates that the flow separation have already occurred. According to [Dutta, 2006] and [Panigrahi et al., 2008], such wind direction leads to an asymmetric flow separation: the shear layer of the left side diverges away from the facade, whereas the shear layer of the right facade remains close to the model surface. This closeness prevents the vortices from developing in the vicinity of the right facade.

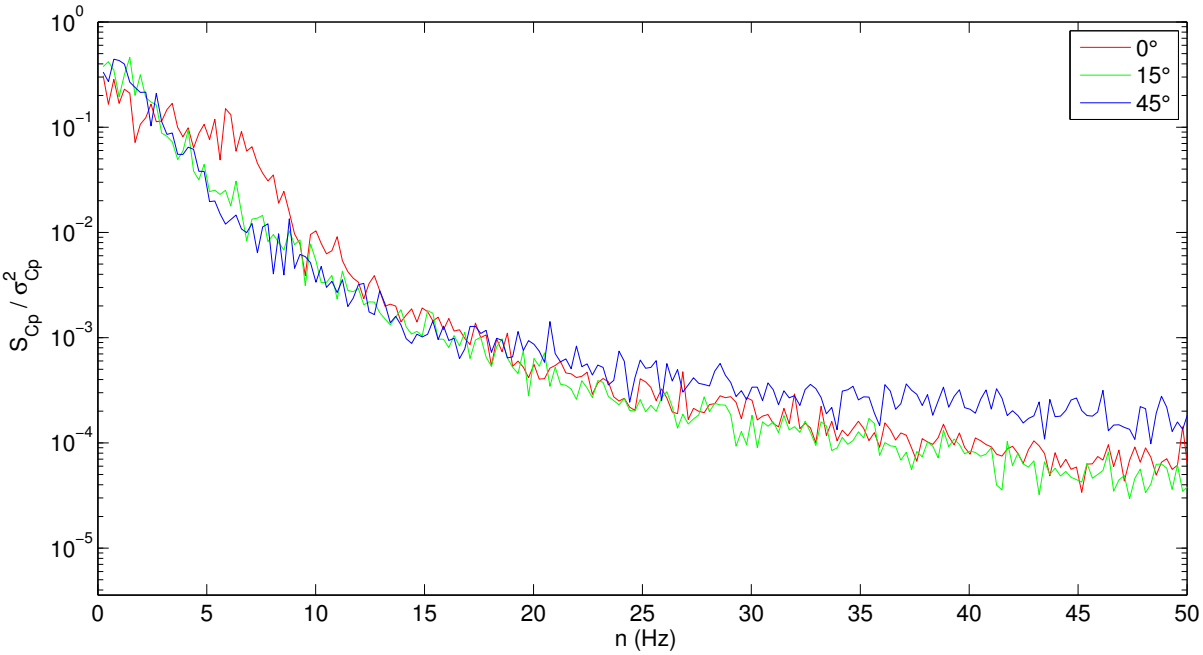

Figure 5.18 – Influence of the wind direction on the normalized spectral density function of the pressure recorded on the right side at 70 m

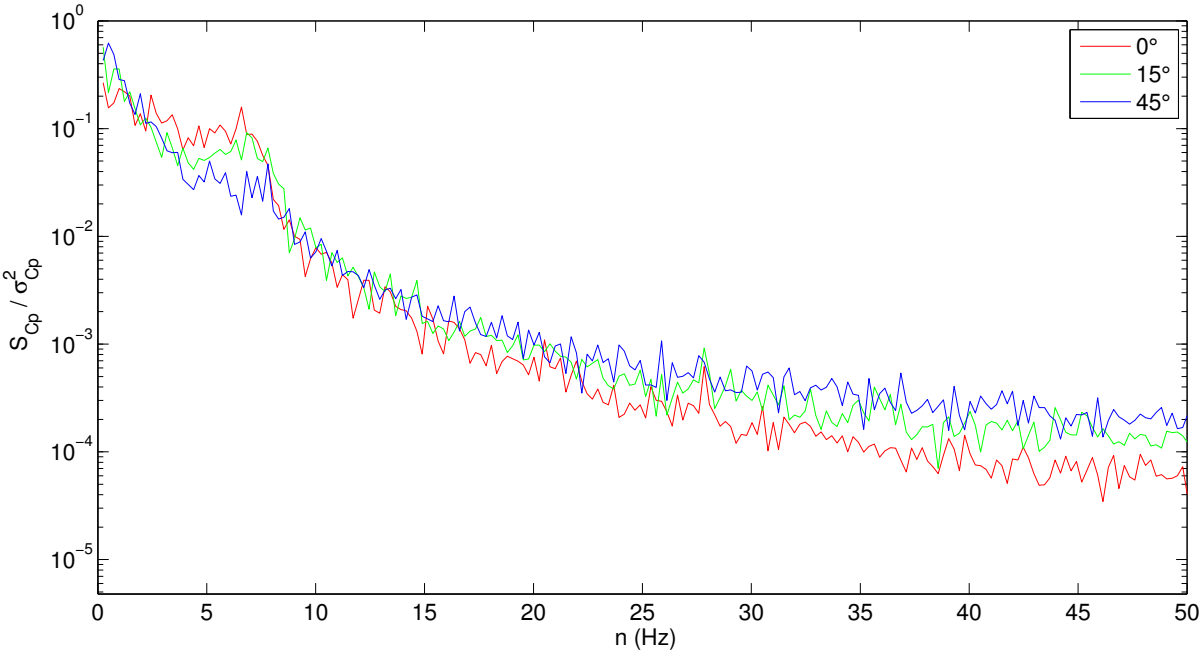

Figure 5.19 – Influence of the wind direction on the normalized spectral density function of the pressure recorded on the left side at 70 m

5.2 Pressure measurements recorded on the patches layout

In this section, I will describe the pressure measurements recorded on the patches layout. The purpose of the analysis is to understand the variations of the four statistical moments along the width of each facade.

First, a comment needs to be made about the representation of the results. This section uses a type of graph in which the x-axis represents the 20 rows of the layout. As a reminder, each facade contains five rows along the width of the model. These rows are plotted in the following order: front, right, back, left sides as depicted on figure 5.20. Therefore the connected dots on the graph represent, by colors, the profiles along the width of the model for the four facades.

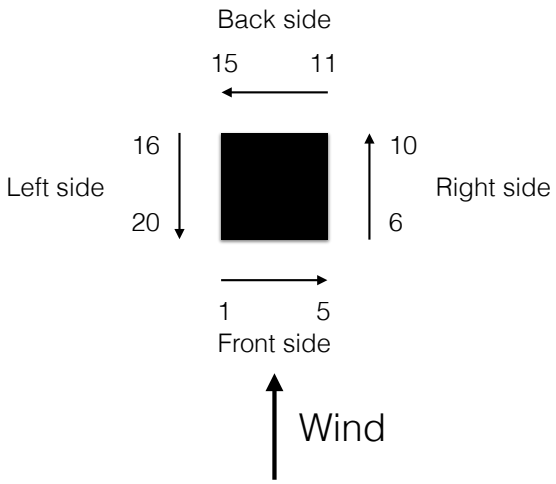

Figure 5.20 – Rows numbering convention for the type of graph used to picture the results of the patches layout

5.2.1 Wind flow perpendicular to the windward facade

the values of the four statistical moments happen to be very similar along the height of each patches. In order to make the graph clearer, I will only present the profiles recorded at line 5 of the patches, which correspond to the middle height of each patch.

On figure 5.21 we can see that the pressure recorded on the front side decreases gradually from the center to the edges of the facades, often referred as a "C shape" or "horseshoe shape". This profile is due to the wind velocity that nearly stops at the center of the facade and then accelerates toward the corners of the model. On the lateral and back sides, the pressure stays relatively constant along the width. We also observe on these frontages that the pressure seems to be constant for the three patches at the edges where the flow separation occurs (leading edges: row number 6 and 20). We can finally notice that results are in line with those of the vertical layout. The mean pressure increases in

absolute value from patch 1 to 3 and is lower on the lateral sides than on the back one. The mean pressure profiles along the width of the model are consistent with the results of [Gioffrè et al., 2001] obtained in wind tunnel and those of [Huanga et al., 2007] who used numerical simulation.

Figure 5.22 confirms the comment made about the vertical layout: the variations around the mean values are larger on the lateral sides than on the windward and leeward facades. The front side presents standard deviation values that clearly follows a "C shape" as observed on the mean profile. This profile is inverted on the back face and flattened. This can be explain by the pressure fluctuations induced by the vortices that develop near the edges of this facade. The lateral frontages also show similar profiles but skewed toward their leading edges. In this case, the vortex shedding effect is combined to the suction generated by the flow acceleration in this zone.

Figure 5.23 presents the skewness of the pressure measurements recorded on each facade. As for the first two statistical moments, the skewness of the front side measurements is higher in absolute value at the center and decrease toward the edges. According to [Gioffrè et al., 2001], non-Gaussian distributions are generally observed at taps located near the windward edges of the building in separated flow as well as in vortex flow. This is what we observe here, with high skewness values near the windward edges on the lateral and back facades (rows 6 and 7; 14 and 15; 20).

Figure 5.24 shows that the kurtosis of the windward frontage is relatively constant along the width. On the lateral and leeward facade, the kurtosis profiles confirm that non-Gaussian distributions are observed near the windward edges in separated and vortex flows.

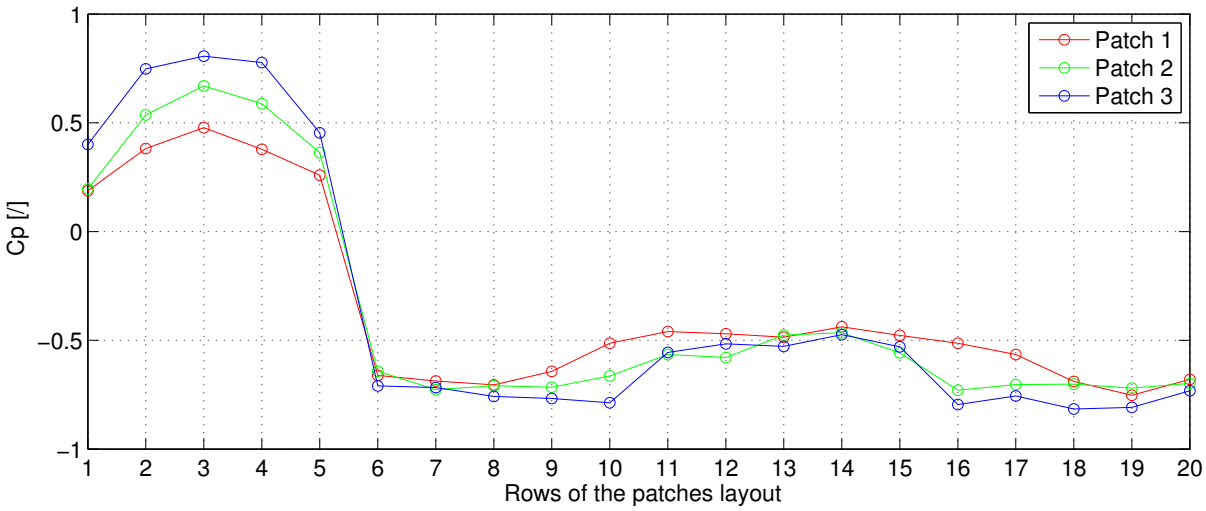

Figure 5.21 – Mean C_P profile on each facade with 0° incident wind

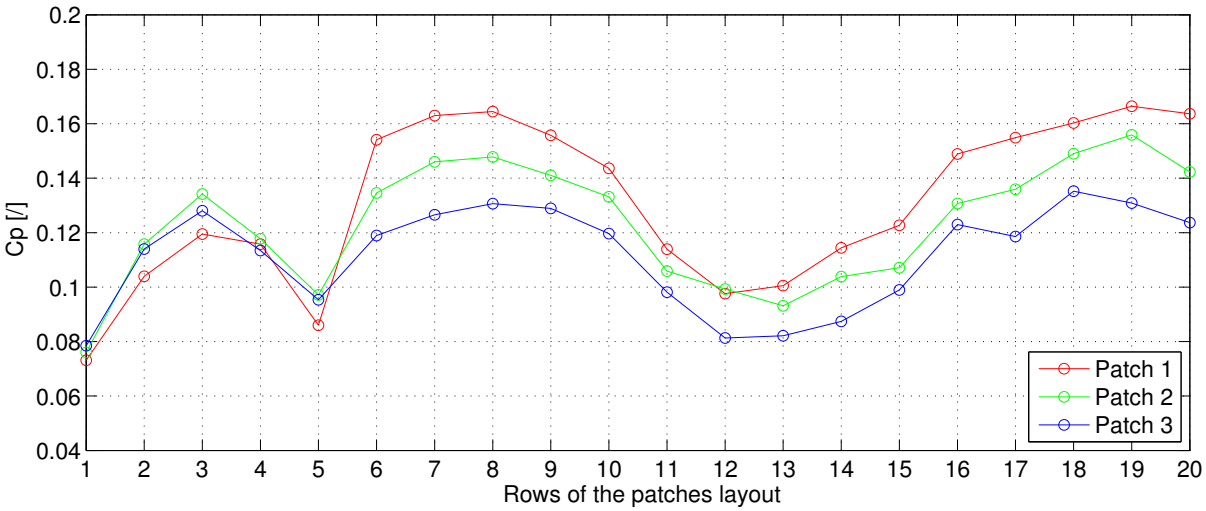

Figure 5.22 – Standard deviation C_P profile on each facade with 0° incident wind

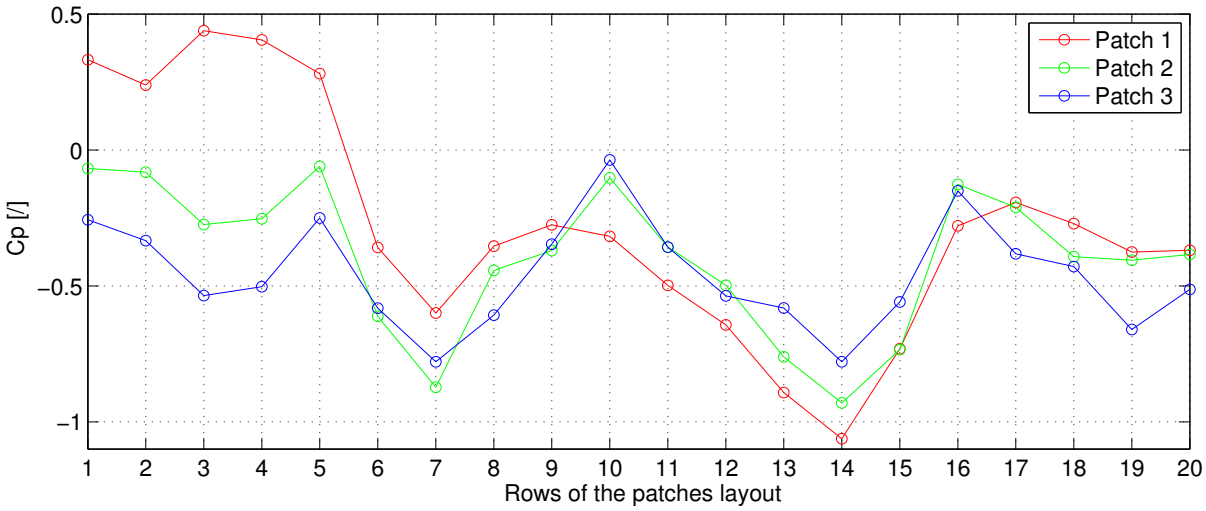

Figure 5.23 – Skewness C_P profile on each facade with 0° incident wind

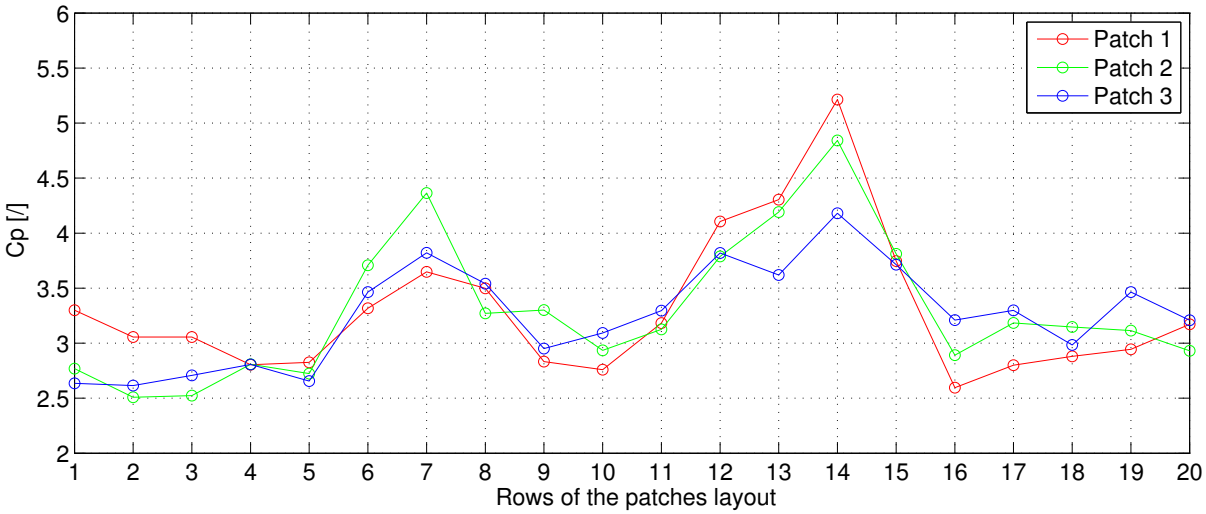

Figure 5.24 – Kurtosis deviation C_P profile on each facade with 0° incident wind

5.2.2 Influence of the wind angle of incidence

In the same way as it has been done for the vertical layout, this section aims to describe the influence of the wind direction on the pressure recorded on the patches layout. I will only present the data recorded on the first patch but the same conclusions can be drawn from the other ones. As in section 5.1.2, the profile of the front and right side are the same at 45°, they are depicted on the following graphs to enable an easier comparison between each wind incidence configuration.

Figure 5.25 confirms multiple comments made about the vertical layout. First, turning the model by an angle of 15 degrees does not influence the mean pressure on the front and back facades. We can also see that the pressure recorded on the left side become close to the values of the back side. On the right face, the pressure decreases in absolute value. At 45 degrees, the pressure on the front side decreases from its heading to its tailing edges. It even becomes negative near the flow separation location (row 1). Finally, we see that the pressure on the back and left sides are unaffected by the change in the wind direction and that the pressure on the right facade becomes positive.

Figure 5.26 shows that changing the wind direction from 0 to 15 and then 45 degrees seems to decrease the standard deviation on each facade, excepted at the center of the right facade at 15°. This has already been observed on the vertical layout. On the front side, the reduction of the pressure fluctuation is only visible at 45 degrees.

Concerning the skewness and the kurtosis represented on figure 5.27 and 5.28 we see that the wind direction has no influence on the front side. For the lateral and back facades, the effect of the wind direction is unclear.

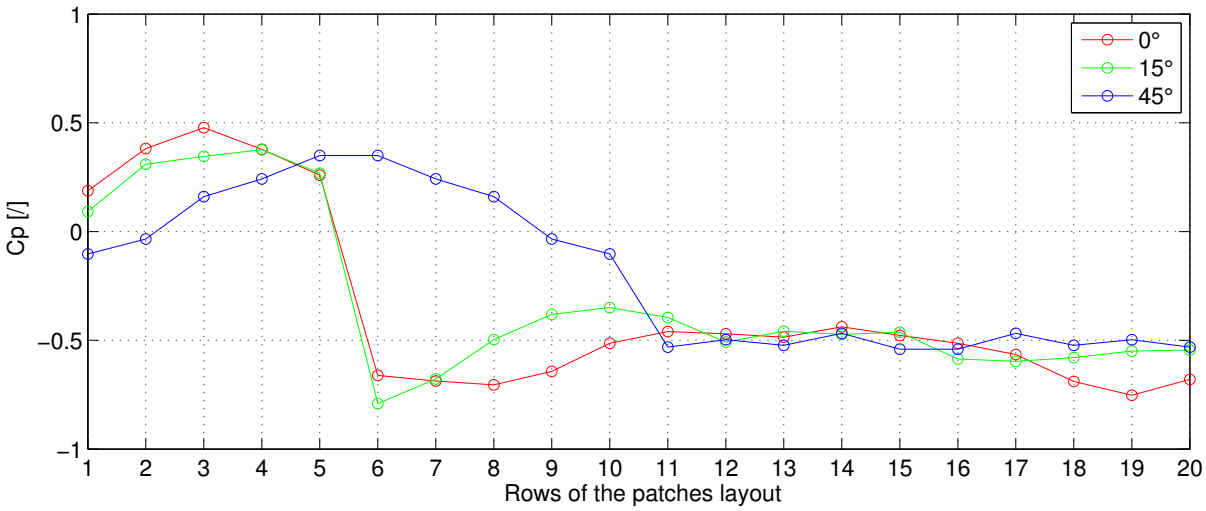

Figure 5.25 – Influence of the wind direction on the mean C_P profile along the width of each facade

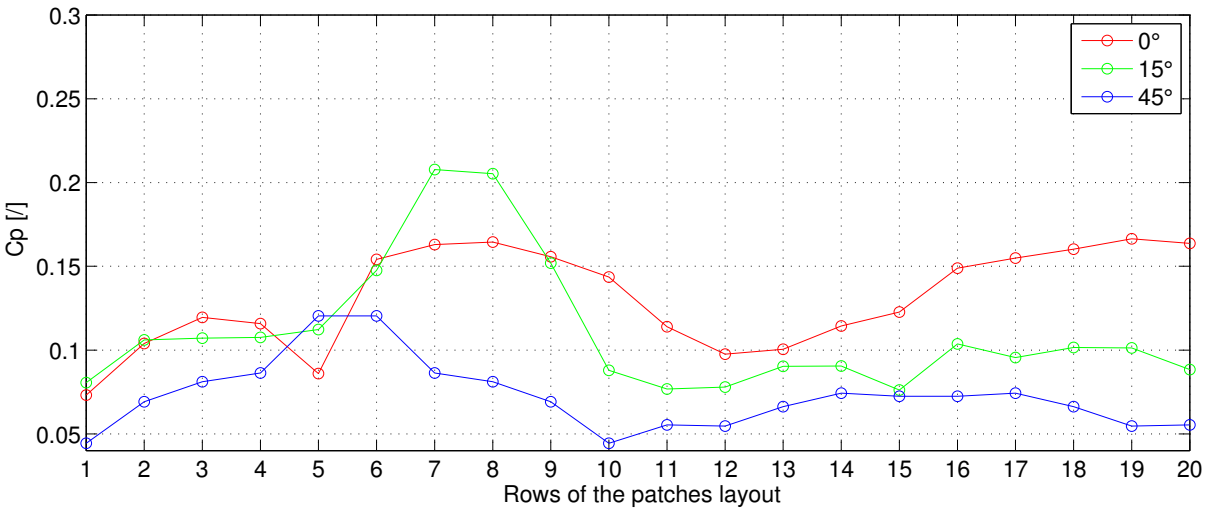

Figure 5.26 – Influence of the wind direction on the standard deviation C_P profile along the width of each facade

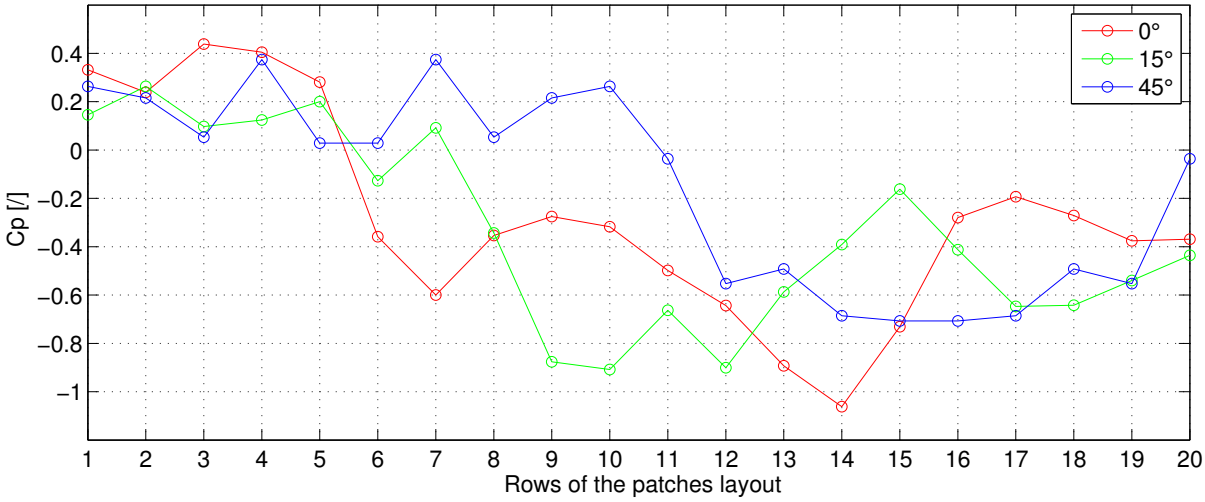

Figure 5.27 – Influence of the wind direction on the skewness C_P profile along the width of each facade

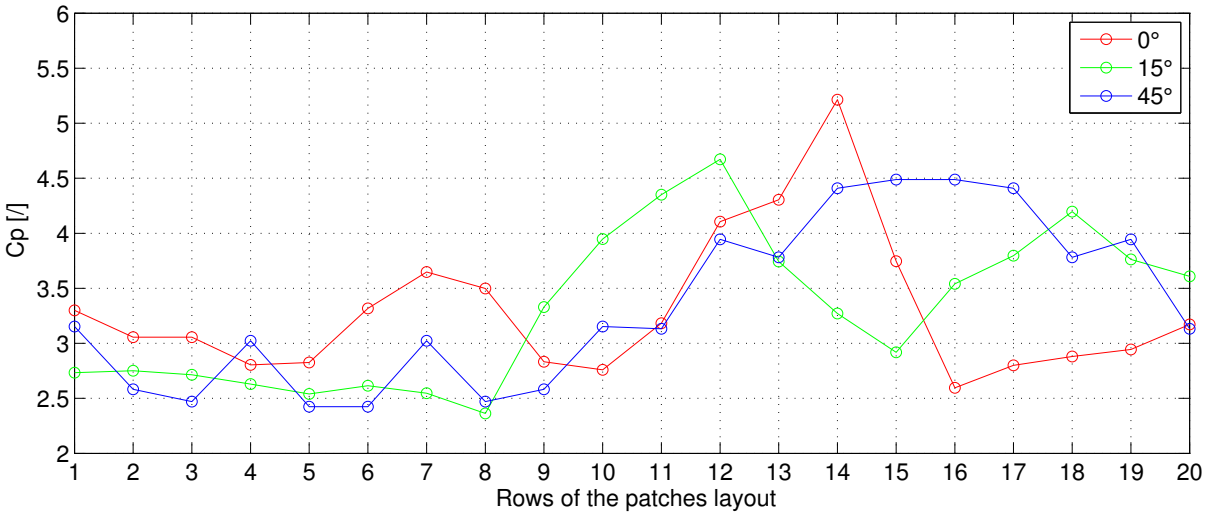

Figure 5.28 – Influence of the wind direction on the kurtosis C_P profile along the width of each facade

5.3 Conclusion

It is now important to summarize the major observations that have been presented in this chapter.

Along the height of the model, with a wind direction perpendicular to the windward facade, the pressure on each face increases in absolute value from the bottom to the top of the building. I also found lower negative pressure on the lateral sides than on the back frontage. Positive pressure only acts upon the front side because the flow separation occurs at the edges of this facade. I also noticed that interactions with the floor of the wind tunnel disturb the measurements in the first 8 m of the lateral facades. Then, pressure fluctuations appeared larger on the lateral faces than on the front and back sides. The skewness only happens to vary along the height of the front side whereas it stays constant on the three other faces. Finally, the kurtosis remains relatively constant and around the Gaussian value of 3 on the entire height of the building.

Regarding the front and back sides, I noticed that changing the wind direction to 15 degrees does not affect the pressure measurements. At 45 degrees the only effect is to decrease the mean pressure on the front side while everything stays unaffected on the back one. Angles of incidence of 15 and 45° place the left side into the wake and the pressure recorded on this side become very similar to those of the back face. The right side is highly affected by the wind direction and the profile of the third first statistical moments change considerably.

The frequency analysis revealed that the vortex shedding effect disappears on the right facade when the model is turned at 15 and 45 degrees whereas it remains visible on the left side.

The results of the patches layout confirmed the comments made about the vertical measurements. They also showed that the variations along the width of the model are highly specific to the facade tested, the statistical moment chosen and to the wind direction. The most important conclusions about the front side are the "C shaped" mean and standard deviation profiles, and the constant values along the width of the building for the skewness and kurtosis. The three other facades presented nearly constant mean values, flatter standard deviation profiles and generally higher skewness and kurtosis values at their windward edges. I also highlighted the fact that the four statistical moments change dimly along the height of each patch.

Finally, the patches and the vertical layout showed similar conclusions about the influence of the wind direction. However it appeared difficult to fit specific trends to the skewness and kurtosis profiles along the width of the building model.

Chapter 6

Statistical analysis

6.1 Influence of a non Gaussian wind flow on the pressure field

The analysis of the velocity measurements in chapter 3 have shown that, above a certain height, the wind flow generated in the wind tunnel of the University of Liège cannot be considered as a Gaussian process. Then, followed this question: "How does a non-Gaussian wind flow influence the pressure measurements recorded in an atmospheric boundary layer in wind tunnel"?

Chapter 5 partially answers the question by revealing that the pressure field on the lateral and back facades of a prismatic high rise building is clearly non-Gaussian and that this non-gaussianity finds its physical explanation in the combination between the wind process (wide band) and the vortex-shedding process (narrow band).

However, we still do not know the influence of the wind process on the non-gaussianity observed on the windward facade of the model.

The wind velocity is linked to the pressure field by a non linear relation containing a square operator. Therefore, predicting the statistical moments of the pressure field based on those of the wind flow is not straightforward. An intuitive way to solve this problem is to compute pressure coefficients on the basis of the velocity measurements.

$$C_{P,u}(h) = \frac{1/2\rho U(h)^2}{1/2\rho V_\infty^2} \tag{6.1}$$

The notation $C_{P,u}$ is used to denote the coefficients of pressure computed with the velocity data.

Another way to tackle the problem is to develop equations that would evaluate the statistical moments of a function of stochastic processes. Let's start with a Gaussian random variable u characterized by its probability density function:

$$p_u(u) = \frac{1}{\sqrt{2\pi}\sigma} e^{-\frac{(u-\mu)^2}{2\sigma^2}} \tag{6.2}$$

The first four statistical moments of this variable are:

$$\begin{aligned} m_0 &= 1 \\ m_1 &= \mu \\ m_2 &= \mu^2 + \sigma^2 \\ m_3 &= \mu^3 + 3\mu\sigma^2 \\ m_4 &= \mu^4 + 6\mu^2\sigma^2 + 3\sigma^4 \end{aligned} \tag{6.3}$$

The centered statistical moments are often preferred because of their easier interpretations. The centered and non centered statistical moments are linked by the following relations:

$$\begin{aligned} \tilde{m_1} &= 0 \\ \tilde{m_2} &= m_2 - m_1^2 \\ \tilde{m_3} &= m_3 - 3m_1m_2 + 2m_1^3 \\ \tilde{m_4} &= m_4 - 4m_1m_3 + 6m_1^2m_2 - 3m_1^4 \end{aligned} \tag{6.4}$$

In the case of a Gaussian variable the results are simply:

$$\begin{aligned} \tilde{m_1} &= 0 \\ \tilde{m_2} &= \sigma^2 \\ \tilde{m_3} &= 0 \\ \tilde{m_4} &= 3\sigma^4 \end{aligned} \tag{6.5}$$

By following the development proposed by [Denoël, 2005], we can consider a random process $p_u(u)$ that is defined as a function of the Gaussian process $u(t)$ like:

$$p_u(u) = \gamma(\bar{U} + u(t))^2 \tag{6.6}$$

This expression obviously represents the wind velocity $u(t)$ and the wind pressure $p_u(u)$. The idea is to develop equations that express the statistical moments of $p_u(u)$ as a function of the mean and standard deviation of $u(t)$.

The wind velocity signals recorded at a certain height in the wind tunnel only depends on the time and can be considered as a stationary ergodic process. In this case, the mathematical expectation can be realized over time. This means that their first order statistical moments do not vary in time and that the relations in 6.3, 6.4, and 6.5 stay valid for the first order characterization of $u(t)$.

By definition the first statistical moment of $p_u(u)$ can be computed as:

$$\begin{aligned} m_{1_p} &= E[\gamma(\bar{U} + u(t))^2] \\ m_{1_p} &= \gamma E[(\bar{U} + u(t))^2] \\ m_{1_p} &= \gamma(E[\bar{U}^2] + E[u(t)^2] + E[2\bar{U}u(t)]) \\ m_{1_p} &= \gamma(\bar{U}^2 + \sigma_u^2) \end{aligned} \tag{6.7}$$

The same method can be used to compute the other statistical moments. Table 6.1 presents the results for the first four statistical moments of the process $p_u(u)$.

Statistical moment	Expression
m_{1_p}	$\gamma(\bar{U}^2 + \sigma_u^2)$
m_{2_p}	$\gamma^2(\bar{U}^4 + 6\bar{U}^2\sigma_u^2 + 3\sigma_u^4)$
m_{3_p}	$\gamma^3(\bar{U}^6 + 15\bar{U}^4\sigma_u^2 + 45\bar{U}^2\sigma_u^4 + 15\sigma_u^6)$
m_{4_p}	$\gamma^3(\bar{U}^8 + 28\bar{U}^6\sigma_u^2 + 210\bar{U}^4\sigma_u^4 + 420\bar{U}^2\sigma_u^6 + 105\sigma_u^8)$

Table 6.1 – First four statistical moments of the random process $p(u) = \gamma(\bar{U} + u(t))^2$

Once again, we can use the relations in 6.4 to compute the centered statistical moments. Results are shown in Table 6.2.

Statistical moment	Expression
$\tilde{m}_{1_p}$	0
$\tilde{m}_{2_p}$	$2\gamma^2\sigma_u^2(2\bar{U}^2 + \sigma_u^2)$
$\tilde{m}_{3_p}$	$8\gamma^3\sigma_u^4(3\bar{U}^2 + \sigma_u^2)$
$\tilde{m}_{4_p}$	$12\gamma^4\sigma_u^4(4\bar{U}^4 + 20\sigma_u^2\bar{U}^2 + 4\sigma_u^4)$

Table 6.2 – First four statistical moments of the random process $p(u) = \gamma(\bar{U} + u(t))^2$

Recalling the definition of section 2.4, the skewness and the kurtosis of the process $p_u(u)$ become respectively:

$$\gamma_{3_p} = \frac{\tilde{m}_{3_p}}{\tilde{m}_{2_p}^{3/2}} = \frac{8\gamma^3\sigma_u^4(3\bar{U}^2 + \sigma_u^2)}{[2\gamma^2\sigma_u^2(2\bar{U}^2 + \sigma_u^2)]^{2/3}} \tag{6.8}$$

$$\gamma_{4_p} = \frac{\tilde{m}_{4_p}}{\tilde{m}_{2_p}^2} = \frac{12\gamma^4\sigma_u^4(4\bar{U}^4 + 20\sigma_u^2\bar{U}^2 + 4\sigma_u^4)}{[2\gamma^2\sigma_u^2(2\bar{U}^2 + \sigma_u^2)]^2} \tag{6.9}$$

These equations rely on the assumption that $u(t)$ is a Gaussian process. Therefore, if the wind flow inside the wind tunnel is perfectly Gaussian, the statistical moments of the experimental pressure field should tend toward the expressions that just have been presented.

Figure 6.1 to 6.4 compare the first four statistical moments of the pressure measurements to those computed with the velocity data and to the theoretical expressions. It appears obvious that only the pressure signals recorded on the windward facade are relevant for this comparison as the flow around the other facades is heavily influenced by the model itself.

The pressure measurements presented in this chapter were recorded with a wind flow perpendicular to the windward facade. Chapter 5 showed that the pressure field on the front side stays unchanged at 15 degrees and that only the mean and the standard deviation slightly change at 45 degrees. Therefore, studying the influence of the wind direction is not essential in this chapter.

Note that sometimes in chapter 5, I have referred to this section to explain the shape of different profiles. Despite the comparison is more relevant with the pressure recorded on the windward face at 0°, this section provides keys to understand some variations of statistical moments observed in the last chapter.

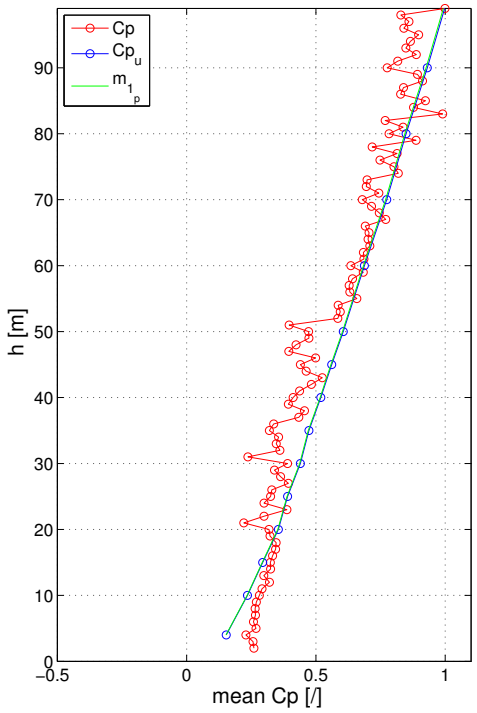

Figure 6.1 – Mean C_P profile on the front facade with a 0° incident wind compared to C_{P_u} computed with the velocity measurements and m_{1_p}

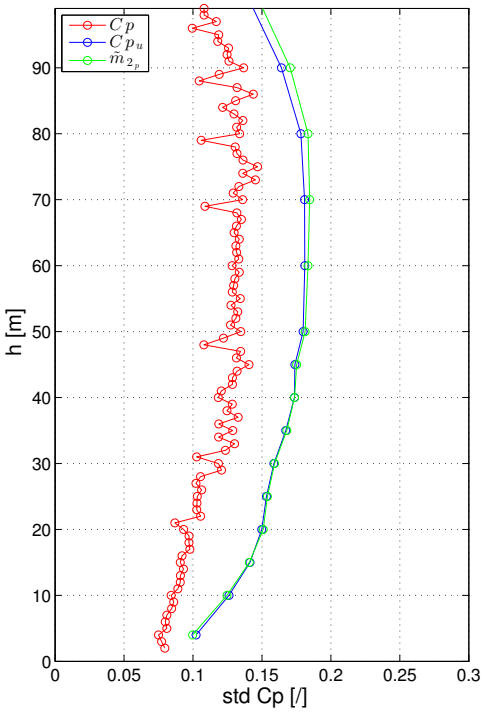

Figure 6.2 – Standard deviation profile on the front facade with a 0° incident wind compared to C_{P_u} computed with the velocity measurements and $\tilde{m_{2_p}}$

Figure 6.1 shows that the three mean pressure profiles are very similar. This results indicates that the wind pressure field on the windward facade is correctly predicted by the quasi-steady theory. We also see that the mean pressure increases almost linearly with the height. This is due to the velocity profile that increases in the same way. The small difference between the three profiles in the first 10 m is due to different positions of the wooden blocks used to create the atmospheric boundary layer (ABL1 and ABL2 see section 3.6).

The shape of the standard deviation profiles on figure 6.2 can be explained by looking at the second equation in table 6.2. This relation depends on the mean and standard deviation of the wind flow. On the one hand, we have seen on figure 3.2 that the wind speed increases quickly in the lower part of the ABL and then tends toward a constant free stream velocity. On the other hand, the wind fluctuations (figure 3.4) follow an inverted trend, with a slow decreasing part followed by a steeper negative slope. Hence, at low altitude, the standard deviation of the pressure measurements increases following the mean velocity profile squared. Higher in the ABL, the growth of the mean velocity is compensated by the decreasing of the wind fluctuations and the standard deviation profile stop increasing. Near the top of the model, σ_u decreases faster and $\bar{U}$ is nearly constant which explains the inflection to the left of the profile presented on figure 6.2. We can also observe that the experimental values are lower than those computed analytically and with the velocity data.

Note that both m_{1_p} and $\tilde{m}_{2_p}$ have been normalized with the value of m_{1_p} at the reference height in order to be compared with non-dimensional values.

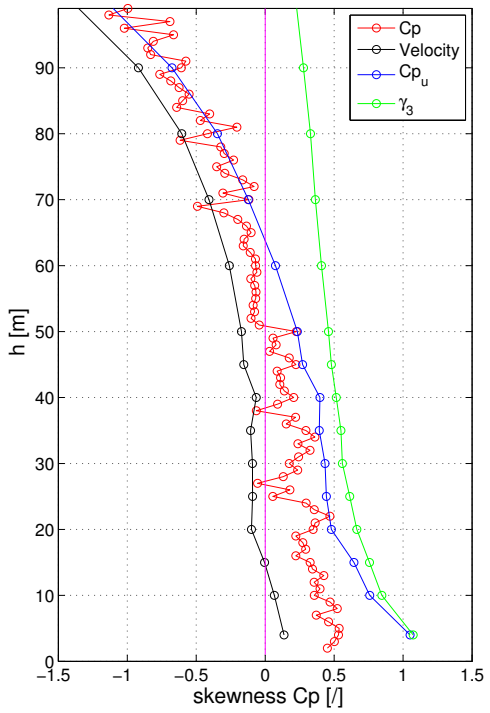

Figure 6.3 – Skewness C_P profile on the front facade with a 0° incident wind compared to the skewness of the velocity data, C_{P_u} and $\gamma 3_p$

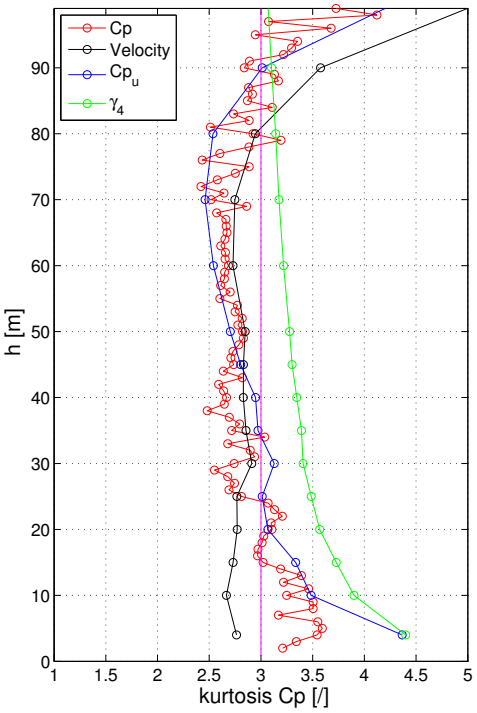

Figure 6.4 – Kurtosis C_P profile on the front facade with a 0° incident wind compared to the kurtosis of the velocity data, C_{P_u} and γ_{4_p}

We can now continue this comparison by focusing on the skewness coefficient as depicted on figure 6.3. To explain the shape of the green profile, I will once again refer to [Denoël, 2005] who demonstrated that the skewness of this type of random process can be approximated by $3I_u$.

$$\gamma_{3_p} = \frac{\tilde{m}_{3_p}}{\tilde{m}_{2_p}^{3/2}} = \frac{8\gamma^3\sigma_u^4(3\bar{U}^2+\sigma_u^2)}{[2\gamma^2\sigma_u^2(2\bar{U}^2+\sigma_u^2)]^{2/3}} = 3I_u\frac{1+I_u^2}{(1+I_u^2)3/2} \simeq 3I_u \tag{6.10}$$

This can also be understood intuitively. At low altitude, the fluctuations of the wind velocity are large compared to the mean value. The square operator that links velocity and pressure amplifies more the gap between the mean and high values compared to the the one between the mean and small values. It follows that the statistical distributions of the pressure measurements are skewed toward the high positive values. Higher in the boundary layer, the ratio $\bar{U}/\sigma_u$ increases and the influence of the fluctuation weakens compared to the the mean. The distributions are therefore less skewed and tend to be Gaussian.

The black line on the figure 6.3 represents the skewness profile of the velocity measurements. By comparing it to the pressure profile we observe that, in the upper half of the model where the velocity data are non-Gaussian, the pressure measurements are also non-Gaussian. This constitutes a first answer to the question asked at the beginning of this chapter. We also notice that, compared to the velocity data, the pressure profile appears shifted to the left. This shift is well estimated by the blue profile and can be explained by the effect of the square operator on the statistical distribution.

Finally, the analytic equation 6.8 happens to overestimate the skewness of the front side pressure. In the Gaussian flow region (0 to 50 m), this expression can be viewed as a higher bound estimation of the pressure skewness coefficient. For altitude higher than 50 m, the non-gaussianity in the wind flow influences the pressure measurements and the analytic expression becomes non relevant.

The different profiles can also be compared on the basis of their kurtosis coefficients. Figure 6.4 confirms the comments made about the skewness. First, the front side pressure shows non-Gaussian values in the non-Gaussian flow region. Then the quasi-steady model represented by the blue profile estimates accurately the kurtosis of the pressure measurements. According to [N. Blaise and Denoël, 2014], equation 6.9 can be approximated by $12I_u^2$ which explains why the analytic kurtosis profile decreases faster to the Gaussian value than the skewness.

6.2 Coherence of the pressure field

Before going further into the statistical analysis of the pressure measurement, we first need to analyze the coherence that exists between the pressure signals recorded on the building model. The concept of coherence Γ_{xy} has been introduced in section 2.4 and characterizes the correlation between two stochastic processes x and y. In this thesis, x and y represent two pressure signals recorded at two different locations. In wind engineering, this function is often modeled by the following expression:

$$\Gamma_{xy} = e^{-\frac{Cn\Delta z}{\bar{U}}} \tag{6.11}$$

Where C is a decay constant that determines the spacial extend of the correlation. n is the frequency in [Hz] and $\bar{U}$ is the wind velocity at the reference height. This function decreases both with the frequency and with the distance between the measurement taps.

Figure 6.5 represents the coherence functions Γ_{xy} between the pressure tap located at a height of 50 m on the vertical layout (called reference tap) and other taps located respectively at 2, 4, 6, 8, and 10 m underneath it. Each graphs corresponds to a facade of the model and Γ_{xy} is plotted as a function of a non-dimensional frequency $\Delta zn/U$. The five profiles, represented by different colors, are compared to the theoretical expression 6.11. The decay constant C has been fitted on experimental data using the least squares method.

Facade	Decay constant C
Front side	$\simeq 0.40$
Left side	$\simeq 0.25$
Back side	$\simeq 0.40$
Right side	$\simeq 0.25$

Table 6.3 – Decay constant values for each facade fitted on experimental data

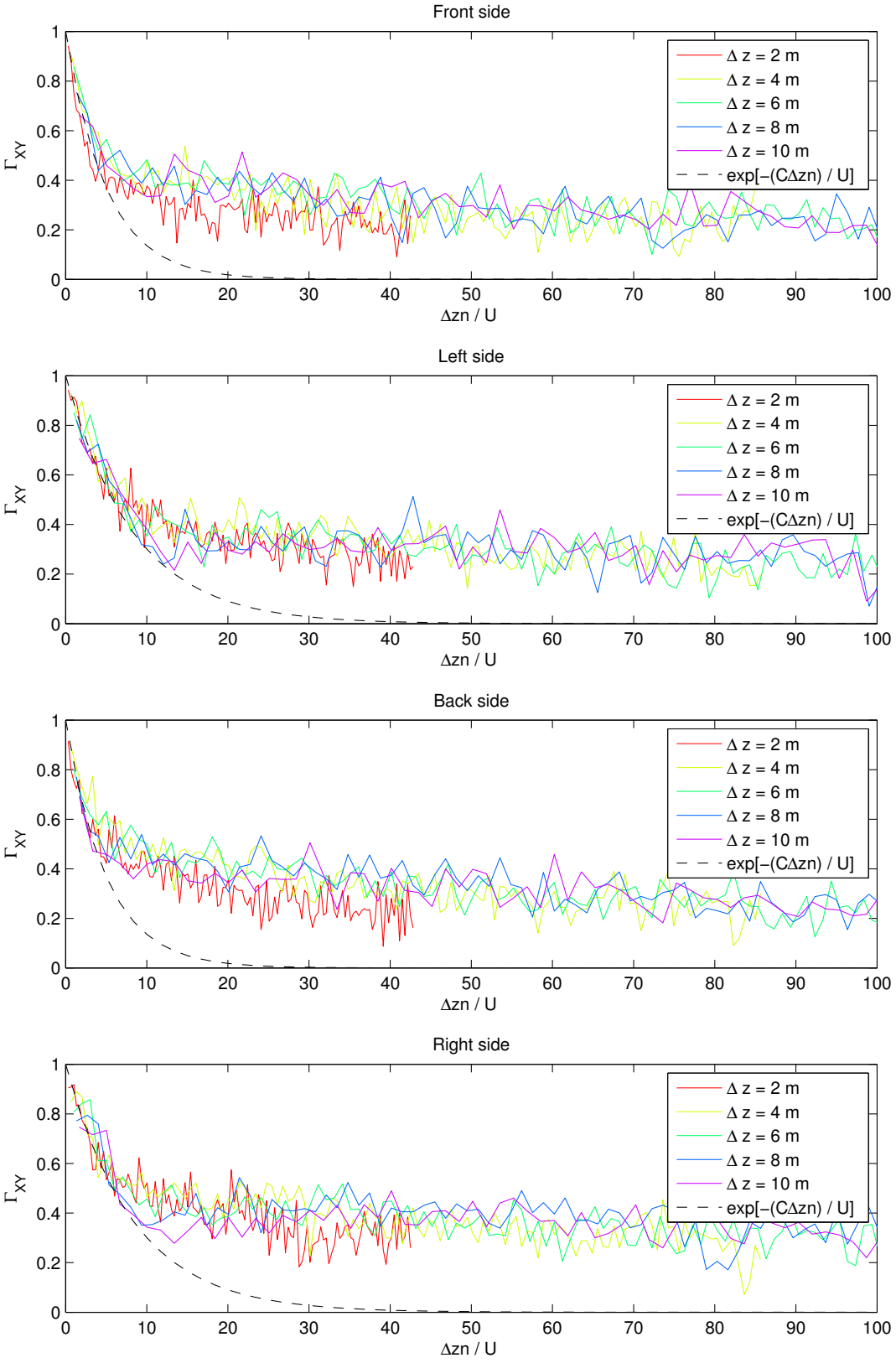

Figure 6.5 – Coherence between the pressure recorded at a height of 50 m and neighboring taps separeted by different distances and compared with the exponential model

Each profile on figure 6.5 shows the same bi-linear shape with a steep negative slope in the low frequencies followed by a flatter one. The coherence on the windward and leeward facade behave similarly. The same comment can be made about the lateral faces. The theoretical model happens to be a fair estimation of the coherence when considering its variation with the frequency. The fact that the model underestimates the coherence function at high frequencies is not really important. Indeed, when the model diverges from the experimental data, the coherence has already fallen to a small value which states that the two random process are weakly correlated.

The values obtained for the decay constant may seem too small compared to the values generally seen that oscillated between 6 and 12, for the coherence of the wind fluctuations. However, those values are related to real scale atmospheric boundary layers and I have shown in section 3.3 that the turbulence integral scale modeled inside the wind tunnel is far smaller than expected at real scale. Moreover, it is also known that the pressure field is better correlated than the wind flow. According to [Larose, 2002] correlation lengths of pressure can easily be 4 times larger than the correlation length of the incident wind.

The fact that each profile has the same shape means that the coherence only depends on the frequency and the distance Δz between the measurement taps. This can be easily proven by computing the coherence function as a function of Δz for different reference tap locations between 20 m and 90 m, as depicted on figure 6.6. The coherence decreases in the same way along the height of the model on each facade. This proves that the coherence function does not depend on the reference tap location along the height of the model. The deviation of the red line on the lateral sides is due to wind flow interactions with the floor of the wind tunnel. This has already been highlighted in chapter 5.

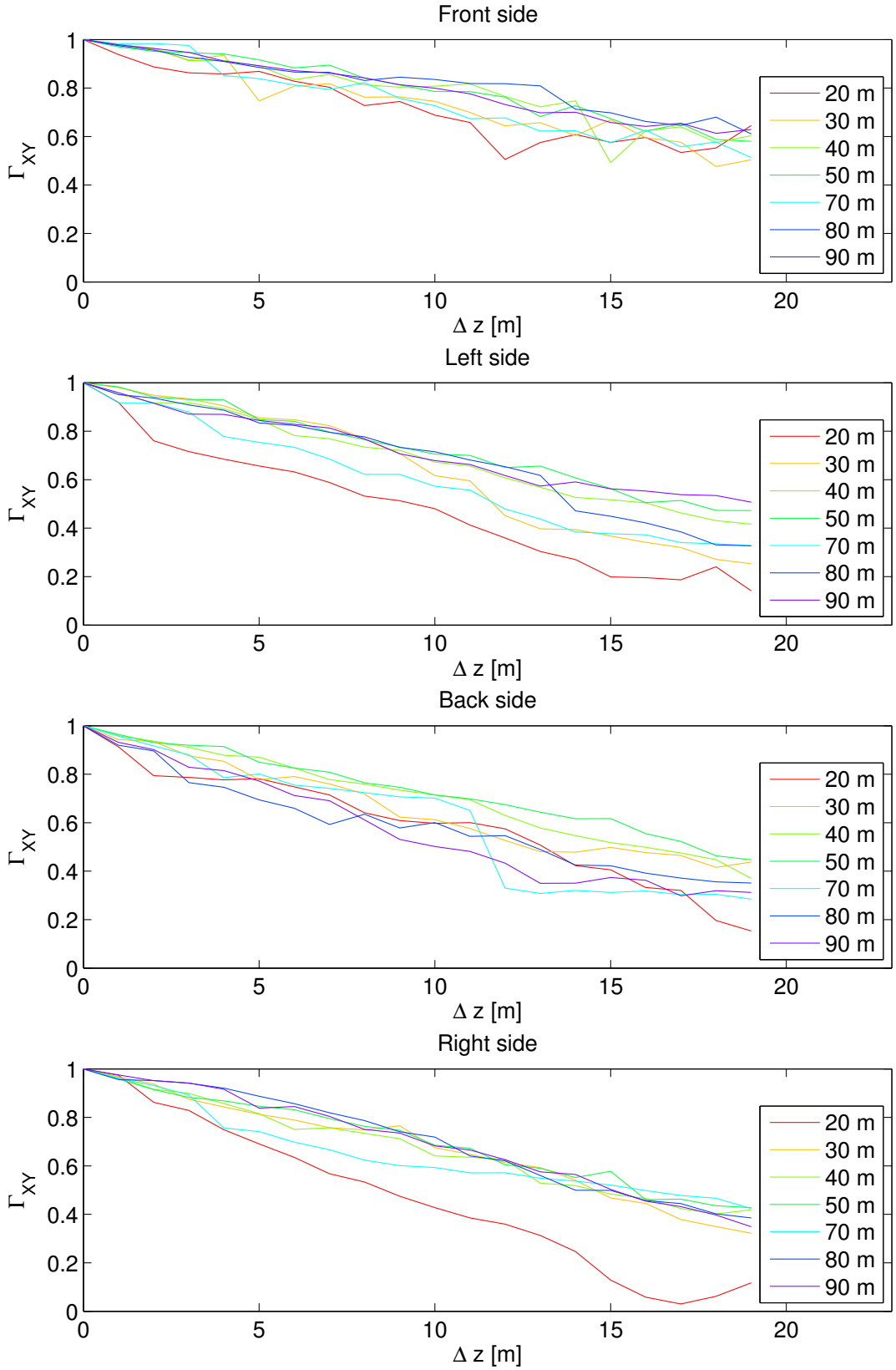

Figure 6.6 – Influence of the recording location on the coherence between pressure signals

We can now focus on the variation of the coherence with the distance that separates two pressure measurements. Figure 6.7 represents the coherence function computed between a reference tap located at a height of 50 m and all its neighbors along the height of the model. We can directly see that the coherence decreases linearly with Δz and that the profiles appear symmetrical with respect to the reference tap location. A linear model can be fitted on the experimental data (red lines on the graphs).

$$\Gamma_{xy} = \frac{0.8}{L_p^z}\Delta z + 1 \tag{6.12}$$

The coefficient L_p^z is the correlation length along the height of the model (z axis). It is generally admitted that two random processes are considered non-correlated when the coherence function takes values lower than 0.2. The correlation length is defined in this thesis as the distance required to have a coherence function equal to 0.2. This explains the 0.8 in equation 6.12. The correlation length have been estimated using the least square method on each facade.

Facade	Pressure correlation length (z axis)
Front side	$\simeq$ 40 m
Left side	$\simeq$ 27 m
Back side	$\simeq$ 27 m
Right side	$\simeq$ 27 m

Table 6.4 – Pressure correlation length (z axis) on each facade estimated with experimental data

The 40 meters indicated in table 6.4 suggest that the longitudinal length scale of turbulence of the wind flow is a good approximation for the vertical correlation length of the pressure field on the windward facade. On the lateral and leeward faces, the correlation length appears shorter and approximately equal to 2/3 of the length scale of turbulence.

The exponential model of equation 6.11 can also be used to approach the coherence function of the pressure measurements (black dashed line on the graphs). The decay constant adjusted to fit the experimental data are presented in table 6.5.

Facade	Decay constant C
Front side	$\simeq$ 0.45
Left side	$\simeq$ 0.55
Back side	$\simeq$ 0.55
Right side	$\simeq$ 0.55

Table 6.5 – Decay constant values for each facade fitted on experimental data

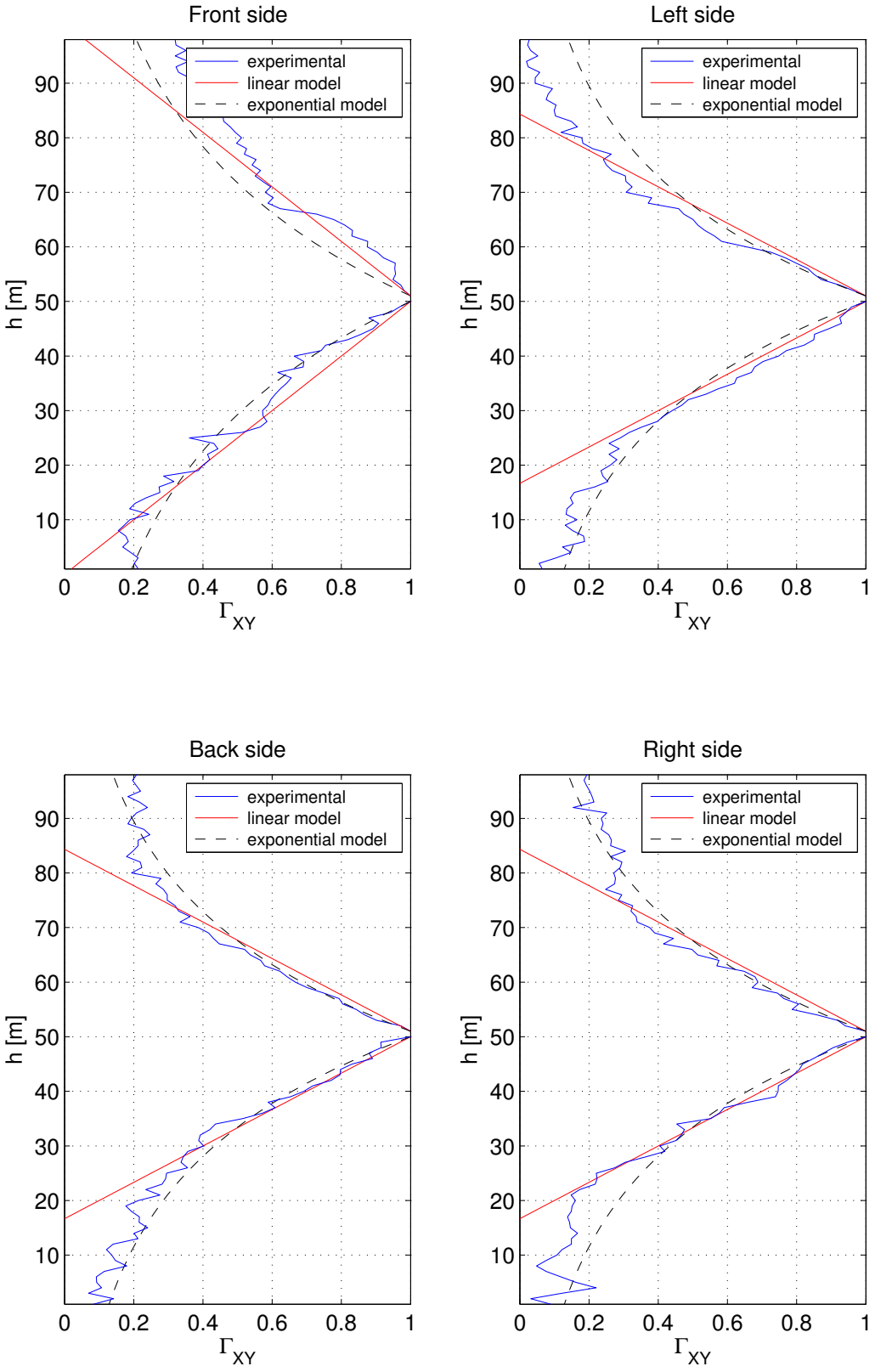

Figure 6.7 – Coherence function of the pressure recorded at a height of 50 m with neighboring taps along the height of the model and compared to a linear and exponential model

The patches layout provides information about the variation of the coherence function in two dimensions. Figures 6.10 to 6.11 present the coherence functions computed between different reference taps and all the other taps on a single patch. The considered reference tap locations are:

- The four corners of the patch.
- The center of the two peripheral rows.
- The center of the two peripheral lines.
- The center of the patches layout.

These location correspond to taps 1, 3, 5, 26, 28, 30, 46, 48 and 50 on figure 4.6). The nine graphs are presented in the same order on the following figures. As the coherence function only varies with the distance between pressure measurements, only the results from the lowest patch are presented.

The shape of the coherence functions does not appears perfectly circular. This indicates that the correlation length is not the same along the height (z axis) and along the width of the model (y axis). We can estimate the y-axis correlation lengths in the same way than we did for the vertical ones. Table 6.6 summarizes the estimations for each facade and each direction.

Facade	Pressure correlation length (z axis)	Pressure correlation length (y axis)
Front side	$\simeq$ 40 m	$\simeq$ 20 m
Left side	$\simeq$ 27 m	$\simeq$ 13 m
Back side	$\simeq$ 27 m	$\simeq$ 10 m
Right side	$\simeq$ 27 m	$\simeq$ 10 m

Table 6.6 – Pressure correlation length (z and y axis) on each facade estimated with experimental data

These results show that the pressure field is better correlated along the height of the model than along its width. The y-axis correlation lengths on the front and back sides drop by a factor 2 compared to the vertical estimations. Nearly a factor 3 can be observed between the two correlation lengths on the lateral facades.

On the front and back facades, we can notice that the contour lines are roughly equally spaced. This means that the correlation varies linearly in both directions. We also observe that each graph has the same shape and is just moved in different positions, which proves that the correlation function does not depends on the position of the reference tap in both directions.

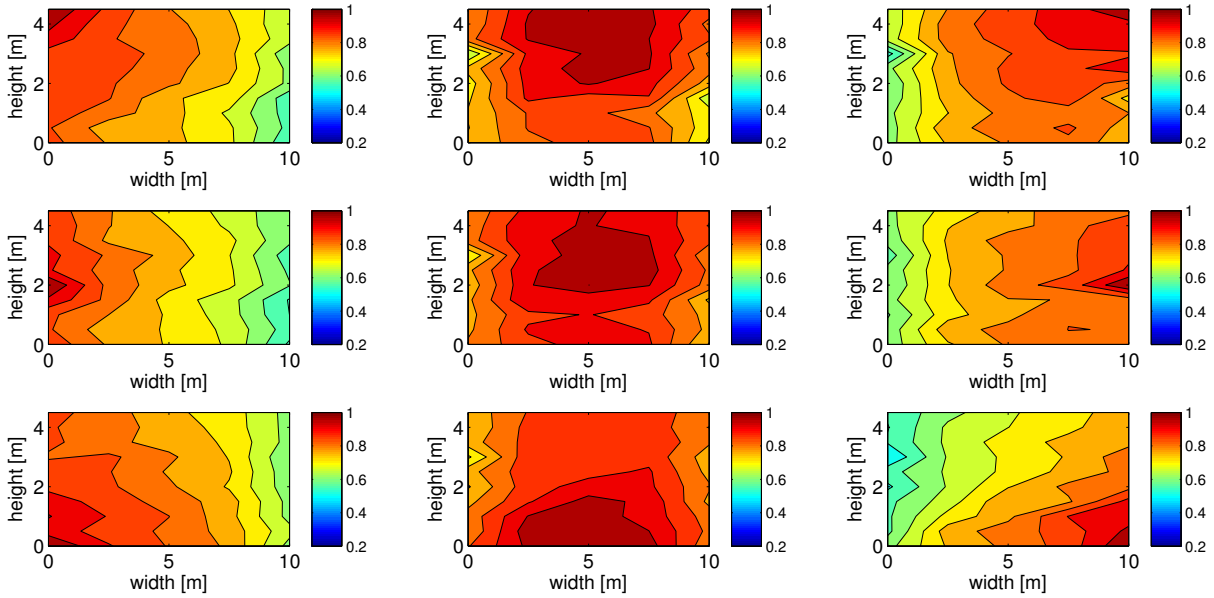

Figure 6.8 – Front side coherence function computed with the patches layout measurements between reference taps 1, 3, 5, 26, 28, 30, 46, 48, 50 and neighboring taps

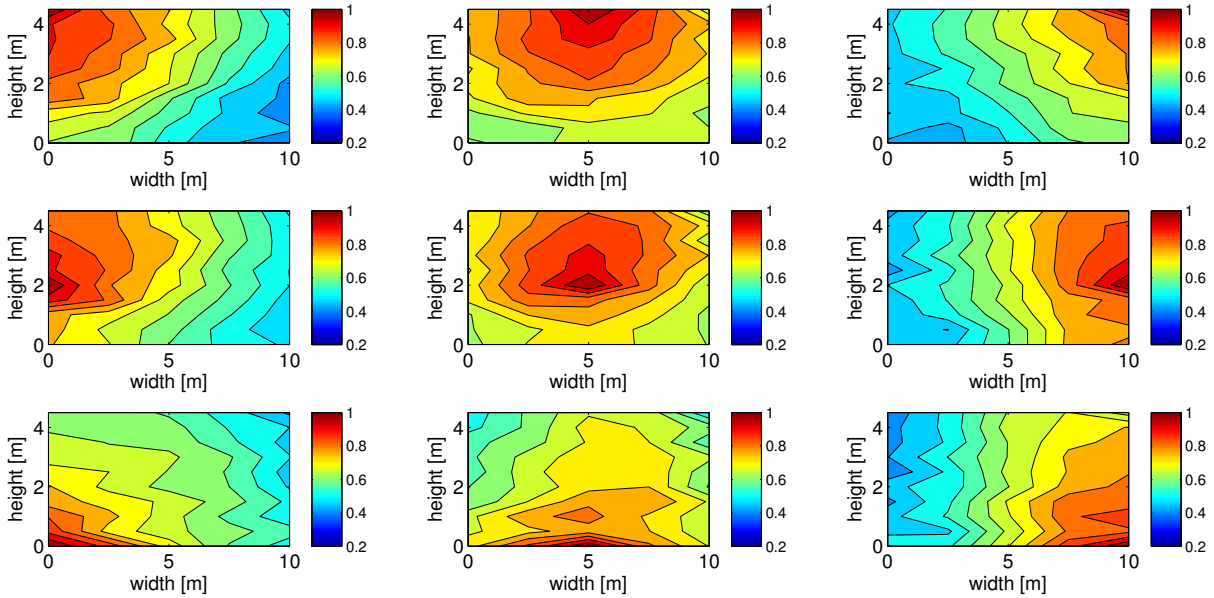

Figure 6.9 – Back side coherence function computed with the patches layout measurements between reference taps 1, 3, 5, 26, 28, 30, 46, 48, 50 and neighboring taps

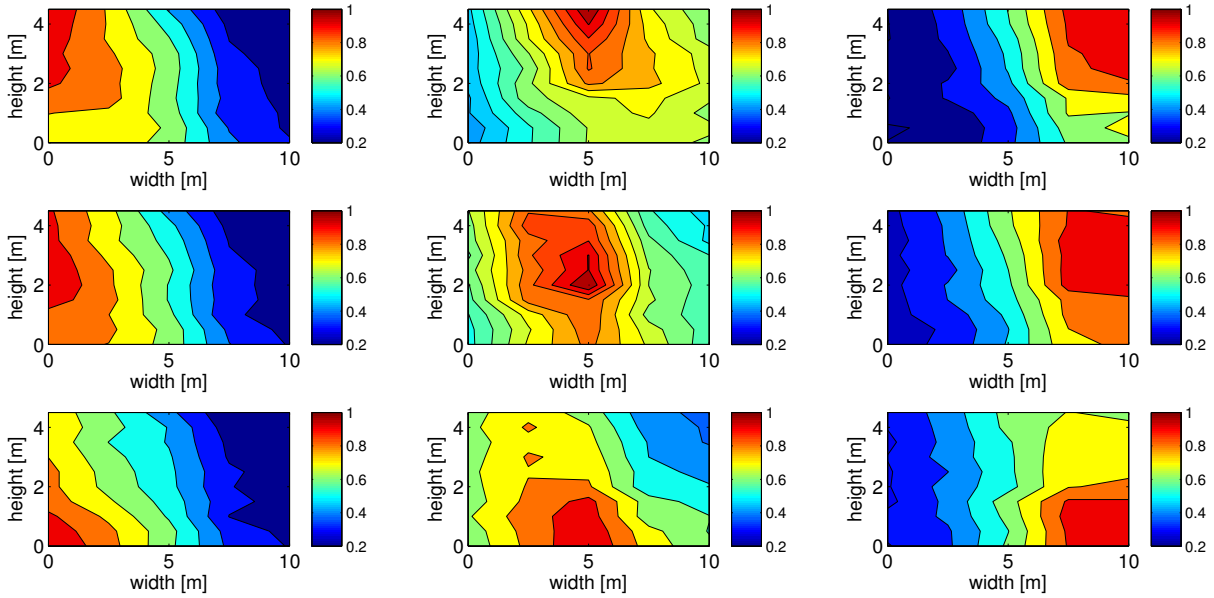

Figure 6.10 – Left side coherence function computed with the patches layout measurements between reference taps 1, 3, 5, 26, 28, 30, 46, 48, 50 and neighboring taps

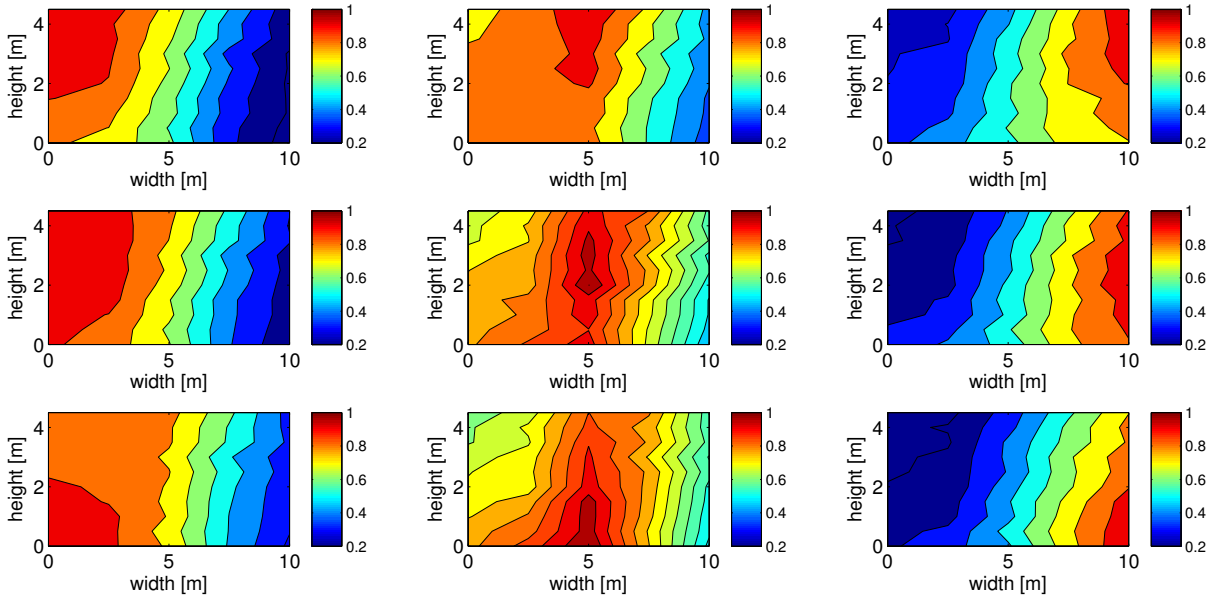

Figure 6.11 – Right side coherence function computed with the patches layout measurements between reference taps 1, 3, 5, 26, 28, 30, 46, 48, 50 and neighboring taps

On the lateral facades, the graphs do not have the same shape anymore and the coherence function clearly varies with the position of the reference tap along the width of the model. The pressure signals appear better correlated near the windward edges (right side of the graphs on figure 6.10 and left side of the graphs on figure 6.11). Away from this plateau, the contour lines are equally spaced indicating a linear variation of the coherence function.

6.3 Influence of the scale effect on the stochastic nature of the resultant force

As stated before, the objective of the experimenter is to generate a Gaussian wind flow inside the wind tunnel in order to be consistent with Codes and general practice. Section 6.1 has demonstrated that, in the region where the wind flow is non-Gaussian, the windward pressure field is also non-Gaussian. Therefore, we can conclude that building model higher than 50 cm (at model scale) cannot be tested inside the wind tunnel of the University of Liège. In fact, this limit is too restrictive because it does not take the size effect into consideration.

When the characteristic length of the structure is far smaller than the turbulence integral length of the wind flow, pressure peaks acting on the structure surface can be considered perfectly correlated. This means that the characteristic wind force can be computed by multiplying the characteristic pressure by the area exposed to the wind.

$$F_{max}(t) = C.P_{max}(t).A_{ref} \tag{6.13}$$

In this case, if the pressure field is non-Gaussian, the resultant force is also non-Gaussian.

For real structure having a windward surface larger than the order of magnitude of the integral scale of turbulence. The pressure peaks do not occur at the same moment on the entire surface of the structure and are partially correlated. According to the central limit theorem [Hilhorst, 2009], the probability density function of a sum of independent random variables can be approximated by a Gaussian distribution, if the sample size is sufficiently large and regardless of their own distributions. This theorem stays valid for partially correlated processes. This means that if we consider a sufficiently large area, the resultant wind force should tend toward a Gaussian distribution. Then, the following question arise: "What is a sufficiently large area"? It seems obvious that the resultant force at the bottom of a high rise building can be modeled as a Gaussian process. However, the answer to this question takes on its full meaning regarding the design of cladding and building elements.

The resultant wind force on a surface Ω is defined as:

$$R(t) = \iint_{\Omega} P(y, z, t) dy dz \tag{6.14}$$

I considered different surfaces Ω with increasing areas using the patches layout. Let's make the assumption that each pressure tap contributes to a unit area $A_0 = 0.5 \times 2m = 1m^2$ and that the pressure are perfectly correlated on this surface. The refined mesh of the patches layout and the evaluation of the correlation lengths ensure that the error introduced by the discretization of the pressure field stays limited. Equation 6.14 becomes:

$$R(t) = \sum_{i}^{n} Pi(y, z, t) A_0 dydz \tag{6.15}$$

The different surfaces Ω are rectangles of increasing areas starting at the top left corner of the patches layout as depicted on figure 6.12 (the dots represent the measurement taps of the layout and the dashed lines the limits of each unit area).

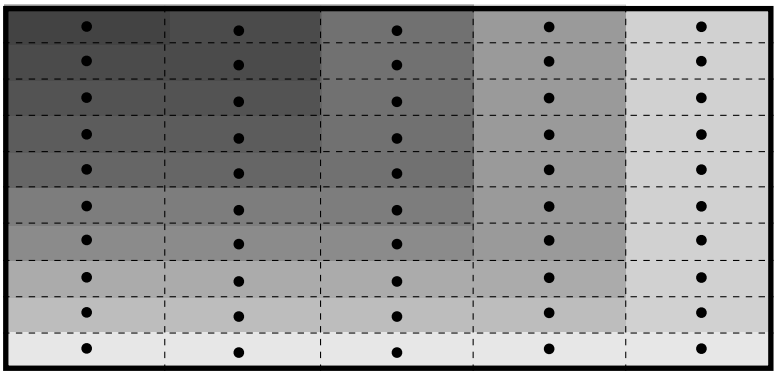

Figure 6.12 – Considered surfaces for the study of the size effect influence on the resultant force

Figure 6.13 represents the statistical moments of the resultant forces on the right facade as a function of a non-dimensional area $\Omega/L_U^x b$. The mean μ_F and the standard deviation σ_F are normalized with μ_{max_F} which is the resultant mean force acting on the largest surface considered.

The mean force on figure 6.13 increase linearly in magnitude with the surface. Indeed, by taking the definition of the mean and considering that each unit area is the same we can write:

$$\begin{aligned} E[R(t)] &= E[\sum_{i}^{n} Pi(y, z, t) A_0 dydz] \\ E[R(t)] &= E[nA_0 \sum_{i}^{n} Pi(y, z, t) dydz] \\ E[R(t)] &= nA_0 \sum_{i}^{n} E[Pi(y, z, t)] dydz \end{aligned}$$

Knowing that the pressure does not vary along the height of the patch and neglecting the variation along the width, we can estimates $P_i(x, y, t)$ by $P_0(t)$ and we obtain:

$$\begin{aligned} E[R(t)] &= nA_0 E[P_0(t)] \\ E[R(t)] &= nA_0 \mu_P \end{aligned} \tag{6.16}$$

Which is the equation of a straight line.

The standard deviation increases like two straight lines with a steeper slope in the first half of the profile. This can once again be explained mathematically. The definition of the variance of the resultant force is:

$$E[(R(t)-\mu_R)^2] = E[\iiiint_{\Omega}(P_1(y,z,t)-\mu_{P_1})^2(P_2(y,z,t)-\mu_{P_2})^2 dy_1 dz_1 dy_2 dz_2]$$
$$E[(R(t)-\mu_R)^2] = \iiiint_{\Omega} E[(P_1(y,z,t)-\mu_{P_1})^2(P_2(y,z,t)-\mu_{P_2})^2] dy_1 dz_1 dy_2 dz_2$$

The expression in the integral is the covariance function between $P_1(t)$ and $P_2(t)$ which is equal to the correlation function multiplied by the standard deviation of each process (see definition 2.30)

$$E[(R(t)-\mu_R)^2] = \iiiint_{\Omega} \rho_{P_1,P_2}(y,z)\sigma_{P_1}\sigma_{P_2} dy_1 dz_1 dy_2 dz_2$$
$$E[(R(t)-\mu_R)^2] = \sigma_{P_1}\sigma_{P_2} \iiiint_{\Omega} \rho_{P_1,P_2}(y,z) dy_1 dz_1 dy_2 dz_2$$

This equation can be rewritten as:

$$E[(R(t)-\mu_R)^2] = \sigma_{P_1}\sigma_{P_2}\Omega^2 \left[\frac{1}{\Omega^2}\iiiint_{\Omega} \rho_{P_1,P_2}(y,z) dy_1 dz_1 dy_2 dz_2\right]$$

The expression inside brackets is the squared admittance function χ^2 which accounts for the imperfect correlation between pressure peaks that act on the surface. This function take its values between 0 and 1

$$E[(R(t)-\mu_R)^2] = (\sigma_{P_1}\sigma_{P_2}\Omega)^2\chi^2 \tag{6.17}$$

When the surface area is small the correlation between the pressure peaks is nearly perfect and the admittance function is close to 1. In this case, the standard deviation increases linearly with the surface. When the surface is larger, the pressure are less correlated and the admittance function decreases. Thus, the slope of the standard deviation profile decreases as well. In fact, adding highly correlated signals results in adding the peak values which induces large standard deviation. When the peaks do not occur at the same moment, they are added to lower values and the standard deviation increases less.

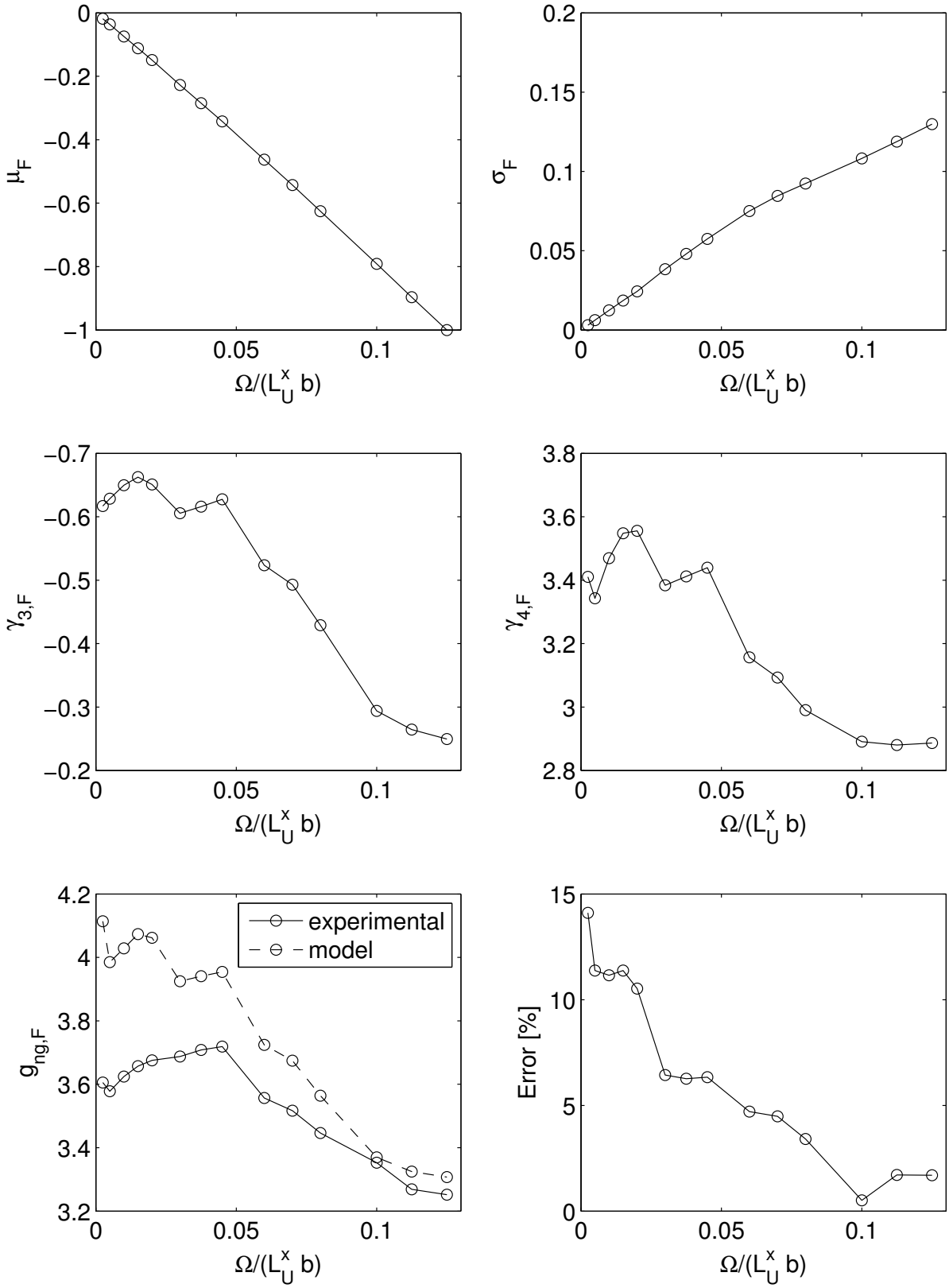

Figure 6.13 – Influence of the scale effect on the statistical moments and on the peak factor of the resultant force (Right facade)

The skewness and the kurtosis of the resultant force on figure 6.13 stay constant and then decrease exponentially to reach Gaussian values. In fact three effects influence the progressive reduction of the non-gaussianity of the resultant force signal as larger areas are considered:

- **The central limits theorem** insures that the distribution of the resultant force tends to be Gaussian as an increasing number of pressure signals are added together, independently of their individual distributions.
- **The variation of the skewness and kurtosis along the width of the model** influences also the gaussinity of the resultant force. We have seen in chapter 5 that pressures are highly non-Gaussian near the windward edges of the lateral facades and tend to be Gaussian near the tailing edges of these faces. Note that if I had chosen to increase the surface area from the right corner of the patch instead of the left one, both effect would have canceled each other. In this case, the resultant force would have appeared Gaussian regardless of the surface area.
- **The coherence between pressure measurements** influences the convergence of the central limits theorem. The more the pressure signals are correlated, the larger the surface must be. We have seen that the pressure signals are better correlated near the windward edges where the pressure are non-Gaussian. This explains the plateau observed on the skewness and kurtosis profiles.

We also see that the kurtosis coefficient decreases faster than the skewness. These results are in line with the analytic developments realized by [N. Blaise and Denoël, 2014].

The peak factor of the resultant force is also presented on figure 6.13. It can be computed with the experimental data by first centering and normalizing the resultant force signals:

$$R(t) = \frac{R(t) - \mu_R}{\sigma_R} \tag{6.18}$$

Then the signals are cut into parts having a duration of 10 minutes at full scale each. Finally the peak factor is computed by taking the average of the largest value in each sub-signal.

The peak factors computed with this method are compared to the values obtained with the expression presented in [Gurley et al., 1997] which derives from on a moment based Hermite transformation and that accounts for the non-Gaussian properties of the process.

$$g_{ng} = \kappa \left\{ \left(\beta + \frac{\gamma}{\beta} \right) + h_3(\beta^2 + 2\lambda - 1) + h_4 \left[\beta^3 + 3\beta(\gamma - 1) + \frac{3}{\beta} \left(\frac{\pi^2}{12} - \gamma + \frac{\gamma^2}{2} \right) \right] \right\} \tag{6.19}$$

With $\gamma = 0.5772$ (Euler's constant), $\beta = \sqrt{2ln(\nu_0 T)}$, ν_0 is the zero upcrossing rate and considering the following expressions:

$$h_3 = \frac{\gamma_3}{4 + 2\sqrt{1 + 1.5\gamma_4}} \tag{6.20}$$

$$h_4 = \frac{\sqrt{1 + 1.5\gamma_4} - 1}{18} \tag{6.21}$$

$$\kappa = \frac{1}{\sqrt{1 + 2h_3^2 + 6h_4^2}} \tag{6.22}$$

We can see that it highly depends on the kurtosis and skewness coefficient. For small areas, the peak factors computed with both methods are higher than 3.5 as assumed in the Eurocode 1-4. The model also happen to overestimate the peak factor compared to the experimental data. The difference is larger when the process is non-Gaussian as depicted on the last graph.

Finally, we notice that the transition between the non-Gaussian and the Gaussian distribution of the resultant force occurs between $\Omega/L_U^x b = 0.05$ and $\Omega/L_U^x b = 0.1$. Thus, between $\Omega = 20cm^2$ and $\Omega = 40cm^2$ at model scale. We can conclude that, on lateral facades, the resultant force acting on a surface having an area larger than $\Omega/L_U^x b = 0.75$ can be considered as a Gaussian process. This surface corresponds to $\Omega = 30m^2$ in full scale and $\Omega = 30cm^2$ at model scale. I considered that the minimum skewness value to characterize a process as non-Gaussian is 0.5 in absolute value and 3.5 for the kurtosis.

The same conclusions can be drawn concerning the back facade. Results are presented on figure 6.14.

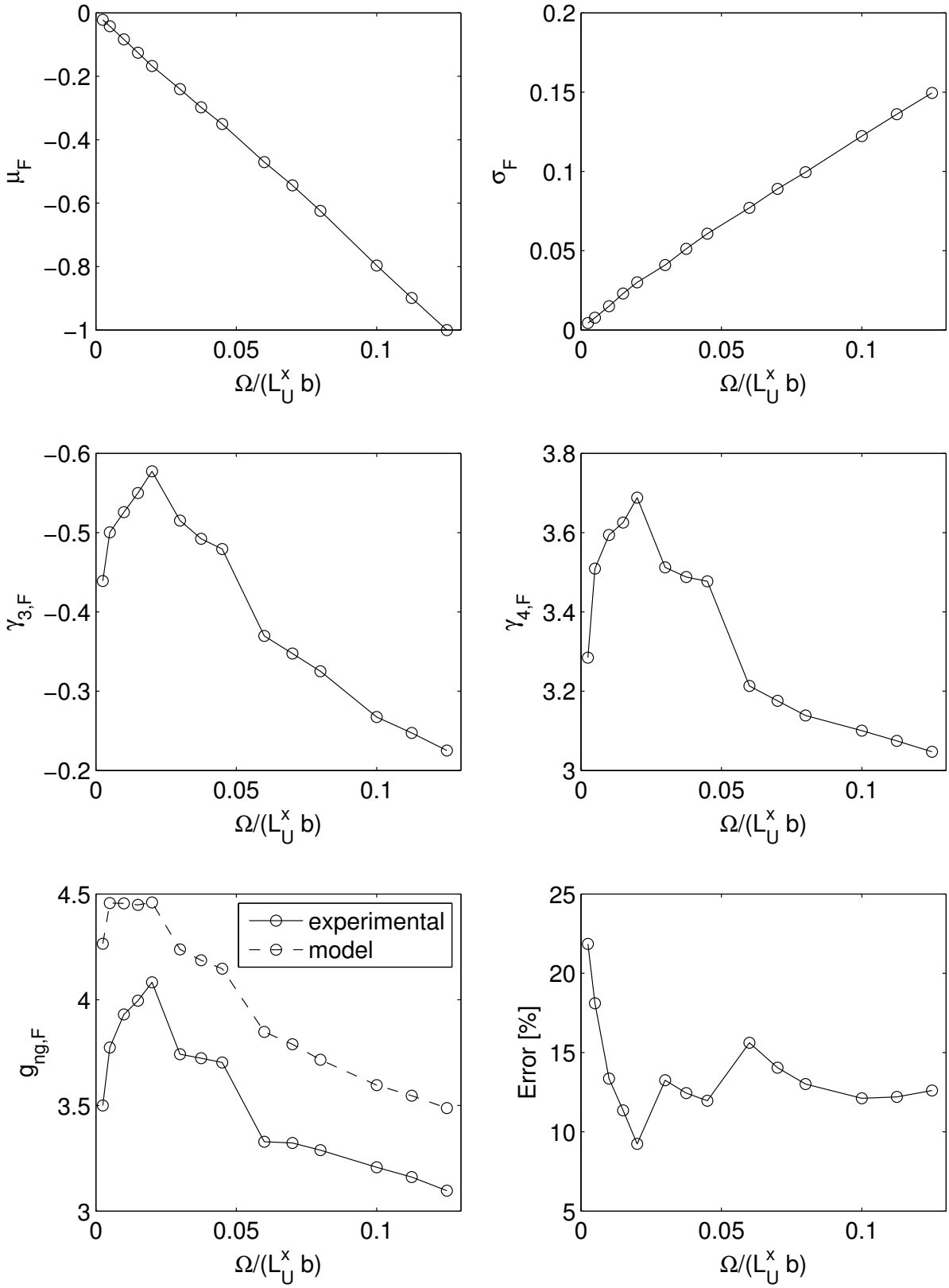

Figure 6.14 – Influence of the scale effect on the statistical moments and on the peak factor of the resultant force (Back facade)

Figure 6.15 represents the statistical moments of the resultant forces on the front side as a function of the non-dimensional area. For this facade, the surface of the patches layout was too small to reach Gaussian values. Therefore, I used the vertical layout and considered surfaces starting at the top of the model and increasing toward the ground. A unit area of $A_0 = 1 \times 2 = 2m^2$ was chosen.

In this case, the distribution of the resultant force can only be considered Gaussian when the surface area is larger than $\Omega/L_U^x b = 0.2$ compared to 0.075 for the other building faces. This is due to the correlation length on the front side that is larger than on the other faces and to the larger skewness values.

However, another comment needs to be made about the results generated for the front side. With the vertical layout, the only way to increase the surface area is vertically. Then, we have seen that the correlation length is longer in this direction than along the width of the model. So it is possible that the result of $\Omega/L_U^x b = 0.2$ is slightly overestimated due to the computation technique.

We also see that the size effect influences the mean forces when large areas are considered. The assumption of nearly equal mean pressure values made in equation 6.16 is no more applicable.

The small peak factor observed on this facade is due to the skewness coefficient that is negative. The statistical distribution are skewed toward the low force values. We also notice relatively large deviation between the model and the experimental data.

The results developed in this section are in line with the analytic developments realized by [N. Blaise and Denoël, 2014] and [Carassale, 2012].

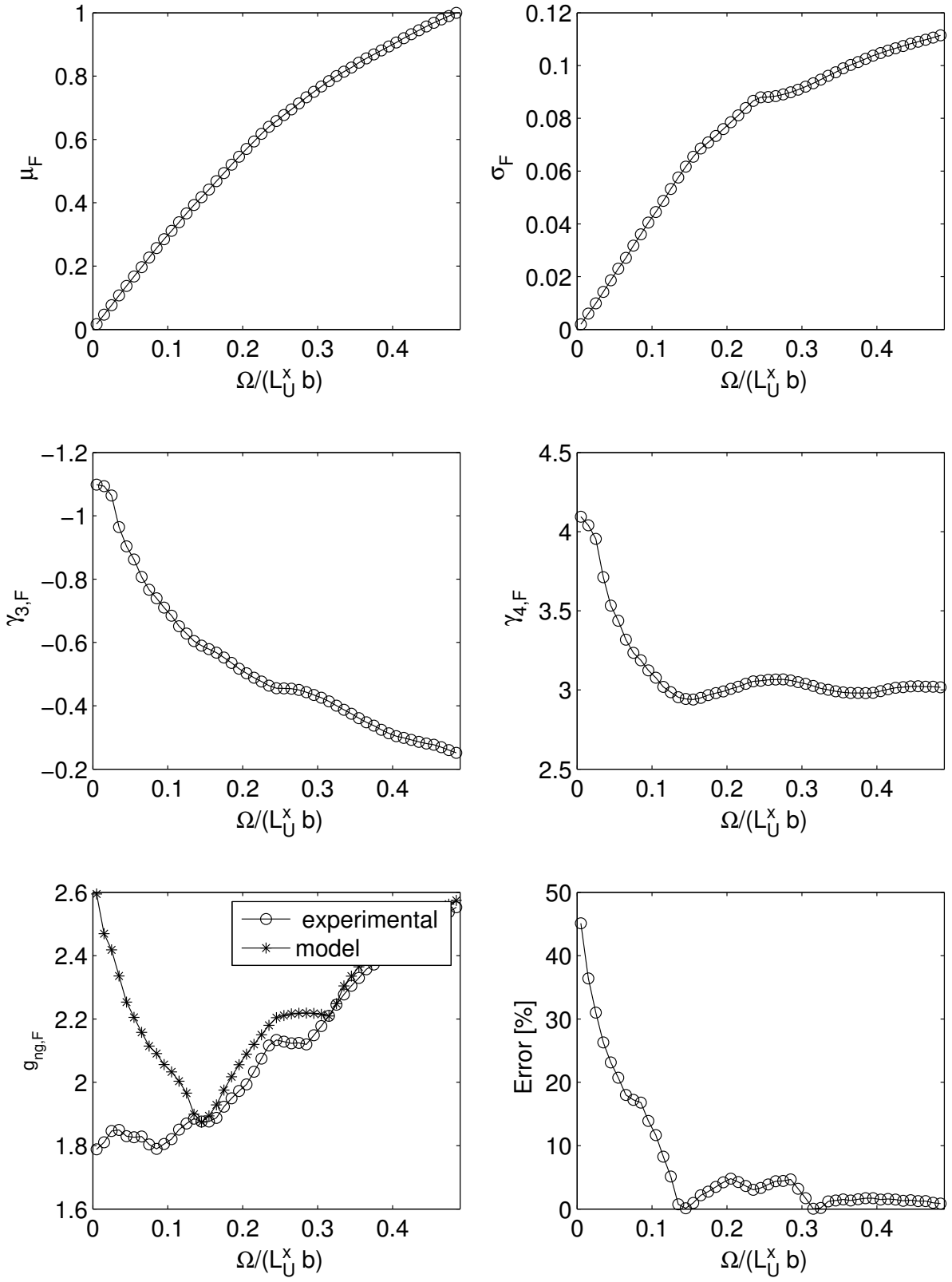

Figure 6.15 – Influence of the scale effect on the statistical moments and on the peak factor of the resultant force (Front facade)

6.4 Conclusion

This chapter answered the first question asked in the introduction of this thesis. We have seen that a non-Gaussian wind flow does influence the pressure field recorded on the windward facade of a building model. In the region where the wind flow is non-Gaussian, the pressure measurements are also non-Gaussian. On the other facades, the pressure field is generally non-Gaussian regardless of the statistical parameters of the incoming wind flow.

A section was dedicated to the analysis of the coherence between pressure signals and the different correlation lengths have been estimated. The longitudinal integral scale of turbulence was found to be a good estimation of the vertical correlation length on the front side of the building. I have also shown that the coherence decreased faster along the width of the model than along its height.

Finally, It was shown that the size effect influences the statistical distribution of the resultant wind force. I proposed to answer the second question of this thesis by giving some estimations of the minimal surface area that needs to be considered to characterize the resultant wind force as a Gaussian process. The conclusion is that if the interest of the experiment is focused on a surface of more than $80cm^2$ at model scale, on the front side, and $30cm^2$ on the other facade, the influence of the non-gaussianity in the wind flow can be neglected.

Chapter 7

Conclusions and perspectives

The first subject addressed in this thesis was the characterization of the atmospheric boundary layer that is created inside the wind tunnel of the university of Liège. We have seen that the mean velocity profile is similar to the fourth terrain category of the Eurocode 1-4 whereas the turbulence intensity diverts from the theoretical profiles. The longitudinal integral scale was found to be around 40 cm at model scale, which hardly represents the large scale turbulence with a length scale of 1/100. Then, the most interesting result of chapter 3 was the statistical characterization of the wind flow. I demonstrated that the wind flow can be considered Gaussian in the first 50 cm of the wind tunnel. Between 50 and 70 cm the transition to non-Gaussian flow occurs and above 70 cm the wind is clearly non-Gaussian. From these results, we could have concluded that the maximum model height that can be tested in the wind tunnel was 50 cm, to be consistent with the assumption of Gaussian wind flow realized in the design codes. However, before being hasty, it appeared interesting to study the influence of a non-Gaussian wind flow on the pressure measurements recorded on a high-rise building model in wind tunnel and the influence of the considered facade area on the stochastic nature of the resultant force on cladding.

In order to achieve these goals, I first proposed an exhaustive description of the pressure measurements recorded on each facades of the model and with different wind directions. It came out that along the height of the model, the pressure increases in absolute value with the altitude. I also found lower negative pressure on the lateral sides than on the back frontage. Positive pressure only acts upon the front side because the flow separation occurs at the edges of this facade. I noticed that interactions with the floor of the wind tunnel disturb the measurements in the first 8 m of the lateral facades. Then, pressure fluctuations appeared larger on the lateral faces than on the front and back sides. The skewness only happens to vary along the height of the front side whereas it stays constant on the three other faces. The kurtosis remains relatively constant and around the Gaussian value on the entire height of the building. Regarding the front and back sides, I noticed that changing the wind direction to 15 degrees does not affect the pressure measurements. At 45 degrees the only effect is to decrease the mean pressure on the front side while everything stay unaffected on the back one. Angles of incidence of 15 and 45° place the left side into the wake and the pressure recorded on this side becomes very similar

to those of the back face. The right side is highly affected by the wind direction and the profile of the statistical moments change considerably. Then, the frequency analysis revealed that the vortex shedding effect disappears on the right facade when the model is turned at 15 and 45 degrees whereas it remains visible on the left side. The results of the patches layout confirmed the comments made about the vertical measurements. It also showed that the variations along the width of the model are highly specific to the facade tested, the statistical moment chosen and to the wind direction. The most important conclusions about the front side are the "C shaped" mean and standard deviation profiles and the constant values along the width of the building for the skewness and kurtosis. The three other facades presented nearly constant mean values, flatter standard deviation profiles and generally higher skewness and kurtosis values at their windward edges. I also highlighted the fact that the four statistical moments change dimly along the height of each patch. Finally, the patches and the vertical layouts showed similar conclusions about the influence of the the wind direction. However it appeared difficult to fit specific trends to the skewness and kurtosis profiles along the width of the building model.

The pressure field being characterized, I was able to compare its statistical moments to those of coefficient of pressure computed with the velocity data and to analytic equations. It clearly appeared that a non-Gaussian wind flow does influence the pressure field recorded on the windward facade of a building model. In the region where the wind flow is non-Gaussian, the pressure measurements are also non-Gaussian. On the other facades, the pressure field is generally non-Gaussian regardless of the statistical parameters of the incoming wind flow. These results have been verified by comparison with others from the literature. Before tackling the second topic of this thesis, it was important to analyze the coherence between pressure signals. I gave some estimations of the different correlation lengths that characterize the pressure field. The longitudinal integral scale of turbulence was found to be a good estimation of the vertical correlation length on the front side of the building. It was also shown that the coherence decreases faster along the width of the model than along its height and was better modeled by a linear model. Finally, It was proven that the size effect influences the statistical distribution of the resultant wind force. I proposed estimations of the minimal surface area that need to be considered to characterize the resultant wind force as a Gaussian process. Finally, I concluded that if the interest of the experiment is focused on a surface of more than $80cm^2$ (at model scale), on the front side and $30cm^2$ on the other facades, the influence of the non-gaussianity in the wind flow can be neglected.

This thesis has reached its objectives and provides insights about the pressure field around a prismatic high rise building model. However, this work can be extended in different directions. For example, a deeper analysis of the coherence between pressure measurements can provide an alternative model to represent the coherence function better. Then, on the basis of this model, the influence of the size effect on the statistical moments of the resultant force could be verified with analytic developments. The patches layout gives a refined mesh of pressure measurements that limits the discretization of the continuous pressure field. Yet, it should also be extended to provide a broader view of the bidirectional pressure field.

Bibliography

[Andrianne and Denoël, 2014] Andrianne, T. and Denoël, V. (2014). *Statistical analysis of velocity measurements in an atmospheric boundary layer in wind tunnel*. Université de Liège.

[ASCE, 1999] ASCE (1999). *Wind Tunnel Studies of Buildings and Structures (ASCE Manuals and Reports on Engineering Practice No. 67*. American Society of Civil Engineers.

[Braun and Awruch, 2009] Braun, A. L. and Awruch, A. M. (2009). *Aerodynamic and aeroelastic analyses on the CAARC standard tall building model using numerical simulation*. Computers and Structures 87 (2009) 564–581.

[Carassale, 2012] Carassale, L. (2012). *Scale effect on the buffeting response of wind-excited structures*. Meccanica dei Materiali e delle Strutture, Vol. 3 (2012), no. 2, pp. 41-48.

[Denoël, 2005] Denoël, V. (2005). *Application des méthode d'analyse stochastique à l'étude des effets du vent sur les structures du génie civil*. Université de Liège.

[Denoël, 2013] Denoël, V. (2013). *Eléments de Processus Stochastiques*. Université de Liège.

[Dutta, 2006] Dutta, S. (2006). *sensitivity of a square cylinder wake to orientation and oscillation in the intermediate reynolds number regime*. Department of Mechanical Engineering Indian Institue of Technologu, Kanpur India.

[Dyrbye and Hansen, 1996] Dyrbye, C. and Hansen, S. O. (1996). *Wind Loads on Structures*. John Wiley and Sons.

[EN1991-1-4, 2005] EN1991-1-4 (2005). *EN 1991-1-4 - Eurocode 1: Actions on structures - Part 1-4: General actions - Wind actions*.

[Gioffrè et al., 2001] Gioffrè, M., Gusella, V., and Grigoriu, M. (2001). *Non-Gaussian wind pressure on prismatic buildings, I: Stochastic field*. Journal of Structural Engineering 2001.127:981-989.

[Gurley et al., 1997] Gurley, K. R., Tognarelli, M. A., and Kareem, A. (1997). *Analysis and Simulation Tools for Wind Engineering*. Prob. Eng. Mech., 12(1), 9-31.

[Hilhorst, 2009] Hilhorst, H. J. (2009). *Central limit theorems for correlated variables: some critical remarks.* Brazilian Journal of Physics, vol. 39, no. 2A, August, 2009.

[Huanga et al., 2007] Huanga, S., Li, Q., and Xua, S. (2007). *Numerical evaluation of wind effects on a tall steel building by CFD.* Journal of Constructional Steel Research 63 (2007) 612–627.

[Kumar and Stathopoulos, 1998] Kumar, K. S. and Stathopoulos, T. (1998). *Synthesis of non-Gaussian wind pressure time series on low building roofs.* Engineering Structures 21 (1999) 1086–1100.

[Larose, 2002] Larose, G. L. (2002). *The dynamic action of gusty winds on long-span bridges.* Danmarks Tekniske Universitet, Rapport BYG DTU R-029 2002 ISSN 1601-2917 ISBN 87-7877-088-2.

[N. Blaise and Denoël, 2014] N. Blaise, T. C. and Denoël, V. (2014). *Calculation of third order joint acceptance function for line-like structures.* IN-VENTO 2014 XIII Conference of the Italian Association for Wind Engineering 22-25 June 2014, Genova, Italy.

[O'Neill et al., 2004] O'Neill, P. L., Nicolaides, D., Honnery, D., and Soria, J. (2004). *Autocorrelation Functions and the Determination of Integral Length with Reference to Experimental and Numerical Data.* University of Sydney.

[Panigrahi et al., 2008] Panigrahi, P. K., Dutta, S., and Muralidhar, K. (2008). *Experimental Investigation of Flow Past a Square Cylinder at an Angle of Incidence.* Journal of Engeneering Mechanics, ASCE, September 2008.

[Simiu and Scanlan, 1977] Simiu, E. and Scanlan, R. H. (1977). *Wind effects on structures : An introduction to wind engineering.* Wiley-Interscience Publication.

[Wang et al., 2013] Wang, F., Dutta, R., Bohlmann, B. F., and Stelson, K. A. (2013). *Analysis of Short-Term Energy Storage for Midsize Hydrostatic Wind Turbine.* Journal of Dynamic Systems, Measurement, and Control, Volume 136.

Appendix A

Peak velocity factor

This section gives some insights about the peak velocity factor that can be found in the Eurocode 1-4.

We first make the assumption that it exists a perfect correlation between the pressure peaks on the structure. This hypothesis is admissible when the characteristic length of the structure is far smaller than the turbulence integral length of the wind flow. Then, if the structure is considered stiff and by neglecting the quadratic turbulence term, the force applied on the surface Ω can be computed by :

$$F(t) = \frac{1}{2}\rho C_d \Omega (U + u(t))^2 \tag{A.1}$$

$$F(t) \simeq \frac{1}{2}\rho C_d \Omega (U^2 + 2Uu(t)) \tag{A.2}$$

$$F(t) \simeq \frac{1}{2}\rho C_d \Omega U^2 + 2\frac{1}{2}\rho C_d \Omega U u(t) \tag{A.3}$$

From equation A.3 we can see two effects of the wind. The first term of the right member is the mean wind effect and the second term is the fluctuating wind effect. We can therefore decompose the force into two similar components:

$$F_{mean} = \frac{1}{2}\rho C_d \Omega U^2 \tag{A.4}$$

$$\Delta F(t) = 2\frac{1}{2}\rho C_d \Omega U u(t) \tag{A.5}$$

From equation A.4 we can compute the mean displacement of the structure:

$$\bar{x} = \frac{F_{mean}}{K} \tag{A.6}$$

With K the stiffness matrix of the considered structure.

From equation A.5 we can compute the standard deviation of the displacement:

$$\sigma_x = \frac{\sigma_{\Delta F}}{K} = \frac{2\frac{1}{2}\rho C_d \Omega U}{K}\sigma_{u(t)} = \frac{2F_{mean}}{KU}\sigma_u(t) \tag{A.7}$$

Then from the definition of the turbulence intensity $I_v = \frac{\sigma_u(t)}{U}$ it follows that :

$$\sigma_x = \frac{2F_{mean}}{K} I_v \tag{A.8}$$

The extreme value of each stochastic process can be computed with:

$$x_{max} = \bar{x} + g.\sigma_x \tag{A.9}$$

With g the peak factor of the stochastic process x (typically taken equal to 3.5 in the Eurocode 1-4).

By inserting equation A.8 into equation A.9 we have:

$$x_{max} = \frac{F_{mean}}{K}(1 + 2gI_v) = \frac{F_{mean}}{K}(1 + 7I_v) \tag{A.10}$$

This development explains the origin of the peak velocity pressure of the Eurocode 1-4.

$$q_p(z) = (1 + 7I_v(z))\frac{1}{2}\rho U^2(z) \tag{A.11}$$

Appendix B

Size factor

For structures having a windward surface larger than the order of magnitude of the integral scale of turbulence L_u^x of the wind flow, the pressure cannot be considered as perfectly correlated any more. The pressure peaks do not occur at the same moment on the entire surface of the building. Consider a perfectly correlated pressure field would lead to overestimate the resultant forces. The concept of coherence is introduced in the Eurocode by the size factor c_s that takes into account the reduction effect on the wind action due to the non-simultaneity of occurrence of the peak wind pressures on the surface. This factor depends on the background factor B^2 allowing for the lack of full correlation of the pressure on the structure surface.

The size factor c_s is defined as:

$$c_s = \frac{1 + 7I_v(z)\sqrt{B^2}}{1 + 7I_v(z)} \tag{B.1}$$

Recalling the development of the previous section, I showed that the force applied by the wind on a structure can be split into a mean part and a fluctuating part. For a structure of area Ω greater than L_u^x the pressure field is not prefectly correlated and the equation A.4 and A.5 become:

$$F_{mean} = \iint_{\Omega} \frac{1}{2}\rho C_d \Omega U^2 d\omega = \frac{1}{2}\rho C_d \Omega U^2 \tag{B.2}$$

$$\Delta F(t) = \iint_{\Omega} 2\frac{1}{2}\rho C_d \Omega U u(t,x,y)\, d\omega \tag{B.3}$$

We can introduce the background factor B^2 by:

$$\Delta F(t) = 2\frac{1}{2}\rho C_d \Omega U \iint_{\Omega} u(t,x,y)\, d\omega = 2\frac{1}{2}\rho C_d \Omega U\sqrt{B^2} \tag{B.4}$$

We can now use equation A.9 to write:

$$x_{max} = \bar{x} + g.\sigma_x = \frac{F_{mean}}{K}(1 + 2g\sqrt{B^2}I_v) \tag{B.5}$$

Finally, by dividing equation A.10 by B.5 we end up with:

$$\frac{1 + 7\sqrt{B^2} I_v}{1 + 7 I_v} = c_s \tag{B.6}$$

This equation constitutes the definition of the the size factor c_s of the Eurocode 1-4. It represents the ratio between the response of a structure and the response of the same structure considering perfectly correlated response. The response of the structure can therefore be computed by multiplying the perfectly correlated response (using the peak velocity pressure) by the factor c_s.

The Eurocode also consider a dynamic factor c_d, that takes into account the resonance effect of the structure introduced by the vibrations due to the turbulence.

Appendix C

Influence of the integration domain on the integral scale of turbulence

Recalling section 2.2, the longitudinal integral scale of turbulence L_u^x is often computed using Taylor's hypothesis of "frozen turbulence".

$$L_u^x(z) = U(z)T(z) \tag{C.1}$$

With $U(z)$ the longitudinal mean wind speed and $T(z)$ is the time scale defined as :

$$T(z) = \int_0^\infty \rho_u^T(z,\tau)d\tau \tag{C.2}$$

The autocorrelation function $\rho_u^T(z,\tau)$ of the turbulence is defined as:

$$\rho_u^T(z,\tau) = \frac{E[u(z,t).u(z,t+d\tau)]}{\sigma_u^2(z)} \tag{C.3}$$

By definition, equation C.2 has to be realized over the entire range of $d\tau$. However, I noticed that the time and integral scales of turbulence strongly depend on the integration domain in equation C.2. The lower bound is fixed to zero but, the higher bound plays a significant role. The article [O'Neill et al., 2004] proposes different methods to determine the integration domain:

1. Integrate only up to the value where the autocorrelation function falls to $1/e$.
2. Integrate over the entire available domain.
3. Integrate only up to the first zero-crossing.
4. If the autocorrelation function has a negative region, integrate only up to the value where the autocorrelation function is a minimum.

Figure C.1 and C.2 represent time and integral scales computed with the four methods.

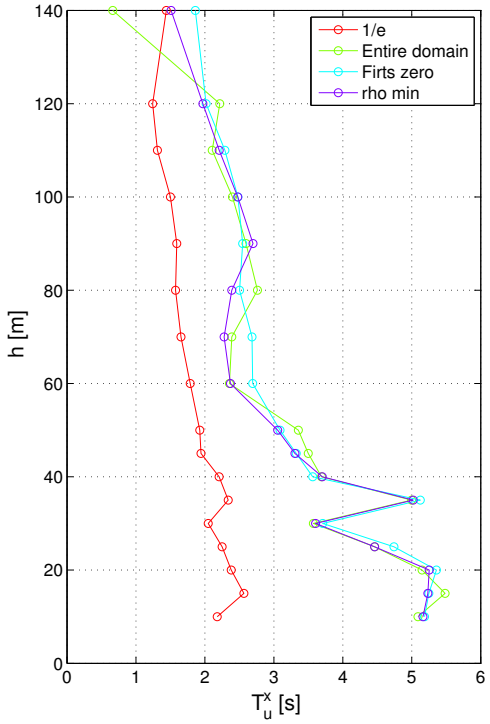

Figure C.1 – Influence of four types of integration domain on time scales

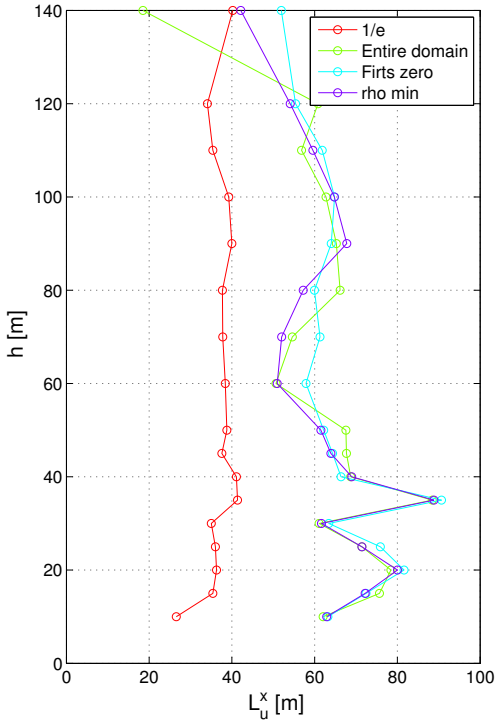

Figure C.2 – Influence of four types of integration domain on longitudinal integral scales of turbulence

By seeing the results on figures C.1 and C.2, we can conclude that only the first method gives results in line with the logic. Indeed the longitudinal integral scale of turbulence is supposed to increase with the altitude as the nominal size of vortices increase with the altitude. This conclusion is also supported in the article [O'Neill et al., 2004].

I also computed the time and integral scales by fixing different values of integration domain upper bounds. Results are shown on Figure C.3 and C.4.

We can see on these figures that the upper bound limit of the integration domain seems to be around 0.1 second in order to have results consistent with the logic.

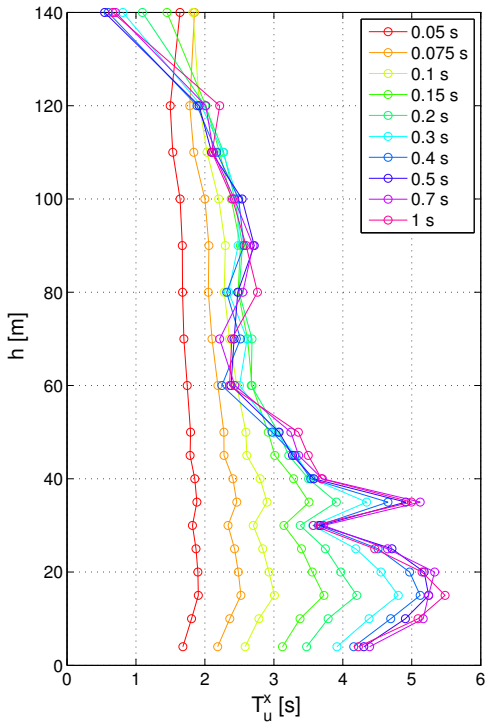

Figure C.3 – Influence of different upper bounds of integration domain on time scales

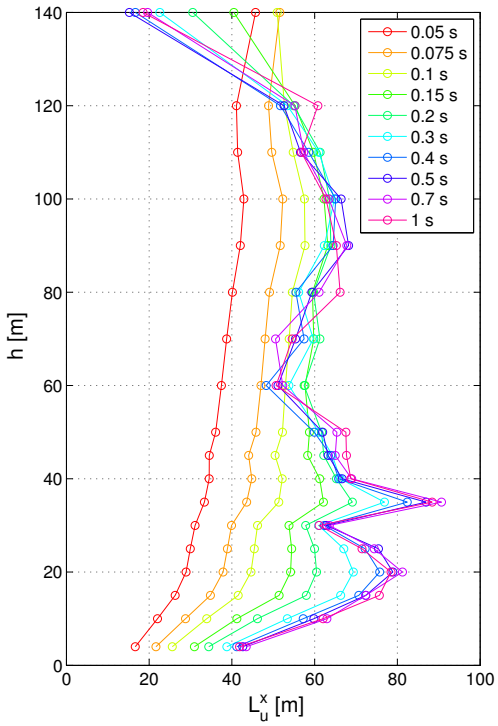

Figure C.4 – Influence of different upper bounds of integration domain on longitudinal integral scales of turbulence

Finally, the method that consists in integrating only up to the value where the auto-correlation function falls to $1/e$ have been chosen. This method is equivalent to fix the integration domain upper bound to a value ranging from 0.035 s to 0.076 second, depending on the height where the measurements are taken. The mean value of the upper bounds is 0.054 second with this method. Values of T_u^x and L_u^x depicted by the red lines on figure C.3 and C.4 are consistent with those on figure C.1 and C.2.